UNIVERSITY OF CALIFORNIA,
IRVINE

Network Biomarkers of Neurological Disease

DISSERTATION

submitted in partial satisfaction of the requirements
for the degree of

DOCTOR OF PHILOSOPHY

in Biomedical Sciences

by

Maria Inez Falcon

Dissertation Committee:
Professor Ana Solodkin, PhD Chair
Professor Steven L. Small, MD, PhD
Professor David J. Reinkensmeyer, PhD

2016

DEDICATION

For Elmo T. Falcon, PhD

TABLE OF CONTENTS

LIST OF FIGURES

LIST OF TABLES

ACKNOWLEDGMENTS

Innumberable thanks to Dr. Ana Solodkin, my PI and committee chair, for choosing me as her first graduate student to mentor towards a PhD. Her passion, guidance and encouragement has been crucial to my graduate training, my successful completion of my degree, and my development as a scientist. I am forever grateful for her mentorship during these years. Many thanks are owed to my wonderful thesis committee, Dr. Steven L. Small and Dr. David Reinkensmeyer. Their support and feedback over the years has contributed immensely to the success of the work described in this dissertation. I would also like to express sincere thanks to members of my advancement committee, Dr. Jeffrey Krichmar, Dr. Ron Frostig, and Dr. David Lyon, for their comments and insight.

I owe a great many thanks to my collaborators, Drs. Anthrony R. McIntosh, Viktor Jirsa, Paula Sanz Leon, Joaquin Goni, Petra Ritter, and Lia Domide for sharing their time and expertise. Many of these collaborators were co-authors on the publications resulting from my graduate work, and significantly enhanced my training these past five years.

My graduate experience would not have been nearly as enjoyable without the companionship of my fellow lab mates in the Solodkin/Small Brain Circuits Lab, and my peers in the Interdepartmental Neuroscience Program (Class of 2016) and in the Department of Anatomy and Neurobiology. It has been a true pleasure experiencing the trials and tribulations of graduate school with such intelligent, supportive and fun people, and I am forever grateful for all the times we have shared.

Financial support for this work was provided by NIH (RO1-NS-54942) and the James McDonnell Foundation: Brain Network Recovery Group. I would also like to express my sincere gratitude to the Orange County Chapter of ARCS for providing me with a 2-year fellowship. Both their financial and emotional support throughout my graduate work was intangible.

Finally, I would like to thank my family for their never-ending support as I moved across the country for graduate school. I am so thankful for the many visits and trips we have shared these past few years, and for having a family that has pushed me to strive for success, and has celebrated and shared in my excitement over my accomplishments. This dissertation is dedicated to my late dad, Dr. Elmo T. Falcon, who always emphasized the value of a good education, and who always motivated me to work at the “cutting edge of science.”

CURRICULUM VITAE

Maria Inez Falcon

Education

2016 Ph.D., Biomedical Sciences, University of California, Irvine; Irvine, CA

2010 B.S., Biomedical Engineering, Georgia Institute of Technology; Atlanta, GA

Research Experience

2011- Graduate Student, Department of Anatomy & Neurobiology
University of California, Irvine; Irvine, CA
Research advisor: Ana Solodkin, PhD

2010-2011 Research Technician, Department of Cell Biology
Emory University; Atlanta, GA
Research advisor: Arthur English, PhD

2009-2011 Research Technician, Department of Applied Physiology
Georgia Institute of Technology; Atlanta, GA
Research advisor: T. Richard Nichols, PhD

Teaching Experience

2015 Cellular Biology (D103), Professors: Sarah Lutz, PhD, Adeela Syed, PhD
2014 General Biology (Bio 93), Professor: Andrea Nicholas, PhD
2013 General Biology (Bio 93), Professors: Andrea Nicholas, PhD, Diane O'Dowd, PhD, Amie Edinger, PhD
Media and the Mind, Professor: Andrea Nicholas, PhD
Stress, Professor: Andrea Nicholas, PhD
2012 General Biology (Bio 93), Professors: Diane O'Dowd, PhD

Publications

Falcon, M.I., Stahl, V.A., Nichols, T.R. (2011). Evidence that Popliteal Fat Provides Damping during Locomotion in the Cat. Cells Tissues Organs. 193(5):336-341

Falcon, M.I., Gomez, C.M., Chen, E.E., Solodkin,A. (2015). Early Cerebellar Network Shifting in Spinocerebellar Ataxia Type 6. Cerebral Cortex.

Falcon, M.I., Riley, J., Shereen, A.D., Chen, E.E., Solodkin, A. (2015). The Virtual Brain: Modeling Biological Correlates of Recovery after Chronic Stroke. Frontiers in Neurology.

Falcon, M.I., Riley, J., Jirsa, V., Chen, E.E., McIntosh, A.R., Solodkin, A. (2016). Functional Mechanisms of Recovery after Chronic Stroke: Modeling with The Virtual Brain. *Submitted.*

Publications In Preparation

Falcon, M.I., Jirsa, V., Riley, J., Chen, E.E., McIntosh, A.R., Solodkin, A. (2016). A New Neuroinformatics Approach to Precision Medicine in Neurology: The Virtual Brain.

Falcon, M.I., Rowe, J.B., Wolbrecht, E., Solodkin, A., Reinkensmeyer, D.J.(2016). Lack of finger individuation during motor adaptation.

Conference Abstracts

Falcon, M.I., Stahl, V.A., Nichols, T.R. (2010). The influence of muscles, fascia and adipose tissue on limb and joint variables during locomotion. Abstract for poster presentation, Society for Neuroscience Annual Meeting, San Diego, CA.

Falcon, M.I., English, A.W. (2011). Continuous Treadmill Training Increases trkB Expression in the DRG of Male But Not Female Mice. Abstract for poster presentation, Society for Neuroscience Annual Meeting, Washington D.C.

Falcon, M.I., Gomez, C.M., Solodkin, A. (2012). Functional intra-cerebellar shifts concur with disease progression of Spinocerebellar Ataxia 6**.** Abstract for poster presentation, Society for Neuroscience Annual Meeting, New Orleans, LA.

Falcon, M.I., Shereen A.D., Gomez, C.M., Solodkin, A. (2013). Elucidating plasticity of white matter cerebellar pathways in Spinocerebellar Ataxia Type 6. Abstract for poster presentation, Organization for Human Brain Mapping 19th Annual Meeting, Seattle, WA.

Falcon, M.I., Riley, J., Chen, E. E., Solodkin, A. (2013). Action Observation Stroke Therapy and long-term maintenance of motor gains. Abstract for poster presentation, Society for Neuroscience Annual Meeting, San Diego, CA.

Falcon, M.I., Riley, J., Chen, E. E., Solodkin, A. (2013). Increased maintenance of motor gains following a novel stroke therapy. Abstract for poster presentation, International Stroke Conference, San Diego, CA.

Falcon, M.I, Riley, J., Jirsa, V., Chen, E.E., Shereen, A.D., Solodkin, A (2014). Initial observations into functional mechanisms of chronic stroke: modeling with The Virtual Brain. Abstract for poster presentation, Organization for Human Brain Mapping 20th Annual Meeting, Hamburg, Germany.

Falcon, M. I., Rowe, J.B., Wolbrecht, E., Solodkin, A., Reinkensmeyer, D. J (2014). Finger Individuation at the motor learning level. Abstract for poster presentation, Society for Neuroscience Annual Meeting, Washington, D.C.

Falcon, M.I., Riley, J., Shereen, A.D., Chen, E.E., Solodkin, A. (2015). The Virtual Brain: New Modeling of Stroke Recovery and its Relationship with Global Efficiency. Abstract for poster presentation, Organization for Human Brain Mapping 21st Annual Meeting, Honolulu, HI.

Academic And Professional Honors

2013 Achievement Rewards For College Scientists (ARCS) Foundation Fellowship

Professional Memberships
2013- American Heart Association
2013- Organization of Human Brain Mapping
2010- Society for Neuroscience

ABSTRACT OF THE DISSERTATION

Network Biomarkers of Neurological Disease

By

Maria Inez Falcon

Doctor of Philosophy in Biomedical Science

University of California, Irvine, 2016

Professor Ana Solodkin, Chair

Identifying biomarkers of brain disease is a crucial goal of neurological care as it could translate into improved diagnoses and targeting of individualized treatments. Such biomarkers at the cellular and molecular level are difficult to detect directly in humans with current imaging methods, precluding the identification of true biomarkers of disease. Recent advancements in network analyses and computational modeling have enabled novel ways to identify biophysical parameters in imaging data. The studies in this dissertation explored these methods using two models of neurological disease: Spinocerebellar Ataxia Type 6 (SCA6), a neurodegenerative disease, in which biomarkers can help determine pre-symptomatic changes, and stroke, in which biomarkers can be used to predict long-term recovery. The general objective was to examine physiological mechanisms subjacent to individualized clinical phenotype in SCA6 and stroke, to get closer to developing concrete cures. In Chapter 1, a combination of structural equation modeling, DTI, and functional activation maps were used to detect functional and structural brain changes at different stages of severity of SCA6. An increase in cerebellar activation as well as increased connectivity between cerebellum and cerebral cortex in pre-symptomatic patients was found. A concomitant structural change was seen in the

cerebral and cerebellar peduncles. These results showed the sensitivity of using network analysis in detecting brain alterations prior to symptom onset in a degenerative disease. However, these changes seen were at a network level with no ties to the underlying physiology, limiting them from being true biomarkers of SCA6. Therefore, Chapters 4-7 used a novel modeling application, The Virtual Brain, to model brain dynamics associated with stroke using models dependent on the structural brain connectivity of individuals, plus local physiological parameters. Results showed that compared to controls, individuals with stroke showed differences in several physiological parameters indicating a hyper-excitable brain state. This hyper-excitable state was associated with poor motor recovery. Manually normalizing the identified parameters in stroke cases led to a normalization of brain activity, indicating the promise of these parameters in acting as biomarkers for stroke recovery, and the utility of The Virtual Brain in furthering the goal of individualized medicine. These studies in stroke comprise some of the first forays into a new type of brain analysis, in which multiple scales are explored to bridge the brain dynamics and global level connectivity changes associated with neurologic disease with their underlying mechanistic underpinnings in individuals. In summary, the results from the studies comprising this dissertation hopefully provide evidence that novel network analyses and advances in computational modeling can herald a new era of biomarker exploration to pave the way for individualized medicine.

INTRODUCTION

Neurological care strives for cures. Yet one of the most salient challenges in neurological care is the high variability in presentation, progression, and response to treatment among brain diseases across patients. For example, in stroke, patients with similar size and location of lesions might display differences in deficits and recovery at the same time that different lesions can produce similar symptomatology (Fridriksson et al., 2002; Irle, 1987; Page et al., 2013). While some of this variability is due to the nature of the disease (Jirsa et al., 2010; Nelson et al., 2012), much of the variability stems from the great diversity of both brain anatomy and function at the individual level. This diversity is evident at a gross level through anatomical primate studies and human autopsy studies (Adler and Milhorat, 2002; LeMay, 1976), as well as through structural human imaging (Allen et al., 2002; Bartley, 1997; Catani and Thiebaut de Schotten, 2008). Variability in brain function has also been observed, specifically through studies using functional MRI and electroencephalography (EEG) which show different amounts and patterns of brain activity within populations (Mueller et al., 2013a) and between various populations (including different age groups (Di et al., 2014), healthy and disease populations (Grefkes et al., 2008), and gender related differences(Scheinost et al., 2015)). However, even accounting for differences between such groups does not remove all variability in brain function. Some behavioral and gross functional measures of variability can be traced to variations at the genetic level (McHughen et al., 2010; Pearson-Fuhrhop et al., 2012) and to some degree, variations at the neuronal level such as neurotransmitter levels via PET imaging (Frick et al., 2015). However, we have thus far been limited in assessing variations in brain mechanisms at the cellular and molecular levels in humans due to the lack of tools to more

directly measure them. Consequently, translational studies in neurologic disease involving such mechanisms on a finer scale are rare.

A. A Connectivity Approach to Brain Disease

A critical approach to studying brain function is to understand the link between brain anatomy and physiology on one hand and ultimate behavior on the other. The first link (anatomy to function) was first described in the seminal studies by the anatomist, Santiago Ramon y Cajal, in which he first applied a then novel method, based on the silver staining technique developed by Camilo Golgi, to the cerebellar cortex that allowed him to visualize neuronal morphology. Based on visual inspection under the microscope, Cajal concluded that, rather than being contiguous with one another, neurons were anatomically discontinuous from each other via free endings (Sotelo, 2011; Zamora-Berridi et al., 2011), yet, inferred the existence not only of information flow between neurons but also suggested that this flow had directionality, or polarization ((Sotelo, 2011); **Figure i**). These studies formed the critical basis of understanding the inner workings of the brain, and ultimately led to the development of the revolutionary Neuron Doctrine, which established the neuron as *the anatomical, physiological, genetic, and metabolic unit of the nervous system* (DeFelipe, 2013; Shepherd, 1972; Zamora-Berridi et al., 2011). Later electrophysiological studies confirmed Cajal's theories by proving the existence of synapses by Sir Charles Scott Sherrington in 1897 (Bennett,

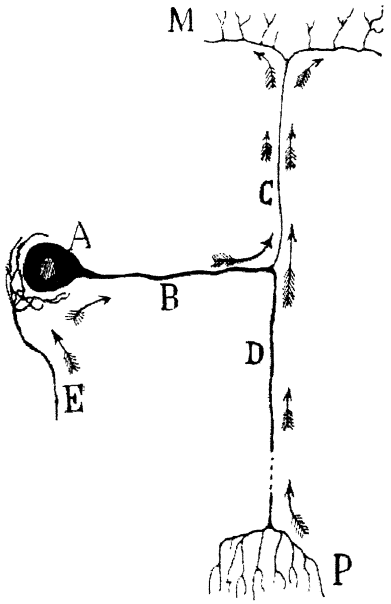

Figure i. Polarization in a neuron. Figure 32 in Volume I of Cajal's Histologie du Système Nerveux de l'Homme et des Vertébrés. Adapted from (Berlucchi, 2010).

1999), thus demonstrating the transmission of information between neurons.

In the field of neurology, behavior, specifically as a result of disease, can be inferred from the integration of anatomy and physiology. Historically and in part even currently, this manifests in the belief that different symptoms are associated with lesions to specific regions, as exemplified by the seminal studies by Paul Broca (Broca; Dronkers et al., 2007). In his most remarkable work, Broca noted that two individuals (Leborgne and Lelong) with damage to the left frontal lobe both still appeared to understand language, however had difficulty speaking, wherein each could only repeat a single word (Dronkers et al., 2007). Based on the anatomical location of the pathology of these patients, Broca attributed a specific form of aphasia (Broca's Aphasia) to a specific portion of the left inferior frontal lobe (Broca's Area). Notably, while he suggested that these lesions extended into the white matter, Broca focused solely on damage to the grey matter (Dronkers et al., 2007). Years later, with the development of magnetic resonance imaging, further analysis of these cases revealed that the lesions were actually much more widely distributed (Dronkers et al., 2007). Additionally, since that time, lesion overlap studies have shown that the correlation between patients with Broca's Aphasia and lesions to Broca's Area is inconsistent (Catani and Mesulam, 2008; Dronkers et al., 2007), and hence, many investigators have raised criticism on the limitations associated with this method of assigning behaviors based off of lesion location (Catani and Mesulam, 2008; Finger et al., 2004).

Subsequent studies followed different approaches by expanding the analysis to exploring pathways connecting brain regions. Norman Geschwind's pivotal studies in disconnection syndromes (Catani and ffytche, 2005; Fornito et al., 2015; Geschwind, 1970) are a remarkable example as they provided a new perspective on lesion analysis. Prior to

Geschwind's studies, based on Wernicke's associationist theory (1874), disconnection syndromes were considered to be the result of lesions to white matter connections leading to cognitive dysfunction. Geschwind's work used brain anatomy to expand this definition, arguing that a lesion to an association cortex, if large and widespread enough, or a lesion to a white matter pathway stemming from an association cortex, could produce dysfunction, based on the complex arrangement of fibers within association cortices and their connecting pathways. These studies even when they mapped symptoms to specific lesion locations, are important as they assigned symptoms to specific lesions including both grey matter and white matter (GESCHWIND, 1965). Therefore, while this work was a critical step in drawing correlations between pathology and behavior that highlighted the importance of the pathways connecting brain regions, this perspective was later proven to be overly simplistic, as it still only considered only a one-to-one correspondence between lesion location and behavioral deficit (Catani and ffytche, 2005; Fornito et al., 2015). More recent studies have further demonstrated the limitations of one-to-one lesion mapping, by showing that while some lesion properties, such as size and location, may be responsible for specific deficiencies, clinical observations reveal an inconsistent relationship between the nature of a brain lesion and the resulting functional deficit. Although some classic 'deficit syndromes' do exist, there is significant variation among individuals. The functional basis for such variation is poorly understood, and there is no consensus on a theoretical or empirical framework for linking brain injury to functional deficits (Jirsa et al., 2010).

With advancing knowledge on the anatomy of the human brain, contemporary distributed network and connectionist theories of brain function based off of Geschwind's early

work have been developed (Catani and ffytche, 2005; Deco and Kringelbach, 2014; Hartman et al., 2011; McIntosh, 2000). These theories posit that a greater understanding of individual variability in brain disease is facilitated by viewing brain anatomy and function from a distributed network perspective, where the brain can be thought of as a complex network composed of different nodes linked by connections (Bullmore and Sporns, 2009; Hartman et al., 2011; Sporns et al., 2004). In current theories, these connections may refer to the anatomical links between individual neurons (synapses), or between neuronal populations or anatomically segregated brain regions (fiber pathways) (Cabral et al., 2014). Through such connections, information is shared between neurons and between brain regions (McIntosh, 2000). Therefore, a perturbation to the system in a specific brain region will have a distributed network effect by conveying changes to remote parts of the brain. For example, John Hughlings Jackson argued that some observable symptoms may be due not to damage from the primary lesion, but secondary effects to other brain regions, as did Von Monakov in 1914, naming this long-term phenomenon “Diaschisis” (Finger et al., 2004). Thus, the basis for using brain network analysis to understand neurologic disease stems from the notion that a primary lesion, present in a specific area of the brain, may affect that area directly (necrosis), as well as remote regions, through changes in an array of connections. Such effects may be functional (diaschisis) or structural (transneuronal degeneration) (Fornito et al., 2015). Therefore, behavioral deficits following damage or disease can reflect either the abnormal operation of a damaged network, or the formation of a completely different network with entirely new behavioral repertoires (Breakspear and Jirsa, 2006; Jirsa et al., 2010).

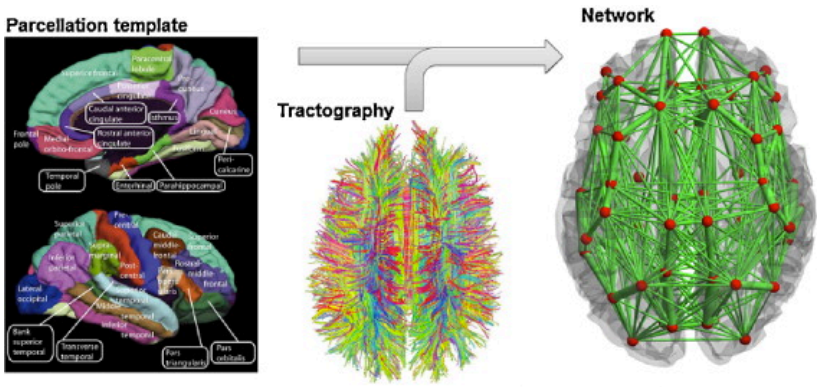

Figure ii. Brain network generated from anatomical brain parcellations and DTI tractography. Modified from (Cabral et al., 2014).

The introduction of human imaging has provided the opportunity to study both structural and functional connectivity in humans in vivo: the structural pathways connecting brain regions can be inferred by detecting white matter tracts using diffusion weighted imaging (**Figure ii)**, and the functional connections between brain regions can be inferred by calculating temporal correlations between neural activity measures (functional MRI, EEG, PET) (Betzel et al., 2014; Cabral et al., 2013, 2014). Some recent imaging studies have provided evidence that damage to specific brain regions results in disturbance of a network via changes to regions and the connections among them, suggesting that some of the observed variability in symptoms and deficits may be a result of brain network disruption (Breakspear and Jirsa, 2006; Ward, 2003; Ward and Cohen, 2004). Ultimately, applying these imaging methods to neurologic disease allows for investigation into the "potential spread of disease along connections in brain networks" (Verstraete and Foerster, 2015), and importantly, may allow for the identification of brain measures that correlate with disease.

B. Biomarkers of Neurologic Disease

A biomarker is a surrogate clinical measure that ideally reflects underlying biological processes on the cellular/molecular level that can be used as an indicator of disease state

(Burke and Cramer, 2013). The crucial feature of a biomarker is that it is consistently reliable for each individual, allowing it to be used to diagnose disease, monitor disease progression, and predict patient response to treatment (Agrawal and Biswas, 2015; Berger and Reindl, 2015). A widely used example in Medicine is the diagnosis and treatment of diabetes based on the concentration of hemoglobin A1c, which reflects degree of glucose metabolism and is consistently increased in diabetes (Caveney and Cohen, 2011; Larsen et al., 1990).

Because of their utility in medical practice, researchers are actively seeking biomarkers of brain injury as a means to personalize treatment and track individual recovery. Currently, biomarkers of neurological disease reflect brain activity related to progressive damage or recovery, correlate with behavioral state (Burke and Cramer, 2013) and can be sensitive, specific, minimally invasive, and relatively easy and inexpensive to measure (Agrawal and Biswas, 2015; Harris and Sadiq, 2014). Yet these neurological biomarkers typically fall into one of three categories: a) indirectly correlated with disease; b) directly correlated with disease; c) directly related to molecular and cellular disease processes. Multiple diverse methods have been explored for viable biomarkers of neurological diseases, including genetics (Agrawal and Biswas, 2015), immunological factors (Karim and Jacob, 2012), molecular imaging (Agrawal and Biswas, 2015), and protein, antibodies (Berger and Reindl, 2015), RNA or metabolite levels detected in blood or CSF samples.

More recently, several clinical imaging techniques, such as computed tomography (CT), magnetic resonance spectroscropy (MRS), magnetic resonance imaging (MRI), ultrasonography, gamma scintigraphy, and positron emission tomography (PET), have been investigated for measures that can serve as biomarkers of neurological diseases. The data collected from these

methods are increasingly supported indirectly by studies at the cellular and molecular level (Verstraete and Foerster, 2015), and thus have the benefit of using longitudinal, non-invasive approaches to characterize disease and assess treatment efficacy (Jung and Lee, 2015). Various neuroimaging measures have been identified that correlate with disease for several neurological disorders, including Alzheimer's disease (Mintun, 2005), epilepsy (Walker et al., 2015), Parkinson's Disease (Miller and O'Callaghan, 2014), and ALS (Verstraete and Foerster, 2015), with varying degrees of success thus far. However, none of these candidate biomarkers can be used clinically yet. The greatest limitation of these potential biomarkers is the high presence of type 1 (false positive) and type 2 (false negative) diagnostic errors; that is, although many identified measures may show correlations with disease within a large population, they lack the precision, specificity, and reliability necessary to implement them in treatment protocols for individuals (**Figure iii**). For example, hippocampal atrophy is a prominent candidate for a surrogate measure of neurodegeneration in Alzheimer's disease. Yet, the prediction rate is as low as 65%, greatly limiting its feasibility as a biomarker (Coupé et al., 2015; Frisoni and Weiner, 2010; Wolz et al., 2011).

More importantly, most of the biomarkers listed above fall into the second neurological biomarkers category. That is, they are correlated with disease, but lack a direct relation to underlying processes. Therefore, the degree to which they can assist with prognosis and

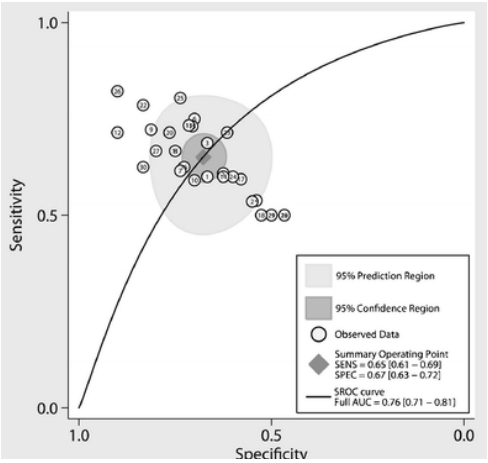

Figure iii. Meta-analysis of DTI studies showing that a single imaging metric results in marginal diagnostic accuracy of ALS. AUC= area under curve; SROC= summary receiver operator curve. Adapted from (Verstraete and Foerster, 2015)

treatment is limited. Moving forward, in order to better identify candidate biomarkers by using gross human imaging measures, it is helpful to have a deeper understanding of the basic biological processes that such measures represent. Specifically, biomarkers falling into the third category can provide direct targets for treatment. Identifying such biomarkers is an ongoing endeavor that the experiments comprising this dissertation attempt to address, where we aim to test the potential value of different MRI-derived metrics as biomarkers for Spinocerebellar Ataxia Type 6 and Ischemic Stroke using novel tools for assessing brain structure and function.

C. Objective and Specific Aims

Understanding basic mechanisms of brain disease is a crucial goal of the bridge between neuroscience and neurology, as this could translate into improved diagnoses and targeting of individualized treatments. In humans, brain mechanisms at the cellular and molecular level are difficult to detect directly with current imaging methods, precluding the identification of true biomarkers of disease state. Recently, advancements in network analyses and computation modeling have enabled novel ways to identify biophysical parameters in imaging data. In order to test the robustness of these methods, we explored two key models of neurological disease with different needs and applications for biomarkers. The first, a neurodegenerative disease, Spinocerebellar Ataxia Type 6 (SCA6), in which biomarkers can help determine pre-symptomatic changes, and the second, stroke, in which biomarkers can predict long-term recovery and hence, in both cases the idea is to get closer to developing concrete cures. The general objective of this dissertation was to examine physiological mechanisms subjacent to individualized clinical phenotype in SCA6 and stroke.

Aim 1: To test the hypothesis that changes in brain connectivity precede overt symptomatology in SCA6.

Significance: SCA6 is an autosomal dominantly inherited degenerative disorder initially characterized by gait ataxia beginning in adulthood. In order to develop treatments however, it is imperative to determine the earliest changes taking place in the brain prior to the development of symptoms.

Challenge: There is a paucity of information on early functional or structural changes that occur in the brain prior to the appearance of gait ataxia.

Approach: Using structural equation modeling centered in cerebellum, we evaluated changes in effective connectivity in patients at different stages of disease severity, including pre-symptomatic individuals. In parallel, we determined structural changes (derived from DTI) in the same pathways.

Aim 2: To test the hypothesis that specific biophysical variables change global brain dynamics after stroke.

Significance: Damage caused by stroke produces widespread functional changes directly or indirectly associated with the primary lesion. Although current studies depicting network changes after stroke are informative (Carter et al., 2010, 2012; Grefkes and Ward, 2013; Rehme and Grefkes, 2013), there is a paucity of data associating those changes to biophysical variables limiting the usefulness of these studies.

Challenge: Until now, there have been no tools that allow the determination of biophysical variables associated with brain dynamics following stroke.

Approach: We used a neuroinformatics platform The Virtual Brain (TVB) to accurately simulate rest-state fMRI (rsfMRI) signals in individuals in the chronic phase of stroke and in age-matched controls. Changes in parameters associated with adequate simulations were then related to clinical phenotype.

Aim 3: To test the hypothesis that TVB can be used to model the effects of a "virtual therapy" on brain activity via biophysical parameter modifications.

Significance: Precision medicine is a common goal of neurology in the clinical and research fields. However, the identification of biomarkers of disease, and the ability to develop and test therapies in individuals is needed to achieve this.

Challenge: There are no tools to test individualized medicine prior to administration to individual patients.

Approach: We applied a "Virtual Therapy" to individuals with stroke by manually adjusting TVB parameters associated with stroke recovery to match those of healthy controls. We compared the simulated brain activity with empirical healthy brain activity, to determine whether adjusting the parameters resulted in a global improvement of brain dynamics.

CHAPTER 1

Sensitivity of Network Analysis in Detecting Early Brain Changes in SCA6

A. Spinocerebellar Ataxia Type 6 Background

Spinocerebellar Ataxia Type 6 (SCA6), is one of 37 autosomal dominant spinocerebellar ataxias, a group of genetic degenerative disorders characterized by a progressive lack of precision during voluntary movements (Brouillette et al., 2015). SCA6 is caused by a polyglutamine expansion in the CACNA1A gene (Zhuchenko et al., 1997), which encodes a transcription factor protein, α1ACT, that is important for neural and Purkinje cell development (**Figure 1.A**). When the expanded polyglutamine tract appears in this transcription factor protein, it loses its transcription factor function, causing cell death and cerebellar atrophy (Hekman and Gomez, 2015). Thus, the primary lesion is limited to the Purkinje neurons (Kordasiewicz and Gomez, 2007; Rüb et al., 2013) in the cerebellar vermis, followed by the intermediate and lateral hemispheres (Giunti et al., 2015; Schulz et al., 2010). Consequently, the initial signs and symptoms of SCA6, such as imbalance and gait ataxia, reflect decline in functions dependent on this region (Ashizawa et al., 2013; Schulz et al., 2010; Yasui et al., 2014). Because of this pathology, for years SCA6 has been referred to as a pure cerebellar ataxia, or one that affects only the cerebellum. However, more recent studies have shown that other brain regions are indirectly affected through transynaptic degeneration (Stefanescu et al.,

2015).

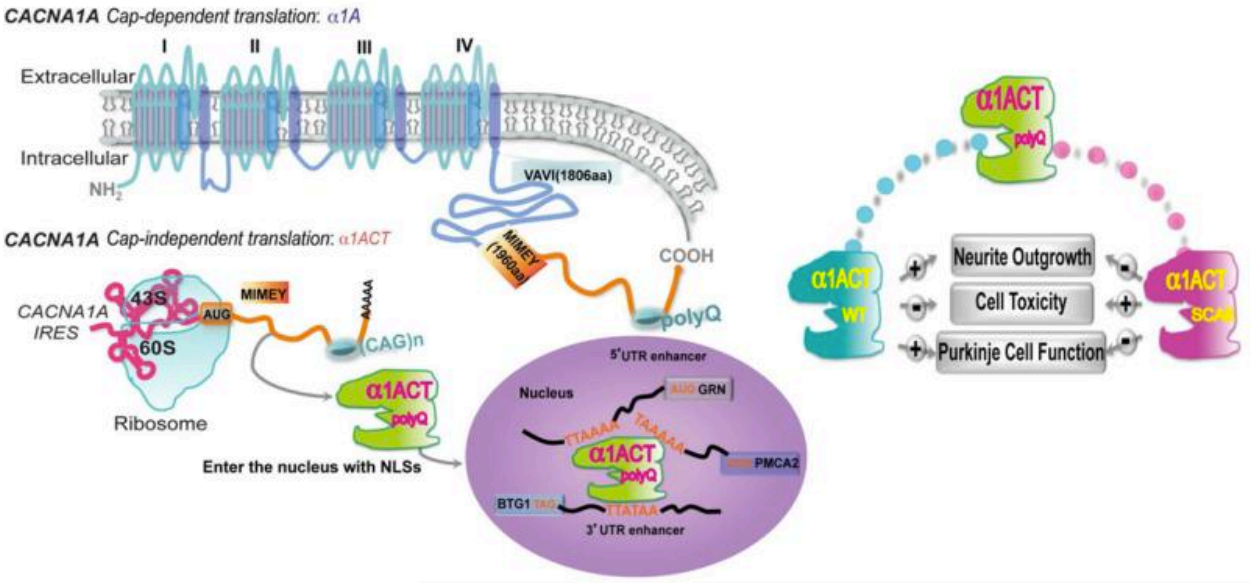

Figure 1.A. Schematic illustration of expression regulation and function of α1ACT. Expansion of the polyglutamine tract in SCA6 leads to pathogenic α1ACT, resulting in cell toxicity. Adapted from (Du et al., 2013)

There is currently no cure for SCA6. Molecular and genetic engineering treatments are being investigated in animal models, but are not yet ready for clinical implementation (Tsou et al., 2011). Hence, identifying additional biomarkers that can help determine prognosis would aid the development of treatments. Thus far, biomarkers, such as levels of specific proteins (alpha-synuclein, tau proteins, glial fibrillary acidic protein) have primarily been sought in the cerebrospinal fluid to compensate for the lack of accessibility to pathogenic tissues and the complexity of brain organization (Brouillette et al., 2015). While some of these proteins have shown to be associated with other neurodegenerative diseases, including other spinocerebellar ataxias, as of yet, significant correlations with SCA6 severity and have not been identified.

Other studies in SCA6 use human imaging to provide critical insight into the brain states of SCA6 patients at different stages of disease severity. For example, one such study assessed

functional and structural changes in the entire cerebellum and cerebellar nuclei and found a decrease in both size and fMRI signal in the cerebellar nuclei (Reetz et al., 2013; Sakakibara et al., 2014; Schulz et al., 2010; Stefanescu et al., 2015). While these findings are not directly reflective of a specific disease mechanism, they provide potential correlates of disease that could be measured non-invasively. However, this and other studies have only assessed brain changes at stages where overt atrophy and behavioral deficits were present; that is, patients were already symptomatic. Targeting changes at these later stages is ineffective at preventing ongoing disease processes. In contrast, exploring instead the pre-symptomatic stage can inform us of early changes of a system that may still be influence able. Given the progressive nature of the disease, the identification of early-stage, or pre-symptomatic stage biomarkers would be useful in providing targets for treatments that could act to prevent the development of symptoms. The goal of the work described in the following experiment was to use functional and structural network analysis to determine whether correlates of disease severity can be detected as early as the pre-symptomatic stage.

B. Early cerebellar network shifting in Spinocerebellar Ataxia Type 6

B.1. ABSTRACT

Spinocerebellar ataxia 6 (SCA6), an autosomal dominant degenerative disease, is characterized by diplopia, gait ataxia, and incoordination due to severe progressive degeneration of Purkinje cells in the vestibulo- and spino-cerebellum. Ocular motor deficits are common, including difficulty fixating on moving objects, nystagmus and disruption of smooth pursuit movements. In pre-symptomatic SCA6, there are alterations in saccades and smooth pursuit movements. We sought to assess functional and structural changes in cerebellar

connectivity associated with a visual task, hypothesizing that gradual changes would parallel disease progression. We acquired fMRI and DTI data during a passive smooth-pursuit task in 14 SCA6 patients, representing a range of disease duration and severity, and performed a cross-sectional comparison of cerebellar networks compared to healthy controls. We identified a shift in activation from vermis in pre-symptomatic individuals to lateral cerebellum in moderate to severe cases. Concomitantly, effective connectivity between regions of cerebral cortex and cerebellum was at its highest in moderate cases, and disappeared in severe cases. Finally, we noted structural differences in the cerebral and cerebellar peduncles. These unique results, spanning both functional and structural domains, highlight widespread changes in SCA6 and compensatory mechanisms associated with cerebellar physiology that could be utilized in developing new therapies.

B.2. INTRODUCTION

The autosomal dominant spinocerebellar ataxias (SCA) constitute a genetically heterogeneous group of neurodegenerative disorders characterized by progressive motor incoordination, consisting of either isolated (pure cerebellar) ataxia or ataxia with additional progressive neurological deficits (Maschke et al.). The worldwide prevalence of the SCAs is approximately 10/100,000. Spinocerebellar ataxia, type 6 (SCA6), which is among the most common forms of autosomal dominant spinocerebellar ataxia represents about 31% of the dominant SCA cases in Japan and 15% of cases in the US (Geschwind et al., 1997; Leggo et al., 1997; Matsumura et al.; Schols et al., 1998).

SCA6 is caused by a CAG repeat expansion in exon 47 of the CACNA1A gene, encoding the α1A (Cav2.1) subunit, the main pore-forming subunit of the neuronal P/Q-type voltage-gated

calcium channel (VGCC) (Zhuchenko et al., 1997) and is one of several clinically distinct, but overlapping dominantly inherited neurological disorders caused by distinct mutations in this gene. Additionally, it is one of ten neurodegenerative diseases that, like Huntington's disease, are associated with polyglutamine-encoding CAG nucleotide repeat expansions, although the polyQ tract encoded by the CACNA1A gene has a normal range of only 4-18 and in SCA6 is expanded only to 19-33 repeats, considerably smaller than all other polyQ diseases. The age of onset of symptoms correlates inversely with the size of the expansion. SCA6 has been described as the prototype of a pure cerebellar ataxia (Gomez et al., 1997; Mantuano et al., 2003; Yang et al., 2000), characterized primarily by Purkinje cell degeneration and cerebellar atrophy. In structural magnetic resonance imaging (MRI) of the brain, SCA6 demonstrates cerebellar atrophy affecting mostly the vermis and, to a lesser extent, the cerebellar hemispheres (Butteriss et al., 2005; Lukas et al., 2006; Murata et al.; Satoh et al., 1998). Neuropathological studies show a striking loss of cerebellar Purkinje cells with preservation of other brain regions although more recent reports suggest a more widespread involvement of cell loss (Reetz et al., 2013; Seidel et al., 2012). Cortical or cerebello-olivary atrophy is occasionally noted but attributed to transynaptic degeneration due to loss of Purkinje cells (Koeppen, 2005).

SCA6 is characterized by an adult onset, slowly progressive cerebellar ataxia, dysarthria, and nystagmus. Initial symptoms in SCA6 include gait unsteadiness, stumbling and imbalance in about 90% of individuals, with the remainder presenting with diplopia, oscillopsia, dysarthria, or episodic vertigo several years before the gait disturbance (Globas et al., 2008). Symptoms progress slowly, and eventually all affected individuals have gait ataxia, upper limb

incoordination, intention tremor, and dysarthria. Dysphagia and choking are common (Gomez et al., 1997).

Multiple ocular motor deficits in SCA6 are also common (Ackl et al.; Bour et al., 2008; Buttner et al., 1998; Gomez et al., 1997; Jacobi et al., 2013), and may precede overt gait and limb ataxia (Christova et al., 2008; Oda et al.). Diplopia occurs in about 50% of individuals. Others experience visual disturbances related to difficulty fixating on moving objects, as well as horizontal gaze-evoked nystagmus (70-100%) and vertical nystagmus (65-83%), compared with fewer than 10% of those with other forms of SCA (Gomez et al., 1997). Other eye movement abnormalities, such as periodic alternating nystagmus and rebound nystagmus, have also been described (Sasaki et al., 2003).

A large-scale study including 107 SCA6 patients (Jacobi et al., 2013) showed that the disruption of smooth pursuit movements had the highest prevalence (92.5%) of the ocular motor deficits. Additionally, by using sensitive eye movement recording techniques (Christova et al., 2008), alterations in saccadic (velocity and metrics) as well as smooth pursuit gain of eye movements in pre-symptomatic SCA6 subjects have been reported. Interestingly, both saccades and smooth pursuit eye movements are known to place a high computational demand on the cerebellum, particularly the vermis (Konen et al., 2005).

Objective:

In this study we sought to assess functional and structural changes in cerebellar connectivity associated with a visual task. We hypothesized that gradual changes in task-dependent cerebellar network connectivity would parallel progression of disease. To this end, we acquired fMRI and DTI data during a passive smooth-pursuit task in SCA6 patients and

performed a cross-sectional comparison of cerebellar networks from individuals at different stages of disease.

B.3. MATERIALS AND METHODS

Fourteen participants were recruited from The University of Chicago Ataxia Center and 20 age-matched control subjects (9 Female/11 Male, age range from 30 to 69 years, mean = 49.1 ± 11.91) were recruited from the local community. Individuals with pre-existing severe psychiatric or other neurological illnesses were excluded. The diagnosis of SCA6 was established by genetic testing at a commercial laboratory according to standard methods (Athena Diagnostics, Wooster, MA). Clinical disease severity was estimated using a validated ataxia rating scale (SARAII) performed on the same day as the imaging study by a single examiner (CMG)(Schmitz-Hubsch et al. 2006). The age of onset of the twelve affected patients ranged from 44 to 60 years (mean = 50.9 ± 4.7) and disease duration ranged from to 1 to 31 years (mean = 12.3 ± 9.2). The SARAII rating scale scores ranged from 2.0 to 26 (mean = 14.1 ± 7.4). In addition two subjects, age 52 and 63, bore a pathological repeat expansion, but were pre-symptomatic (SARAII = 0). These subjects did not demonstrate balance problems and also exhibited a minimal number of oculomotor problems. The demographics for all SCA6 subjects are listed in **Table 1.1**. SCA subjects were classified into 3 groups: "pre-symptomatic"-"early symptomatic" (SARAII 0-4), "moderate" (9-18), and "severe" (> 18.5).

This study and all procedures for recruitment and consent were approved by the Institutional Review Board of the Division of Biological Sciences of The University of Chicago.

Table 1.1 SCA6 Patient Demographics

Subject	Age (years)	Sex	SARAII	Repeat expansion	Age at onset (years)	Duration of disease (years)	Oculomotor symptoms (# out of 4)	Oculomotor signs (# out of 4)
1	55	F	10.0	22, 13	54	1	3	2
2	58	M	21.5	22, 13	48	10	2	3
3	52	M	4.0	22, 13	51	1	2	2
4	61	F	17.5	22, 14	44	17	--	--
5	73	M	22.0	Family history	48	24	2	3
6	63	F	18.5	22, 14	55	8	4	2
7	58	M	13.0	24, 11	48	10	1	3
8	68	F	15.0	22, 13	50	18	1	3
9	81	F	26.0	22, 16	50	31	3	3
10	62	M	9.0	22, 13	60	11	0	2
11	52	F	0.0	22, 13	0	0	2	0
12	59	F	2.0	22, 13	57	2	4	2
13	60	F	10.5	22, 14	46	14	3	2
14	63	M	0.0	22, 13	0	0	1	2

Assessment of oculomotor alterations

To assess severity of oculomotor deficits, the following signs and symptoms were determined during clinical evaluations: Symptoms: vertigo, diplopia, problems focusing, and oscillopsia. Signs: nystagmus, pursuits, saccades, and square wave jerks. For each subject, the

number of symptoms and signs present were quantified for a maximum of 4 for each (**Table 1.1**). This number was correlated with SARAII score using a Pearson's correlation.

Imaging

Imaging was performed using a 3T Philips scanner equipped with a SENSE head coil using higher order shims. Subjects were placed in the scanner, with head movement restricted by foam rubber pillows. Electrostatic headphones (Resonance Technologies, Northridge, CA) were placed on the ears and connected to a computer controlled stereo system. The computer was equipped with the PsyScope psychological software system (Cohen et al., 1993), which was used to present the experimental stimuli. Functional scans were acquired while participants passively viewed a 5-minute video that alternated between 20 seconds of rest and 20 seconds of visual stimuli. The visual stimuli showed different landscapes through the perspective of a walker as seen in the first person. Rest periods were visually neutral showing a static image of a starry sky on a black background. The visual stimuli were presented in videos and did not involve reflexive activity via vestibulo-ocular reflex (VOR) (the head of the participants was immobilized), or optokinetic reflex (OKR) (i.e. there were no objects moving along the visual field). Hence these global motion stimuli basically involved saccadic and smooth pursuit movements.

Structural Images. High-resolution T1-weighted three-dimensional magnetization prepared rapid gradient echo (MPRAGE) scans were collected: Field of view (FOV) =240 mm^2, resolution = 0.75 x 0.75 x 0.75 mm, SENSE reduction factor = 1.5, Repetition Time (TR)/Echo Time (TE) = 11/4.5 ms, flip angle = 18°, sagittal orientation, number of slices = 200 covering the whole brain.

fMRI. Blood Oxygen Level Dependent (BOLD) images were collected for the task-dependent functional images using single-shot echo-planar imaging (EPI), with FOV = 250 mm^2, TR/TE= 2000/30 ms, flip angle = 70°, in-plane resolution = 2 mm × 2 mm, slice thickness = 5mm, number of slices = 30 covering the whole brain.

Diffusion Tensor Imaging. DTI images were collected using a single shot echo-planar spin-echo sequence with the following parameters: total scan time = 8 min 15 sec, image volumes acquired using 32 different diffusion sensitizing gradient directions at b = 1000 sec/mm^2, flip angle =90°, FOV = 224 mm^2, resolution = 0.875 x 0.875 mm^2, slice thickness = 2 mm, number of slices = 60, TR/TE=1031/55 ms, SENSE reduction factor = 2, and EPI factor = 59. Two b=0 s/mm^2 images were acquired. All images were reconstructed to a 256 x 256 matrix.

Image Analysis

fMRI. Following acquisition, fMRI data were reconstructed and preprocessed using AFNI (Cox, 1996) as follows: (1) motion correction using a 6 parameter 3D registration of the functional and anatomical data sets (Cox and Jesmanowicz, 1999); (2) 3D spatial registration to a reference acquisition from the first fMRI run; (3) registration of functional images to the anatomical volume; (4) De-spiking; (5) mean normalization of the time series; and (6) inspection and censoring of time points occurring during excessive motion (>1 mm) (Johnstone et al., 2006).

Multi-subject analysis was performed using an anatomical region-of-interest (ROI) approach that included eight brain regions selected on the basis of the functional anatomy of the motor system including cerebellum and cerebral cortex. For the cerebellum, the anatomical parcellation was generated based on functional divisions: vermis, paravermal (intermediate,

intCRB) region, lateral cerebellum, and flocculus-nodulus, as we have done previously (Solodkin et al., 2011). Cerebral cortex ROIs were generated using automatic Freesurfer parcellation (Destrieux et al., 2010). Alignment of fMRI to the anatomical images and ROIs was manually confirmed.

Structural changes. Atrophy of each brain region was calculated based on the T1-weighted structural images normalized by cranial volume as previously reported (de Leon et al., 2001). The linearity of the relationship between the volume of cerebellar regions and disease severity was obtained by Pearson's correlation with probability values corrected for multiple comparisons (Bonferroni) (Armstrong, 2014). A two-tailed Wilcoxon Rank Sum test was used to compare volumes between the control cases and SCA6 cases.

Statistical Maps. Statistical analysis of individual subject data was performed using a multiple linear regression, in which the signal time course for each voxel was compared to a reference waveform. The reference waveform was based on the convolution of a square wave with an empirical model of the hemodynamic response (Cox, 1996). Voxels were considered active if the single voxel *p*-value was less than 1×10^{-5} and the voxel met a three-dimensional contiguity requirement, requiring clusters (sets of contiguous voxels) to contain at least three voxels (53 mm^3). These values were determined following a Monte Carlo simulation that established a corrected whole brain significance level ($\alpha < 0.05$) (Forman and Cohen, 1995). The resulting clusters that survived both the initial F-test and the clustering threshold defined the presence of activation in the brain for each subject. Group frequency maps for controls and each stage of SCA6 severity were generated to depict the fraction of subjects per group that had activation in each voxel. Finally, to ensure that atrophy of the cerebellar cortices did not

affect the amount of activation seen, we normalized active volumes by the total volume of each of the cerebellar cortices for each individual.

Effective Connectivity: Structural Equation Models. The secondary analysis was the construction of networks for corticocerebellar activity via effective connectivity. We built structural equation models (SEM), covariance structures constrained by known anatomy, using AMOS, as we have done before (Arbuckle, 1989, 1992). We measured the fit between predicted and observed covariance matrices using both χ^2 and explained variance to generate the SEMs (Solodkin et al., 2004; Walsh et al., 2008)**.** We generated both a group model (e.g., healthy controls) and individual models for each patient. To minimize variance within the group model, we modeled the time series from the peak voxel in each ROI as we have done before (Mashal et al., 2012; Walsh et al., 2008). To quantify model differences between the group control model and individual SCA6 patients, we used a ‘‘stacked model” approach (McIntosh and Gonzalez-Lima, 1994) as we have done previously (Solodkin et al., 2004; Walsh et al., 2008). A Bollen-Stine bootstrap analysis was also performed to test the null hypothesis that each model had a good fit with the data. Using this approach, for each model, the data was re-sampled and re-fitted for a total of 2000 iterations. The goodness-of-fit (χ^2) obtained from the original model was then compared with those generated from the re-sampled data.

DTI. Pre-processing (FDT diffusion toolbox of FSL; FMRIB Software Library) (Behrens et al., 2003) consisted of (1) correcting for motion and eddy current spatial distortions using an affine transformation with 12 degrees of freedom (*eddycorrect* function in FSL); (2) improving the tensor estimations by diffusion gradient reorientation (Leemans and Jones, 2009); (3) estimating diffusion tensors using a linear least squares approach (*dtifit* function in FSL) with

reconstruction of mean, axial, and radial diffusivities and fractional anisotropy (MD, AD, RD, and FA); and (4) manually segmenting the superior, middle cerebellar peduncles and the cerebral peduncles (ROIs) as we have done before (Walsh et al., 2008). Due to large partial volumes, the inferior peduncle was not included in this analysis. Corrections to the data were performed as follows: SCP, MCP and CP ROIs were manually drawn carefully to avoid the edges in the T1. We then applied a 12 degrees of freedom transformation to warp the T1 into b0 of the DTI. All ROIs were then visually inspected to ensure an accurate alignment. In the MCP and CP, because there was minimum distortion, and because we avoided the exterior portions, there were no errors to the alignment of those peduncles. Of the SCP ROI's that were mis-aligned, we then manually shifted those so that they overlapped more with the SCP as viewed in the diffusion images.

All DTI metrics (FA, MD, RD and AD) were extracted on a voxel-by-voxel basis from each ROI. Mean and median values of the diffusion metrics per group for each ROI were calculated. Voxel-wise frequency distributions for FA and RD in each fiber bundle were also calculated. Differences in distribution between the different SCA6 groups and the controls were performed and corrected for multiple comparisons with the Kolmogorov-Smirnov-test.

Deterministic diffusion tensor tractography was performed using a Diffusion Toolkit and Trackvis Software (Wedeen et al., 2008). The fiber assignment by continuous tracking, FACT, algorithm (Mori et al., 1999) was selected to create the tractography with stopping criteria of either a turning angle greater than 60 degrees or an FA value less than 0.20. From the tractography, the MCP, SCP, and CP were identified automatically and refined manually by removing obvious stray or false positive tracts from each peduncle. For each peduncle the

number of streamlines was calculated. Pathway weights were calculated via two methods: by multiplying the number of streamlines by the mean FA and mean inverse RD (1/RD) from all voxels with which each peduncle's streamlines intersected.

Age Correlations. To ensure that age did not affect the results, we performed a Pearson's correlation between age and all measures, including structural volumes, active volumes, and DTI measures, for the healthy control group.

B.4. RESULTS

Oculomotor Disorders along Disease Severity

Severity of SCA6, as assessed by SARAII score, was highly correlated with the number of oculomotor signs present on each patient ($r=0.72$, $p=0.0052$). However, there was no correlation between number of oculomotor symptoms and SARAII score ($r=0.21$, $p=0.4817$).

Structural Changes in Cerebellum

The degree of atrophy based on the normalized T1-weighted ROIs varied among patients (**Figure 1.1**) but on average, all cerebellar regions were atrophic in the SCA6 cases compared to controls (vermis, p=3.76e-8; intermediate, p=1.15e-9; lateral, p=7.66e-9). In addition, Pearson's correlation showed a significant relation ($p < 0.02$ after Bonferroni correction) between SARAII scores and the volumes of vermis ($r = -0.64$, $p = 0.013$) and the lateral cerebellum ($r = -0.66$; $p = 0.011$) but not for the intermediate cerebellum ($r = -0.58$; $p = 0.029$), as shown previously (Solodkin et al., 2011).

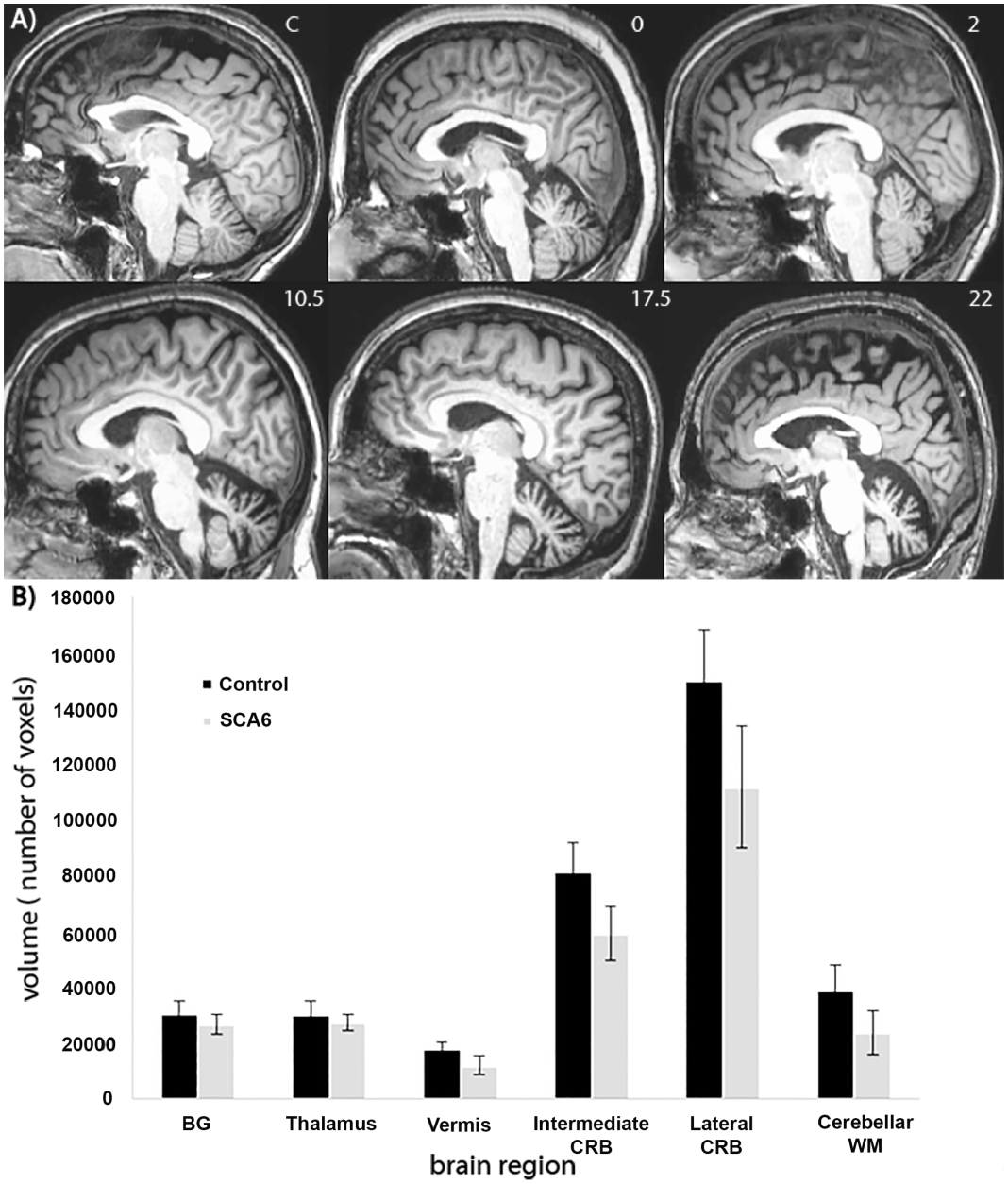

Figure 1.1 Volumetric assessment of brain regions in SCA6 and healthy controls.
A. Sagittal view of T1-w images in a healthy control (1), a pre-symptomatic SCA6 case (SARAII =0, (2)), moderate case (SARAII =2 (3), SARAII = 10.5 (4), and two severe cases (SARAII=17.5 (5), and SARAII =22 (6). Note the increase in cerebellar atrophy along an increase of SARAII scores.
B. Graphical representation of averaged brain region volumes and their standard deviation in healthy controls (black bars) and in SCA6 (gray bars).

Statistical Activation Maps

The distribution of brain activation during the visualization of the walking-landscape videos in healthy controls and SCA6 patients showed both similarities and differences (**Figures 1.2 and 1.3**). The stimuli evoked widespread activation in the cerebral cortex in all subjects, including premotor regions, the postcentral sulcus, the medial frontal gyrus (frontal eye fields, FEF), inferior and superior parietal (iPAR, sPAR) lobules (including the intraparietal sulcus) and widespread occipital areas (including MT and MST). In contrast, whereas increased activation in vermis and intermediate cerebellum was seen in healthy controls and pre-symptomatic cases, individuals with greater disease severity had less activation in these regions, and instead showed increased activity in the lateral cerebellum. Finally, individuals with the highest severity of disease were devoid of this lateral cerebellar activation. Results after volume normalization were consistent with those seen prior to normalization.

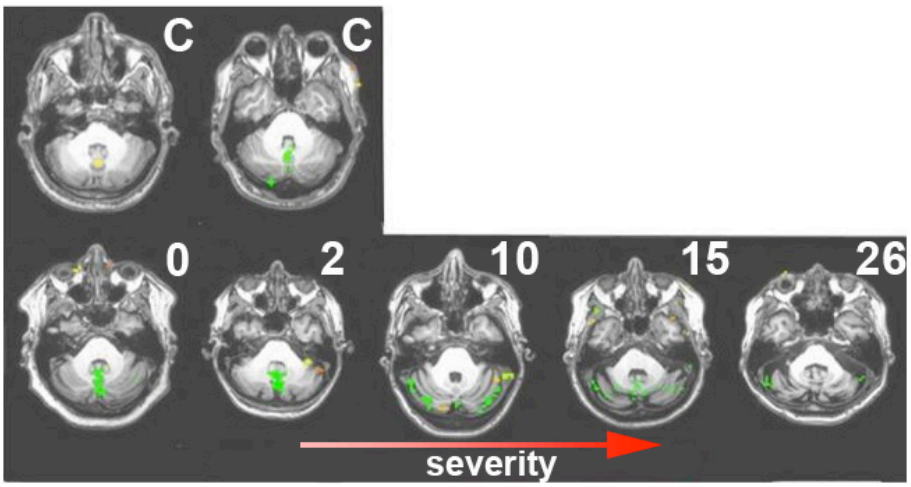

Figure 1.2 Functional brain activation in cerebellum during an eye movement task. Active volumes (yellow/green) shown in control cases (C) and in increasing severity cases of SCA6. Activation in controls is seen in cerebellar vermis that increases in pre-sympomatic and early cases (SARAII 0-2). Cases with mild severity (SARAII 10-15), see a decreased activation in vermis accompanied by an increase activation in lateral cerebellum which decreases in the more severe cases (SARAII =26).

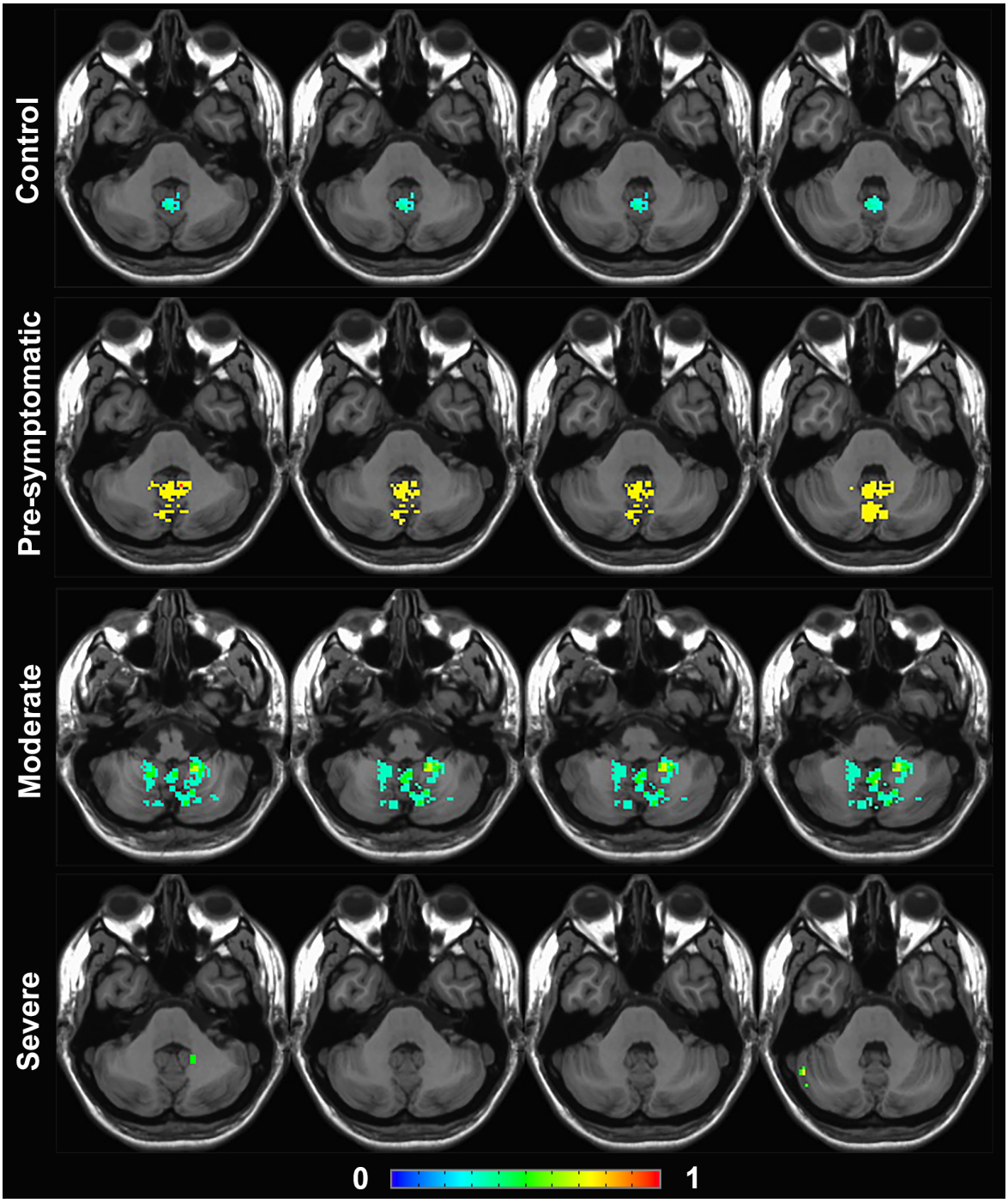

Figure 1.3 Group frequency maps of functional brain activation in cerebellum. Fraction of subjects with activation in each voxel is shown in control cases and in each stage of SCA6 severity (pre-symptomatic/early, moderate, and severe), with hotter colors depicting higher fraction of subjects. Note the increase in vermis activation in the pre-symptomatic/early stage, followed by a spread to lateral cerebellum in the moderate stage, and a decline in activity in the severe stage.

Effective Connectivity: Structural Equation Models

Given that the different functional regions of cerebellum (vermis-intermediate-lateral) are not intrinsically interconnected, the shifting of the activation from spinal to lateral cerebellum should originate extrinsically. Since the main input to lateral cerebellum comes from the cerebral cortex (via both pons and the inferior olives) that was heavily active during the task, we considered the cerebral cortex a suitable candidate mediating this shift. We used SEM analysis to assess effective connectivity between cerebral cortex and cerebellum (Walsh et al., 2008). All SEM models generated had a good fit ($\chi^2 > 0.06$) and each node had variance explained between 55-94%. Additionally, the Bollen-Stine boostrap analysis showed that all models had a good fit.

Group model for healthy controls

Connectivity among occipital and temporal regions exerted multiple influences over parietal regions that in turn influenced the FEF (**Figure 1.4**). In contrast, connectivity to and from cerebellum was more restricted since the intCRB was the sole locus establishing significant connections with iPAR and the FEF.

b) Network changes in SCA6

The networks associated with pre-symptomatic and early cases (SARAII = 2-4) shared features with the group control model; the connections between occipital and temporal regions and parietal and frontal regions remained constant. However, the strong connectivity between sPAR to iPAR seen in controls was not present, and a new association between the occipital regions and the FEF appeared at this early stage. Additionally, the activation in the intCRB was

driven by both the iPAR and the mTEMP (**Figure 1.4**; stacked model, p<3.6e-12; Bollen-Stine bootstrap, p=0.219).

In more advanced disease (SARAII 9-18), effective connections associated with the cerebellum showed profound differences compared to the group model (**Figure 1.4**; stacked model, p<3.2e-35; Bollen-Stine bootstrap, p=0.142). A new cortical influence on the intCRB included the occipital regions and more importantly, the lateral cerebellum at this point was driven by connectivity from mTEMP, inferior and superior PAR and the FEF. Concomitant with these changes was a disappearance of heavy influence between occipital and the FEF.

In the most advanced cases (SARAII > 18.5), cerebellar networks were less distributed. There was a paucity of connectivity between the cerebellum and the cerebral cortex along some cortico-cortical connections associated with mTEMP (**Figure 1.4**; stacked model, p<3.9e-26; Bollen-Stine boostrap, p=0.401).

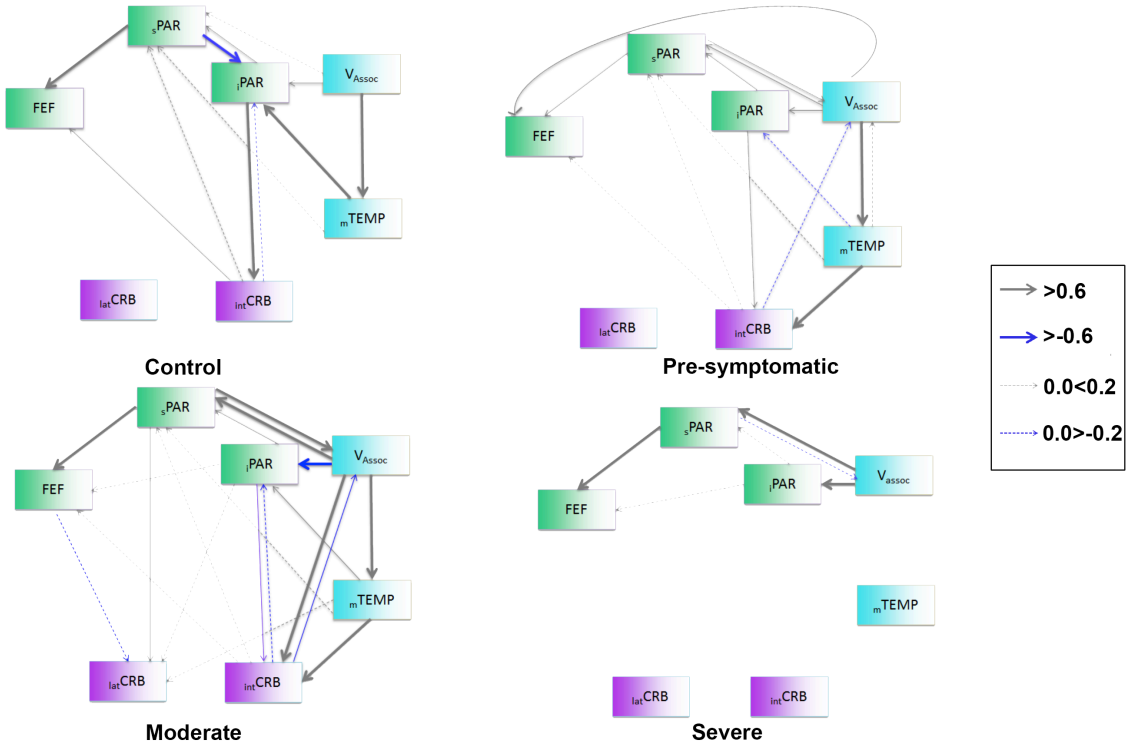

Figure 1.4 Structural equation model networks depicting the connectivity between cerebral cortex and cerebellum evolve with the development of disease.
The nodes (brain regions) have been color coded to denote 3 categories: Turquoise: visual related areas (Association visual areas (Vassoc), and visual-temporal MST, MT (mTEMP); Green: sensory-motor areas (superior Parietal (sPAR), inferior Parietal (iPAR) and frontal eye fields (FEF); Magenta: cerebellar regions (intermediate Cerebellum (intCRB) and lateral cerebellum (latCRB)). The thickness of the arrows denote the weight of connections; gray arrows showing positive correlations and blue arrows negative correlations. The influence of cerebral cortex increases early in the disease, becomes maximal in moderate cases to decrease below control levels in the most severe cases.

White Matter Changes

a) Peduncle Volumes

The average volumes of the superior and middle cerebellar peduncles (SCP and MCP) and the cerebral peduncle (CP) were lower in SCA6 cases compared to healthy controls (Wilcoxon Rank Sum Test: p = 0.0, 0.05, 0.05 respectively). In the MCP and CP, a trend towards reduced volume with increased disease severity was observed, beginning with pre-symptomatic

individuals continuing through the more severe cases (SARAII > 18.5) (**Figure 1.5**), though these changes were not statistically significant (Spearman's rank correlation).

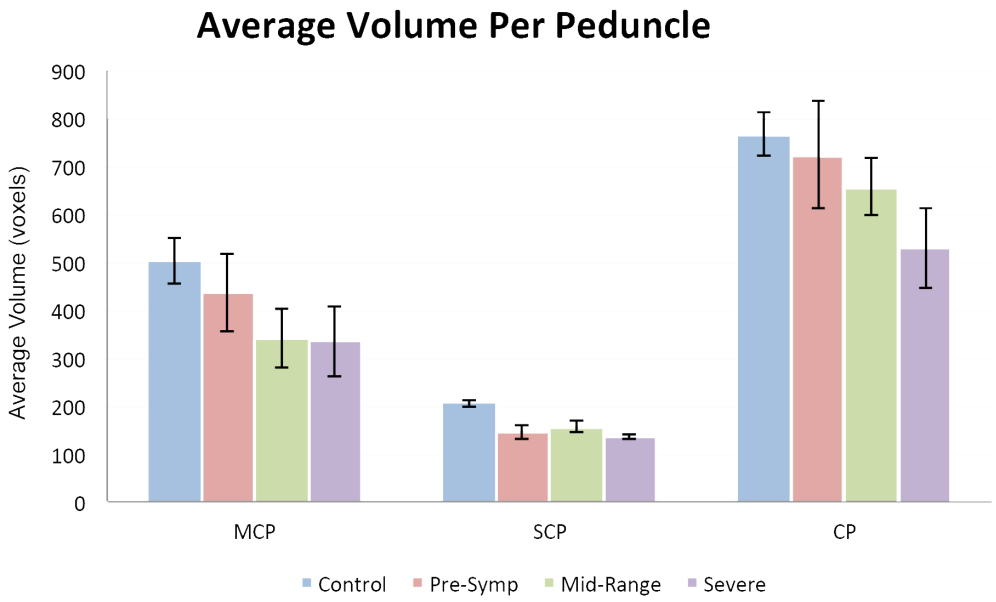

Figure 1.5 Graphical representation of the average size (and SD) of white matter tracts linking (indirectly) the cerebral cortex and the cerebellum.
Pathways included are: middle cerebellar peduncle (MCP), superior cerebellar peduncle (SCP) and cerebral peduncle (CP) calculated in controls (blue bars), pre-symptomatic (pink), moderate (green) and severe SCA6 (purple). Note that all peduncles have progressively reduced volumes in SCA6 compared to controls.

b) DTI Metrics

Superior Cerebellar Peduncle:

Changes in the SCP were the most salient compared to the other pathways studied (**Table 1.2, Figure 1.6**). The main difference when compared to controls was a decrease in RD in pre-symptomatic cases followed by a progressive increase in moderate and severe cases. This trend was inversed in FA whose values increased in pre-symptomatic individuals, subsequently decreasing in moderate and severe cases.

Middle Cerebellar Peduncle:

The MCP showed limited changes in DTI metrics along the progression of the disease. The differences were more apparent when comparing patient data to controls (**Table 1.2, Figure 1.6**) where an increase in RD apparent at all SCA stages.

Cerebral Peduncle:

The profile of DTI changes in the CP in some ways resembled those in the SCP (**Table 1.2, Figure 1.6**), although the magnitude of the changes was smaller.

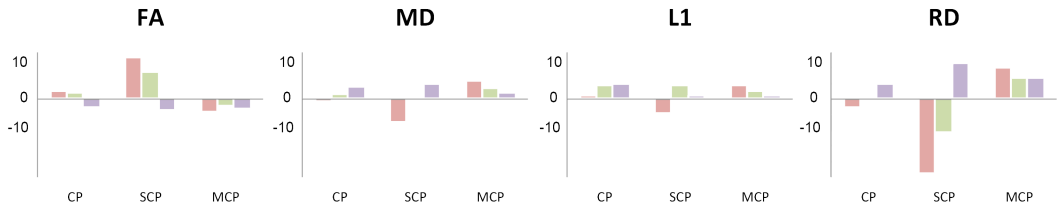

Figure 1.6 Percent change in DTI metrics of pathways of interest in healthy controls and SCA6 cases. FA = fractional anisotropy; MD = mean diffusivity; L1 = lambda 1 and RD = radial diffusivity. CP = cerebral peduncle, SCP = superior cerebellar peduncle and MCP = middle cerebellar peduncle. Percentage values in pre-symptomatic cases are depicted in red, moderate cases in green, and severe cases in purple. Note that the larger effects seen in SCP are repeated with less magnitude in the CP.

Statistical Distributions:

In order to understand the differences seen between SCA6 and controls with more precision, we performed analysis at the single voxel level to determine concrete differences in the statistical distributions as we have done before (Solodkin et al., 2013). This analysis comparing SCA6 to healthy controls with the Kolmogorov–Smirnov test showed significant differences in the distribution of FA and RD. The only comparisons that were not significant included the RD in the CP in the pre-symptomatic group and FA in the SCP in the severe group (**Table 1.3**).

We determined if there was a shift in the distributions of FA and RD between the control and the SCA6 groups. This analysis showed that in the CP, RD distribution compared to controls was shifted to the left in pre-symptomatic cases (p = 5.79 e -4) and moderate cases (p = 1.01 6 -6) and to the right in severe individuals (p = 6.53 e -25). In contrast, in the SCP there was a shift in the distribution of FA to the right in both pre-symptomatic (p = 5.97 e -20) and moderate individuals (p = 1.0 e -25). In severe cases, the trend inverted but the leftwards shift did not reach significance after correction for multiple comparisons (p = 8.0 e -3).

Table 1.2
Diffusion tensor metrics ± their standard deviation in pathways associated with cerebellum

	FA	MD	L1	RD
CP				
Control	5.74E-01±1.89E-01	7.72E-04±2.13E-04	1.35E-03±3.20E-04	4.87E-04±2.32E-04
Pre-Symptomatic	5.89E-01±1.93E-01	7.67E-04±2.16E-04	1.36E-03±3.17E-04	4.75E-04±2.40E-04
Moderate	5.87E-01±1.88E-01	7.85E-04±2.82E-04	1.40E-03±3.56E-04	4.89E-04±3.01E-04
Severe	5.60E-01±2.10E-01	8.03E-04±3.20E-04	1.41E-03±3.79E-04	5.10E-04±3.42E-04
SCP				
Control	6.83E-01±2.21E-01	8.59E-04±5.07E-04	1.76E-03±5.65E-04	4.48E-04±5.32E-04
Pre-Symptomatic	7.76E-01±1.78E-01	7.95E-04±3.27E-04	1.68E-03±4.48E-04	3.43E-04±3.15E-04
Moderate	7.44E-01±2.30E-01	8.60E-04±5.06E-04	1.84E-03±5.34E-04	4.01E-04±5.32E-04
Severe	6.58E-01±2.18E-01	9.03E-04±4.19E-04	1.78E-03±4.84E-04	4.99E-04±4.39E-04
MCP				
Control	6.61E-01±1.58E-01	7.19E-04±2.68E-04	1.37E-03±3.46E-04	4.03E-04±2.81E-04
Pre-Symptomatic	6.34E-01±1.62E-01	7.60E-04±3.00E-04	1.43E-03±3.66E-04	4.44E-04±3.10E-04
Moderate	6.47E-01±1.72E-01	7.46E-04±3.30E-04	1.41E-03±3.91E-04	4.30E-04±3.47E-04
Severe	6.40E-01±1.77E-01	7.35E-04±2.75E-04	1.39E-03±3.43E-04	4.30E-04±2.96E-04

FA = fractional anisotropy, MD = mean diffusion; L1 = lambda 1; RD = radial diffusivity.
CP = cerebral peduncle; SCP = superior cerebellar peduncle; MCP = middle cerebellar peduncle.

	Table 1.3 Probability values derived from Kolmogorov–Smirnov comparing SCA-6 groups versus healthy controls			
	DTI metrics	**Pre-symptomatic**	**Moderate**	**Severe**
CP	*FA*	4.59e-05	2.40e-05	2.75e-08
	RD	9.16e-02	1.38e-12	< 2.2e-16
MCP	*FA*	4.77e-09	1.02e-04	4.01e-06
	RD	< 2.2e-16	< 2.2e-16	3.17e-12
SCP	*FA*	< 2.2e-16	< 2.2e-16	7.56e-02
	RD	3.22e-09	2.60e-10	2.12e-03

Correction for multiple comparison level is: 4e -3.

c) Peduncle Weights

The structural weights of each peduncle normalized by FA (FA*number of streamlines) and by RD (1/RD*number of streamlines) were decreased in SCA6 compared to controls (**Figure 1.7**). In the CP, weights were significantly decreased in SCA6 when compared to controls for both FA-normalized weights (p=0.0013, t-test) and RD-normalized weights (p=0.0028, t-test). In the SCP and MCP, the decrease in RD-normalized weights followed a linear trajectory, where the weight correlated with SARAII score significantly for both peduncles (p=0.0105 and p=0.0452 respectively, Pearson's correlation). The decrease in FA-normalized weights correlated with SARAII score significantly only in the MCP (p=0.0073, Pearson's correlation).

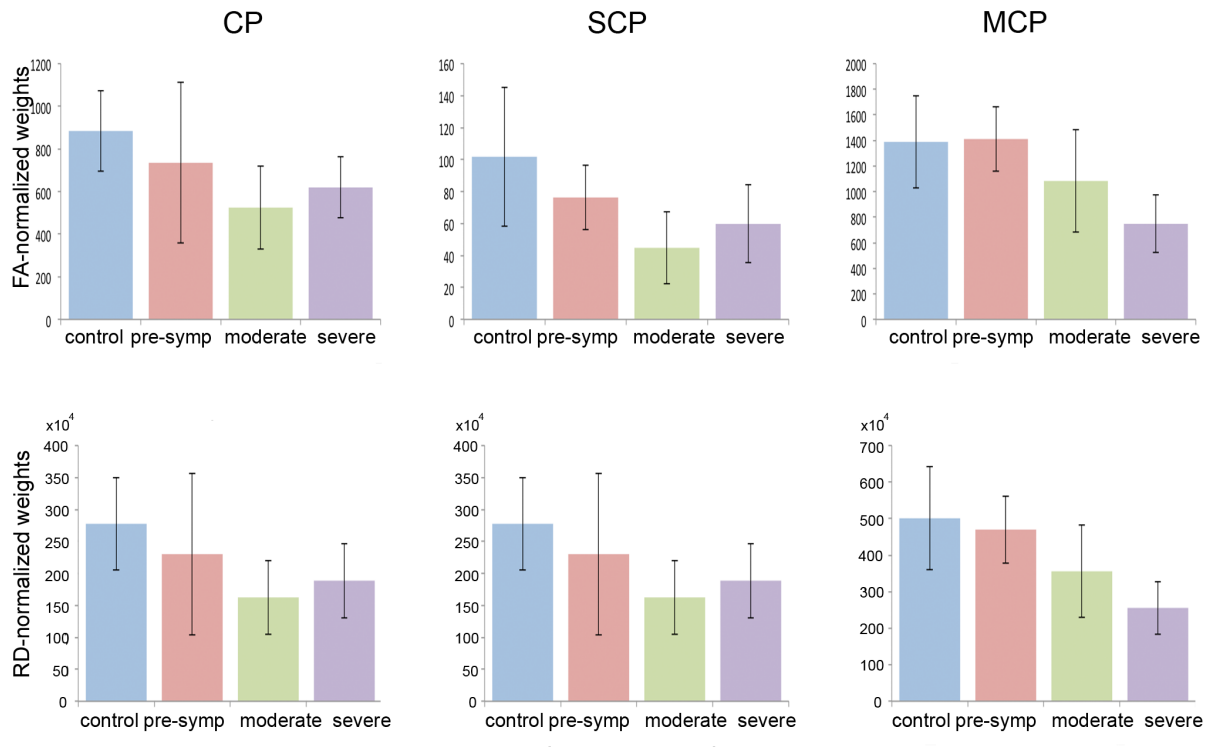

Figure 1.7 Structural weights of white matter peduncles in healthy controls and SCA6 cases. FA= fractional anisotropy; RD= radial diffusivity. CP= cerebral peduncle, SCP= superior cerebellar peduncle and MCP = middle cerebellar peduncle. FA-normalized weights = FA*number of streamlines. RD-normalized weights= (1/RD)*number of streamlines. Control cases are depicted in blue, pre-symptomatic cases in red, moderate cases in green, and severe cases in purple. Note that the RD-normalized weights decrease significantly along disease severity for the SCP and MCP whereas FA-normalized weights decrease significantly along disease severity only for the MCP.

Age Assessment

There was no correlation between age and any of the DTI metrics (FA, MD, RD, and L1) for all peduncles in the healthy control group ($p>0.05$, Bonferroni correction threshold set at 0.0042 for significance). In addition, there was no relationship between age and total activation in each cerebellar hemisphere (Bonferroni correction, $p=0.0083$). Therefore, none of the current results reported were confounded by age effects.

B.5. DISCUSSION

Patterns of cerebellar activation are associated with disease severity

A salient result of the current study is the increase in BOLD volumes and subsequent shift of activation from vermis (in controls and pre-symptomatic individuals) to the lateral cerebellum in moderate and severe SCA6 cases during a visual task involving saccades and smooth pursuit movements. Whereas vermal fMRI activation in controls is not surprising because of its ample role in the regulation of saccades (Kheradmand and Zee, 2011; Liem et al., 2013; McDowell et al., 2008), the increase in activation in pre-symptomatic SCA6 patients could be due to the early alterations in saccadic movements (Christova et al., 2008). In contrast, the shift of activation from spino- to cerebro-cerebellum in moderate and severe SCA6 cases is intriguing since these functional cerebellar regions have marked differences in connectivity: the former with somatosensory nuclei in the spinal cord and medulla and the latter with the cerebral cortex (Prevosto and Sommer, 2013; Stoodley and Schmahmann, 2010). In order to understand these changes better, we further investigated functional and structural connectivity of cerebellar circuits.

Patterns of cerebellar connectivity can be described in stages

Effective connectivity models in healthy controls during the visual task show two salient links: 1) a feed-forward influence of visual association cortices (occipital and temporal) on parietal regions that in turn influence the FEF and 2) a top-down modulation of the paravermal cerebellar region from the iPAR lobule. This pattern is in agreement with a previously described cortico-cortical network (Lynch and Tian, 2006) suggesting that saccadic and smooth pursuit movements critically depend on two hubs, one in the temporal lobule (regions MT, MST)

encoding motion in a retinal coordinated system and the FEF representing the motor output (Voogd et al.). Links between and toward these hubs are formed by association regions in the parietal lobule, and by occipital visual regions providing sensory input to the temporal hub.

Early changes in effective connectivity were detected in SCA6 pre-symptomatic cases and continued throughout disease progression. Based off of these changes, we classified three stages of disease severity that also paralleled progressive SARAII scores, average number of oculomotor signs, and patterns of fMRI activation. The progression of connectivity changes linked to each stage is as follows:

***Stage 1 (SARAII=0-4, 1.5 average oculomotor signs)*:** Contrary to early assumptions regarding the pathology of SCA6 as a uniquely cerebellar ataxia (Zhuchenko et al., 1997), we show that cortico-cortical connectivity is functionally altered early with a decrease in the strength of connections among parietal cortices and increased effective connections between occipital regions and the FEF. This reorganization at the level of cortico-cortical connectivity is accompanied by an increase of novel top-down influences from the temporal regions to the intermediate cerebellum. Because the reorganization of effective connections in pre-symptomatic and early symptomatic subjects runs parallel to the increase in vermal activation, we explored the possibility of a top-down influence from FEF to vermis using SEM (Voogd et al.). However, we were unable to achieve a good model fit. Thus we hypothesize that an alternative explanation for this increased activation could be the result of a decrease in cerebellar efficacy resulting from the primary damage to Purkinje neurons in vermis that occurs early in the disease (Cricchi et al., 2007). In turn, this additional activation can indirectly

generate a systemic modulation of the cerebral cortex via the ascending reticular system (Eccles et al., 1975) producing the cortico-cortical reorganization detected at this stage.

***Stage 2 (SARAII=9-18, 2.4 average oculomotor signs)*:** Characterized by the appearance of new functional descending control from several cortical regions (FEF, mTEMP, iPAR, sPAR) onto the lateral cerebellum, this is the critical point at which the activity originally located in the vermis during the visual task is now decreased and instead, lateral cerebellum is now active. Previous fMRI studies have shown that saccadic movements produce consistent activation of the vermis and the paravermal regions (for review see (Voogd et al.)) and the lateral hemispheres only if the visual task implies a cognitive load such as attention or memory demands (Nitschke et al.; Stephan et al., 2002). This perspective fits with the traditional view that the modulation of eye movements by the cerebellum is associated with the vestibulocerebellum for reflexive modulation (ex. VOR), the control of dynamics of saccades and smooth pursuit by the spinocerebellum (Kheradmand and Zee, 2011; McDowell et al., 2008), and modulation of complex eye movements involving cognitive demands by the cerebro-cerebellum (Koziol et al., 2014; Prevosto and Sommer, 2013; Schmahmann and Caplan; Strick et al., 2009). Thus the mechanism for the shift in activation from spino- to cortico-cerebellum is intriguing since anatomically there is no intrinsic connectivity linking them and behaviorally there is a clear difference in the roles associated with each cerebellar domain. In Stage 2, although volumes of activation in the cerebral cortex do not change, cortico-cortical effective connections do change, increasing in number and strength between many regions and thus generating a different neural context (Walsh et al., 2008). This stronger cortico-cortical network can in turn produce a concomitant increase in top-down regulation in widespread regions in

cerebellum. That is, as the weight of the cortico-cortical connections increases, these cortical regions expand their influence on to the lateral cerebellum. In turn, this up-regulation of the activity in lateral cerebellum can produce positive feedback back to cerebral cortex via the SCP.

***Stage 3 (SARAII>18, 2.75 average oculomotor signs)*:** This stage is characterized by a paucity of any significant influence from the cerebral cortex to the cerebellum despite the persistence of some relatively stable cortico-cortical connections. At this stage, cerebellar degeneration becomes generalized and in consequence, it is possible that transneuronal degeneration affects additional brain regions including primary motor cortex, brainstem nuclei, thalamus and basal ganglia (Gierga et al., 2009; Wang et al., 2010a). As a consequence of this widespread cerebellar degeneration, its influence over cortical upper motor neurons can decrease and hence along the descending influences. This decrease in effective connectivity has also been related to atrophy associated with other neurodegenerative disorders (Dennis and Thompson, 2014; Thomas et al., 2014).

The activation shift may be a compensatory mechanism against neurodegeneration

It is interesting to speculate whether the activation shift has an adaptive, functional role reminiscent to what occurs after motor stroke where brain regions are recruited to control upper extremity movements (Grefkes et al., 2008; Ward and Cohen, 2004) or to increase activity in degenerative disorders that modulate the progression of symptoms (Klöppel et al., 2009; Savioz et al.; Scheller et al., 2013). The involvement of the lateral cerebellum in SCA6 may be interpreted as a compensatory response to either maintain functionally sound eye motor control in the presence of vermal degeneration (Klöppel et al., 2009) or by prolonging the anatomical integrity of regions not yet in overt degeneration.

Because vermal degeneration appears early in the disease (Cricchi et al., 2007) followed by other cerebellar regions (Greschwind and Galaburda, 1987; Sasaki et al.), we suggest a compensatory mechanism associated with the survival of cerebellar regions not yet in degeneration (a.k.a. lateral cerebellum). Several mechanisms are thought to drive compensatory activity, including synaptic scaling, increased size of surviving synapses, neuritic outgrowth, and firing rate regulation (Abuhassan et al., 2014; Savioz et al.). Another alternative is the recruitment of silent synapses, which refer to connections without physiological effect when the presynaptic neuron is activated, that become active under certain pathological conditions (Atwood and Wojtowicz, 1999; Jahromi and Atwood, 1974). One of the proposed mechanisms by which silent synapses become active is based on homeostatic plasticity (Cabezas and Buño, 2011; Funahashi et al., 2013; Kerchner and Nicoll, 2008; Wojtowicz et al., 1991), where global activity modulates the synaptic strength (Nakayama et al.; Savioz et al.).

In the cerebellum, silent synapses have been suggested to account for 80% to 98% of synapses between parallel fibers and Purkinje cells (Dean et al., 2010; Ito, 2006; Losi et al., 2002). These become functional with repeated stimulation (Ito, 2006; Porrill and Dean, 2008) elicited by either LTP or LTD (Hess et al., 1996; Hoffland et al., 2012). Hence, the novel top-down activation from cerebral cortex to the lateral cerebellum could in fact activate these silent synapses and thus delay the ongoing disease-related damage.

Functional network changes are accompanied by structural pathway changes

While pathway degeneration associated with overt neuronal death is detectable, methods to assess structural changes in pathways associated with functional regulation were not obvious until recently (Hagmann et al., 2008). One can expect that overt degeneration of

Purkinje cells in moderate and severe SCA6 cases produces increased RD, decreased FA and decreased number of streamlines in cerebellar peduncles with the consequent decrease in the weight of these pathways. Smaller degenerating pathways in turn can result in lower levels of cerebral cortex activation.

In contrast, expected changes in pre-symptomatic cases or in the cerebral peduncles (far removed from Purkinje degeneration) are harder to imagine. Yet the SCP, the main output from cerebellum to the cerebral cortex via thalamus, shows not only the largest changes in pre-symptomatic and early symptomatic SCA6 patients, but also these results are counterintuitive. Opposite to the effects of degeneration, in the SCP, RD *decreases* more than 20% and FA increases more than 10%. Concomitant to this, there is a decrease in peduncle volume, number of streamlines and pathway weight that could be explained by the presence of thinner axons compared to those in healthy controls. Thinner axons would act as barriers to water flow in the radial direction both intra and extra-cellularly, causing the decreased RD and increased FA seen in early cases (Beaulieu; Nilsson et al.; Song et al., 2002) and potentially producing an increase in variance of activation in cerebellar outputs (Seidl et al.; Swindale). Afterwards, the typical increase in RD and decrease in FA is detected. This result is not surprising in the most severe cases since a recent report showed degeneration of the dentate nucleus in SCA6 where the pathway originates(Stefanescu et al., 2015). The pathway size and number of streamlines does not decrease parallel to this, perhaps due to partial volume effects in this small pathway.

Surprisingly, the CP shows similar trajectories to those seen in the SCP, although on a smaller scale probably due to the direct contact of SCP with the primarily degenerating Purkinje neurons on the one hand, and the heterogeneous anatomical composition of the CP on the

other (Ramnani, 2006, 2012; Wakana et al.). Of the many pathways comprising the CP, it may be expected that the cortico-pontine fibers would be the most affected. As the illness progresses, the remaining pathways within the CP may be affected (Smith, 1975; Uchino et al.) as degeneration in SCA6 spreads including layer V neurons in M1 (Gierga et al., 2009). At this point, the MCP, which forms the input from pons to cerebellum, is also affected perhaps in the anterograde and retrograde directions as a consequence of cerebellar degeneration (Ishikawa et al., 1999; Sasaki et al.).

When detecting decreased FA and increased RD, it is worth addressing a limitation of the diffusion tensor model, the effect of partial volume voxels containing tissue and CSF, which would exaggerate RD values and reduce FA (Vos et al.). Under these conditions, the number of streamlines can be underestimated by the premature termination of the tracking algorithm. However, two key points suggest this was not the case in our calculations. First, although the peduncle most likely affected by CSF is the SCP due to its location and small size, early cases display an initial decrease in RD followed by a decrease with disease progression. Second, this trend is also seen in the CP, which because of location and size should not have this potential artifact.

Summary

Key findings in this study reveals parallel structural and functional changes in different stages of SCA6. Importantly, although SCA6 is commonly referred to as a pure cerebellar ataxia, our observations demonstrate widespread functional changes involving the cerebral cortex even before the first clinical symptoms have manifested. Finally, we propose that those changes

have a compensatory nature, allowing the cerebellum to counteract or delay the effects of the neurodegeneration, making them essential in understanding the nature of SCA6 pathology.

C. Comments on SCA6 Findings

This study provides direct evidence of the sensitivity of network analysis to detect early functional changes associated with a degenerative neurologic disease. Further, the reported functional changes were paralleled by structural network changes. The pre-symptomatic stage has been explored extensively for biomarkers in neurodegenerative diseases, particularly in those with a genetic component as we did in this case (Bohanna et al., 2008; Hersch and Rosas, 2008). Previous prodromal studies have identified imaging correlates in several neurodegenerative diseases, particularly in Huntington's Disease (Abdulkadir et al., 2013). However, such correlates have not been limited to diseases with genetic ties. For example, a recent study assessed the integrity of the parahippocampal white matter using DTI in a cohort of patients with mild cognitive impairments (MCI) but who were not yet diagnosed with Alzheimer's Disease (AD), and using this measure, correctly predicted the subset of MCI patients who later converted to AD (Solodkin et al., 2013). The results reported here are in accordance with these previous studies, as they suggest that in pre-symptomatic individuals with SCA6, biological processes occur throughout the brain that result in a progressive re-arrangement of brain circuitry both functionally and structurally, beyond the region of primary lesion (cerebellum). Because of the observed increase in utilization of the cerebellar and cortical regions and pathways that are not primarily affected by the disease, we believe that this re-arrangement could be interpreted as compensatory, acting to preserve the remaining healthy areas of the cerebellum, and thus making the pre-symptomatic stage of disease a

promising time point for future investigation. Notably, it is still unknown at what point in the subject's life such changes are detected. Due to the mechanism of cell death, which inhibits proper development of Purkinje cells (Hekman and Gomez, 2015), it is plausible that individuals with SCA6 see differences in brain structure and function since birth.

While these findings describe network level brain changes, they lack ties to functional mechanisms at the mesoscopic level. Consequently, despite the promise of these findings, the results do not constitute clinically viable biomarkers of SCA6, and cannot serve as targets for treatments. However, this study could influence future work in animal models of SCA6 by providing evidence that the pre-symptomatic or even initial brain state in SCA6 exhibits altered physiology. In terms of human studies, the next step in the search for biomarkers of disease is to use sophisticated modeling methods to access the direct biological processes of disease in living human subjects. These methods are explored in the following chapters.

CHAPTER 2

Background: Connectivity and Stroke

Ischemic Stroke is defined as any episode of acute neurological dysfunction, persisting 24> hours or until death, due to obstruction of a blood vessel supplying blood to the brain (Sacco et al., 2013) and resulting in neuronal death. The acute phase is followed by subacute and chronic stages involving a number of degenerative and reparative processes (Cramer, 2008).

An outstanding issue in treating stroke is the heterogeneity of stroke recovery across individuals, which depends on a plethora of factors, including but not limited to: age, infarct size and location, pre-stroke conditions, severity of initial deficits and breadth of deficits, acute stroke interventions, post-stroke therapy and medications (type, amount and duration), medical complications post-stroke, depression, socioeconomic status, caregiver status, and genetics (Cramer and Riley, 2008; Pearson-Fuhrhop et al., 2012). As a result, brain plasticity, defined as "changes in neural organization which may account for various forms of behavioral modifiability, either short-lasting or enduring, including maturation, adaptation to a mutable environment, specific and unspecific kinds of learning, and compensatory adjustments in response to functional losses from aging or brain damage" (Berlucchi and Buchtel, 2009), varies across stroke patients. Consequently, no singular therapy or treatment is equally effective for all individuals who have suffered a stroke, perpetuating the need for personalized treatment plans.

Studies based on resting state fMRI (rsfMRI) show it is becoming a popular tool of mapping the changes to functional brain networks after stroke since it provides a direct

measure of both interactions between brain regions and a large-scale view of whole-brain systems(Carter et al., 2012). These studies typically calculate resting state functional connectivity (rsFC) by finding the pairwise covariance of the rsfMRI time series between regions, often the Pearson correlation coefficient, allowing for the assessment of the entire brain network ((Hartman et al., 2011; Hlinka et al., 2012); **Figure 2**).

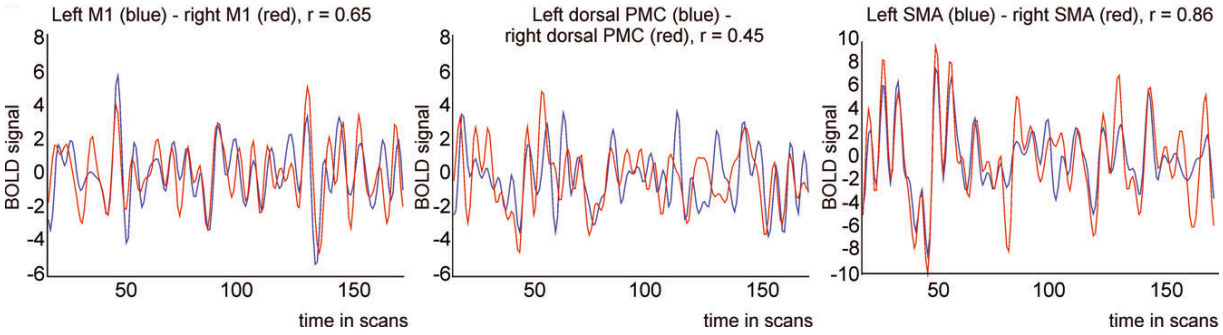

Figure 2. Pearson correlation coefficients between BOLD signal time-courses from homologous motor areas. Time series are averaged across 16 healthy subjects. Adapted from (Rehme and Grefkes, 2013).

Recent studies utilizing this approach have confirmed that lesions in parts of a motor network can cause dysfunction on remote brain regions (Carter et al., 2010; Grefkes et al., 2008; van Meer et al., 2010). These changes in widespread connectivity may be a strong influence on post-stroke deficits and recovery. Additionally, while the relationship between functional organization and behavioral performance is still being explored, recent findings using rsfMRI highlighted the role of homologous inter-hemispheric connections in improved motor function (Carter et al., 2010) and their strengthening was correlated to motor recovery (Grefkes and Ward, 2013; Wang et al., 2010b). There has also been evidence that inter-hemispheric connectivity between specific regions, such as regions within the central sulcus (M1 and S1), may correlate more strongly with motor function than other regions (Carter et al., 2010).

Finally, current approaches doing graph analysis at the whole brain level ("connectomics", i.e. the mapping of the brain's structural and functional connectivity and their interrelationship (Smith et al., 2013; Sporns, 2014)) have shown that stroke produces changes in both structural and functional network connectivity, particularly related to the organization of "hubs", or regions with high connectivity (Crossley et al., 2014; Sporns, 2014). Taken together, these findings demonstrate the value of connectivity analysis in detecting network disturbances from stroke that "may enable the development of diagnostic tools or biomarkers" (Sporns, 2014). However, such biomarkers typically operate at the network level, with no direct link to basic mechanisms of disease.

While functional network analyses and connectomics can provide further insight into brain plasticity in stroke, they lack any elements linked to concrete biological variables responsible for these changes. Biological variables describe biophysical processes underlying brain dynamics that operate on a microscopic or mescoscopic scale. Specifically, microscopic level biological variables describe characteristics in single neuron models, while mesoscopic level biological variables describe emergent dynamics within small populations of neurons (Deco et al., 2008). While global, or macroscopic level models can inform us on whole-level brain dynamics and interactions between large-scale neural systems (Deco et al., 2008), they lack insight into these biological variables. The closest modeling approach with "embedded" or "indirect" functional considerations applied to a number of brain regions has been Dynamic Causal Modeling (DCM) (Friston et al., 2003). However, while Dynamic Causal Models are rich with variables that reflect biophysical processes (Roebroeck et al., 2011; Stephan et al., 2010), they are intrinsic to the modeling (typically defined as "hidden" state variables) and have

constant values (priors) (Friston et al., 2003). Thus, the only output of such models are the weights of connectivity between regions of the brain network, and they can only be applied to a limited number of brain regions (typically three to six regions) (Daunizeau et al., 2011; Lee et al., 2006; Roebroeck et al., 2011). Consequently, according to Smith and Van Essen, one of the major challenges in the field of functional modeling and connectomics "*will be to enable application of biologically interpretable models using large numbers of nodes in a robust and practical way*" (Smith et al., 2013). The Virtual Brain (TVB), developed by Drs. AR McIntosh and V. Jirsa as part of an international consortium of which we are a site, is unique in this effort since it closes that gap(Jirsa et al., 2010; Ritter et al., 2013a; Sanz Leon et al., 2013). TVB arises from the consideration that biological brain signals are generated by the interaction of two elements: a) long range connectivity (derived from structural connectomics via diffusion tensor imaging) establishing the influence of brain regions on each other and b) local region dynamics governed by population physiology established by evolution equations reminiscent of those by Hodgkin and Huxley at the single neuron level. TVB includes mesoscopic theoretical models governed by specific physiological dynamics, described in detail later. In other words, by integrating long-range dynamics associated with specific connectivity variables, and local dynamics represented by mesoscopic neurobiological models, TVB modeling simulates biological signals at the whole brain level.

Ultimately, current research in stroke should aim to better understand the basic physiological nature of damage and plasticity following stroke in order to find targets for long-lasting gains. Specifically, studying structural and functional brain connectivity after stroke as opposed to focal deficits is becoming a robust approach to understanding global effects of the

lesion(Carter et al., 2012; Smith et al., 2013; Sporns, 2014) and has already been successful at identifying network differences in healthy and stroke brains. However, these results lack sufficient insight into the neurobiological mechanisms underlying network changes in stroke.

The work described over the following chapters encompasses several new approaches regarding stroke and recovery. First, Chapter 3 investigates finger individuation in the context of motor learning in healthy controls. Finger individuation is a phenomenon that contributes to humans' ability to perform fine motor movements, and is dependent on the integrity of the cortico-spinal tract (CST) (Lemon et al., 1986). The CST is composed of several descending tracts from the cortex to the spinal cord, including those originating in the primary motor cortex (M1), premotor areas, and supplementary motor areas, and finger individuation is most commonly thought to depend on the tract originating from M1 (Small et al., 2013a). A stroke in which the lesion affects this tract has been shown to cause a loss in finger individuation (Lang and Schieber, 2003; Schieber et al., 2009), resulting in decreased dexterity and the ability to perform fine motor movements. Therefore there are several recent rehabilitation therapies aimed at improving finger individuation. The work done in Chapter 3 is the first experiment to study finger individuation in the context of motor learning, to provide a baseline comparison for the re-learning of finger individuation after stroke.

The organization of the CST and its role in stroke recovery is probed with the work in Chapter 4. Recent studies have shown that tract-specific injury is a strong predictor of motor recovery (Riley et al., 2011; Stinear et al., 2007), with the tracts originating in M1 and premotor areas demonstrating equal predictive power. Action Observation Therapy (AOT), a novel rehabilitation therapy based on the idea that recovery of fine motor skills is better achieved

through remediation (the reparation of the original pathway), than compensation (the utilization or formation of an entirely new pathway), has been shown to increase excitability in the CST (Small et al., 2013b). Taken together, these results might suggest re-organization at the level of the CST during AOT, which might be more beneficial for those patients who have less damage to the M1 and pre-motor tracts. While prior studies have established the efficacy of AOT in the short term (Buccino, 2014; Small et al., 2013a), this study aims to identify network level changes both at rest (resting fMRI) and during a sequential finger tapping task that correlate with long-term motor recovery in a cohort of individuals with stroke who underwent AOT.

The experiments comprising Chapters 5-7 focus on finding biomarkers that are directly related to physiological mechanisms associated with stroke using The Virtual Brain. While the previous chapters study group level changes, these studies use a sophisticated level of individualized modeling via The Virtual Brain to identify discrete physiological variables determining brain dynamics that can be associated with successful recovery in the long-term (Chapter 5), and to virtually test the viability of these physiological variables as targets for therapies (Chapter 7). We also utilize graph theory and stability measures to gain deeper insight into the parameters of the TVB (Chapter 6). The results from this approach have the potential to greatly enhance the field of stroke recovery by providing specific neurobiological targets for the development of individualized treatment strategies.

CHAPTER 3

Lack of finger individuation during motor adaptation

A. Abstract

Finger individuation describes the extent to which the motor system can move one finger without moving the other fingers. To compliment this traditional definition, in this study we looked at whether motor adaptation of one finger influences its neighboring finger. Unimpaired adult subjects adapted to a resistive viscous force field applied to either the index or middle finger with a novel robot as they flexed their fingers sequentially to play the virtual notes of a musical computer game. When the force was first applied, the perturbed finger slowed as it played notes. It also exhibited hyper-velocity movements when the field was removed. This pattern is consistent with formation of a predictive model of the viscous perturbation by the perturbed finger controller. For the unperturbed finger, changes in dynamic environment applied to the perturbed finger affected its speed, although it did not directly experience mechanical resistance. Specifically, the unperturbed middle finger controller erroneously increased its velocity when it played notes following a brief period of adaptation by the perturbed index finger, and slowed its velocity when the field was removed. We show that this phenomenon can be best modeled if each finger uses an error-based adaptive controller that uses a weighted sum of velocity error information from the two individual fingers. The model suggests the neighboring finger contributes about 28% of the total error drive. We conclude that the finger motor controllers are not fully individuated because errors experienced only by one finger influence adaptation of a neighboring finger.

B. Introduction

Finger individuation is commonly defined as the ability to move one finger independently of the movement or posture of adjacent fingers, and is known to depend in large part on the integrity of the corticospinal tract (Lawrence, DG, Kuypers, 2012). In individuals who have had a stroke, there is a correlation between impaired finger individuation and reduced upper extremity function (Schieber et al., 2009), suggesting the importance of finger individuation for human dexterity. Restoring hand function after stroke is a particularly challenging problem, and targeting improved finger individuation through rehabilitation therapy has shown promise in addressing this problem (Fischer et al., 2007a; Friedman et al., 2014). Further development of this approach would benefit from an improved understanding of how the motor system normally establishes finger individuation.

Finger individuation is mechanically complex because skin, soft tissue and tendons cause mechanical coupling between fingers (Kilbreath and Gandevia, 1994). Therefore, when one finger moves actively, an inherently passive movement occurs in adjacent fingers unless it is actively prevented. Additionally, the muscles that move the fingers, aside from the thumb, are multi-tendoned, and thus cannot exert fully isolated forces on single fingers at a time (Lang and Schieber, 2003).

While mechanical coupling introduces some joint movement of fingers, finger individuation is specifically considered to be the independent active movement of the fingers. Due to the shared role of the actuators responsible for finger individuation, individuated finger movements require synergistic activation of multiple muscles (Lemon et al., 1986; Schieber, 1990). Studies using EMG to investigate the role of synergistic muscle activation in finger

individuation have demonstrated that when one finger is actively lifting a weight, the non-lifting fingers exhibit muscle activity as well (Ingram et al., 2008), suggesting some degree of overlap of the neural activity responsible for the movement of each finger. Isolating where and how this overlap occurs is an ongoing investigation. However, EMG and physiological studies in primates have shown organized control of skilled finger movements at the level of the motor cortex, and have provided evidence for direct cortico-moto-neuronal connections (projections from the motor cortex to the motoneurons of muscles acting on the hand and fingers) being responsible for the ability to perform discrete finger movements (Lang and Schieber, 2004; Muir and Lemon, 1983). Further evidence in both macaques and humans specifies that a combination of activation and inhibition of muscles of individual digits controlled by M1 motor neurons produces finger individuation (Maier et al., 2013; Schieber, 2002). How these areas establish individuated control is unclear.

Experimental methods designed to study finger individuation typically focus on measuring the existing degree of isolation of movement between fingers. For example, many studies of finger individuation in humans use the finger individuation index, which measures the degree of independence of individual fingers based on their ability to move without the movement of other fingers (Schieber, 1991; Susanto et al., 2015; Taheri et al., 2014; Thielbar et al., 2014). Here, we study an alternate aspect of individuated finger control, which is how movement errors experienced by one finger affect a neighboring finger. Specifically, we asked: to what extent does the neural subsystem responsible for maintaining and improving control of a finger in a changing dynamic environment operate independently of the information being gathered and processed by the other finger subsystem? Either the two fingers could be fully

individuated and adapt independently of each other, or the fingers could lack full individuation and be influenced by errors that a neighboring finger experiences.

C. Methods

We recruited 16 healthy right-handed individuals (9 males and 7 females) between ages 22-60 with no known neurological impairments to participate in this study. All subjects provided informed consent according to the UCI IRB requirements.

A) Experimental Protocol

The experiments described here used FINGER (Finger-Individuating Grasp Exercise Robot), a custom robot designed to measure and assist in individuated finger gripping movements (**Figure 3.1**, (Taheri et al., 2014)). FINGER uses stacked, back-drive-able single degree-of-freedom mechanisms that can be adjusted to fit different hand sizes to assist subjects in moving the index or middle finger along a naturalistic curling pattern involving all three joints of the finger similar to that used in a power grasp. FINGER was programmed to apply a velocity-dependent force field to the index and/or middle fingers, with the effect of resisting the curling movement of these fingers.

Subjects placed their right hand (the dominant hand for all subjects) in the FINGER robot, which rested in front of them on a table. To do this, they flexed the elbow to about 90 degrees so that the forearm lay parallel to the torso. The forearm was also supinated 90 degrees so the palm of the hand faced the front of the body.

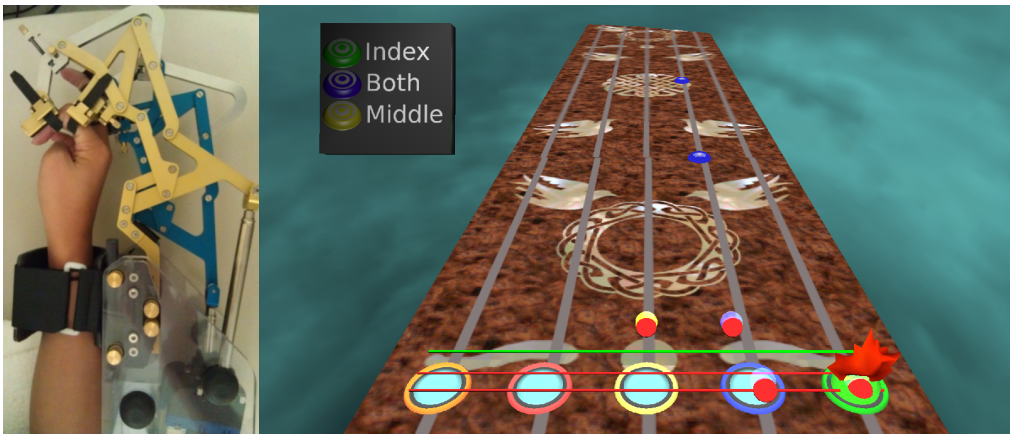

Figure 3.1 Left: The FINGER robot allows users to independently flex the index and middle fingers in a normal grasping-like movement. Right: Participants flexed the index finger or middle finger to move a cursor (red dot) to hit notes progressing toward them down the virtual fret board. The far right target specified index finger movements, the second target from the right specified joint index and middle finger movements, and the third target from the right specified middle finger movements. The other two targets were not used.

The experimental task was based on Guitar Hero, a popular video game that many people find highly engaging and motivating, and which requires precise timing of finger movements. In the custom-designed game used here, subjects attempted to hit notes scrolling down the computer screen to the beat of a popular song (**Figure 3.1**). Two types of notes were possible: notes to be hit by flexion of the index finger, and notes to be hit by flexion of the middle finger. These notes were segregated by color (index notes were green and middle notes were yellow) and by position on the screen (green notes scrolled down the right side of the screen, and yellow notes scrolled down the center of the screen) and a legend was also presented to the subjects describing which finger to use for which type of note. Fingers had to flex a specific distance, from about 90% of full extension to 70% of full flexion, to hit each note at the correct time. Visual feedback of the finger position relative to the note was also given on the screen. A hit note was indicated by the note bursting into flames. After a note was hit, the robot assisted subjects in extending their finger back to the relaxed position.

During a familiarization period, subjects learned how to interact with FINGER and perform the experimental task. The familiarization period consisted of first attempting to hit notes scrolling down the computer screen to the beat of a metronome, then attempting to hit notes to the beat of a short song. Subjects were allowed to repeat the practice period or song until they indicated they were comfortable using the robot (typically after one or two practice trials and songs).

After the training period, subjects sequentially completed three songs. The subjects played the first 20% of the first song (Chicago by Sufjan Stevens) without any perturbation. Then, a viscous, resistive force field was applied to either the index or middle finger (selected randomly), which resisted finger flexion with a force proportional to the speed at which the finger was flexed. We will refer to the finger that experienced the force field as "the perturbed finger". Flexing the perturbed finger through the viscous field felt like moving through a thick syrup. The magnitude of the viscous field was tuned so as to be as strong as possible without causing a subjective sense of fatigue by the end of the song. Prior to the force being applied, subjects alternated through a variety of patterns that allowed for roughly equal notes per finger. Then, immediately before applying the force field, a string of three notes was presented to the perturbed finger, followed by two notes on the perturbed finger immediately after the force turned on, then switched to one note on the non-perturbed finger. We then resumed a sequence of patterns similar to those originally used, except we presented a higher proportion of notes for the perturbed finger. Once 80% of the notes in the song had passed, the force was removed from the perturbed finger without warning and the subjects completed the remainder of the song with no resistive forces, again with roughly equal notes played per finger. The song

had a total of 189 notes, and overall, 112 notes were played by the perturbed finger and 77 notes were played by the non-perturbed finger.

The second song was a shorter "washout" song (Bad Moon Rising by Creedence Clearwater Revival; 48 total notes, 21 on the index finger, 14 on both, and 13 on the middle finger) with no added forces. This song was intended to wash out effects of the force field applied in the previous song. The third song was the same song as the first song, however the note sequence was reversed such that the notes played by the index finger in the first trial were played by the middle finger in the second and vice versa. Additionally, the force was applied to the opposite finger. To remove order effects, half of the subjects received the force on the index finger first, while the other half experienced a force on the middle finger first. Subjects completed the songs in about 13 minutes. Finger fatigue was minimized by allowing a break between the training period and the experimental songs.

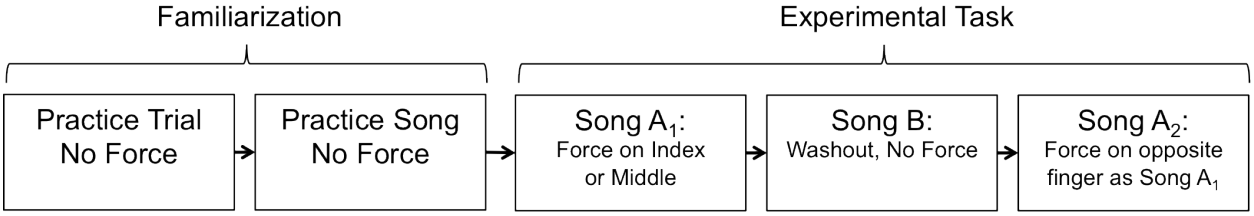

Figure 3.2 The experiment consisted of a familiarization and experimental phase. The length of the familiarization phase varied from subject to subject and depended on the speed at which each subject achieved a basic understanding of the task. The experimental task, consisting of three songs, took approximately 13 minutes. The finger that the force field was applied to in Song A was randomly selected for each subject.

B) Data Analysis and Statistical Methods

Maximum finger flexion velocity was used to quantify the adaption of the finger motor control system to the viscous resistive force field. For each finger for each of the two experimental songs, we calculated direct and after effects as follows. The direct effect of the

force on the perturbed finger was defined as the maximum velocity of the finger for the first note for which the force was applied minus the mean of the maximum velocity of the finger for the last five notes before the force was applied. The after effect of the force on the perturbed finger was defined as the maximum velocity of the finger for the first note after the force was removed minus the mean of the maximum velocity of the finger for the last five notes before the force was applied. Thus, a non-zero aftereffect means that the velocity immediately after the field was removed was different from the velocity before the field was applied. The direct effect and after effect of the non-perturbed finger were defined as the maximum velocity of the non-perturbed finger on the first note that the finger moved following application or removal of the force field to the perturbed finger minus the mean of the maximum velocity of the non-perturbed finger on the last five notes before application or removal of the force field to the perturbed finger.

We used one sample t-tests with α=0.05 to determine if there were non-zero after and direct effects, and paired t-tests to compare size of after and direct effects.

C) Mathematical Model

To better understand how the fingers adapted to the force field, we created a mathematical model to simulate finger movements throughout each song. We assumed the maximum velocity v_i of the i^{th} finger on a note was proportional to the net muscle activation of that finger u_i, with the constant of proportionality *B* determined by the viscous force field strength:

$$v_1[n] = u_1/B, v_2[n] = u_2/B \quad (1)$$

where the subscripts 1 and 2 denote the index and middle fingers respectively. As in previous models describing motor adaptation in response to an applied viscous force field, we assumed

that the motor system updates muscle activation based on the error *e* between an achieved and a desired value (Emken et al., 2007). For our task we defined this value as the error between the achieved maximum velocity and a desired maximum velocity (v_d):

$e_1 = v_1 - vd_1$ and $e_2 = v_2 - vd_2$ (2)

However, unlike previous models, we designed the model to also allow for the possibility that finger control subsystems share information about the errors they experience by defining a shared error vector:

$$eshared = \begin{vmatrix} 1 & 1-a \\ 1-b & 1 \end{vmatrix} \begin{vmatrix} e_1 \\ e_2 \end{vmatrix} \quad (3)$$

Here, the cross-over coefficient *a* determines how the error from finger 2, the middle finger, affects the control of the index finger, and vice versa for the cross-over coefficient *b*. If finger adaptation were fully individuated, *a* and *b* would each equal zero. Again, as in previous models we assume the motor system updates muscle activation based on an error-based learning law with a slacking (also called a forgetting) term as has been shown previously (Emken et al., 2007):

$u_1(n+1) = s_1 * u_1(n) - g_1 * eshared$ and $u_2(n+1) = s_2 * u_2(n) - g_2 * eshared$

where s_i is the slacking coefficient (range from 0 to 1, where s_i=1 indicates no slacking) and g_i is the learning gain.

For the simulations below, we selected initial values for the simulated muscle commands u_1 and u_2 that would ensure that both simulated fingers would initially move at the desired velocities v_{d1} and v_{d2}.

$u_1 = g_1 * vd_1/(1 - s_1 + \frac{g_1}{B})$ and $u_2 = g_2 * vd_2/(1 - s_2 + \frac{g_2}{B})$

We performed a nonlinear optimization in Matlab to solve for the unknown parameters in the model using the collected data for each subject. The unknown parameters were *g1*, *g2*, *s1*, *s2*, *a*, *b*, and *B*. We simulated three simpler versions of the model and one more complex version of the model also, as explained in the Results. The lower bounds for all model parameters were set to 0. For the cross-over coefficients, upper bounds were set to 100. The upper bound for all other variables was set to 1. Optimizations were run multiple times with different starting values for the parameters to verify convergence to an apparent global minimum. The performance of all versions of the model was assessed by calculating root mean squared error (RMSE).

D. Results

In this experiment we studied how the index and middle fingers adapted to a viscous force field applied to one finger at a time, as participants played a musical computer game.

Effects on the Perturbed Finger

The maximum flexion velocity on the perturbed finger dropped significantly when the force field was first applied for both the index ($p = 2.51e-10$) and middle finger ($p = 7.31e-10$), indicating a direct effect of the force field (**Figure 3.3**). When the force field was unexpectedly removed, there was a significant overshoot in velocity relative to the baseline value for the index ($p = 0.0062$) and middle finger ($p = 0.0032$), indicating an aftereffect of adaptation. Thus, both the index and middle fingers adapted when the force field was individually applied to them in a way consistent with formation of a predictive model of the field.

Effects on the Non-Perturbed Finger

We next examined whether the finger that did not experience the applied force (i.e. the non-perturbed finger) was influenced by the short-term adaptation of the perturbed finger to the force field. When the middle finger was the non-perturbed finger, its velocity increased significantly after the force field was applied to the perturbed (index) finger ($p = 3.99e\text{-}4$), and its velocity decreased significantly when the force field was removed from the index finger ($p = 0.0336$), even though the finger was not directly manipulated (**Figure 3.3B**). When the index finger was the non-perturbed finger, its velocity did not change significantly when the force was applied to ($p = 0.0998$) or removed from ($p = 0.2273$) the middle finger, although there was a trend in this direction. Note there was a small movement of the non-perturbed finger during perturbed-finger movement trials, which, was on average, 7% of the distance required to hit a note for the middle finger.

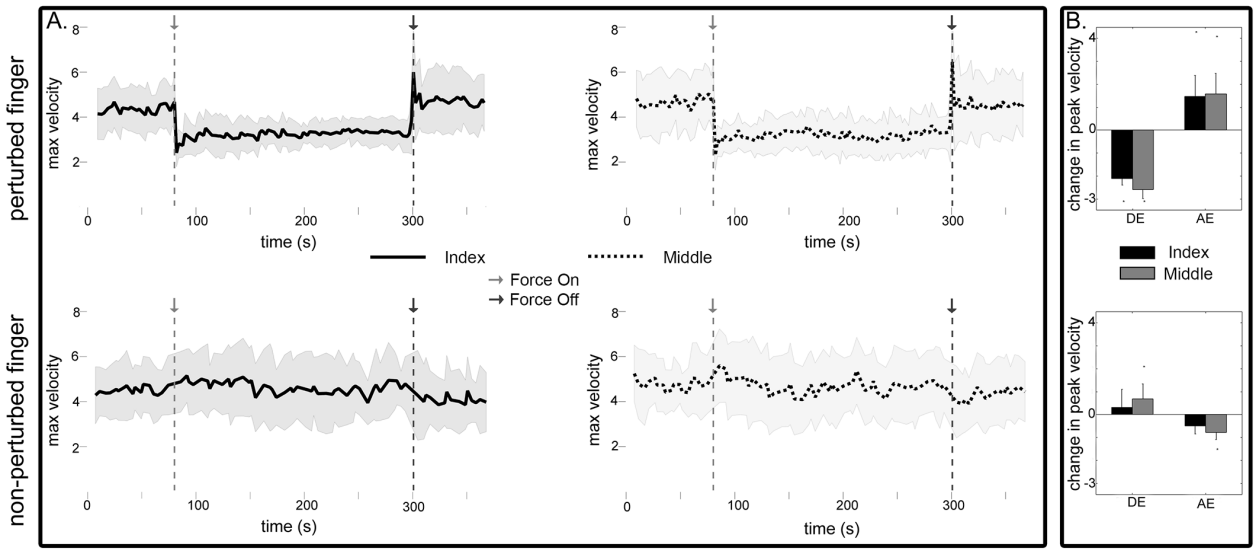

Figure 3.3 Effects of the force field on maximum velocity of the index and middle fingers. A) Maximum finger flexion velocity achieved during each note for index (solid) and middle (dotted) fingers. After the first 20% of notes, a viscous field was suddenly applied to the perturbed finger (time denoted by first vertical dashed line). Both fingers were then allowed to adapt to the

perturbation before it was abruptly removed once 80% of the notes were complete (second, vertical dashed line). B) Direct Effects (DE) and After Effects (AE) of non-perturbed and perturbed fingers (black bars= index finger, gray bars = middle finger). Both fingers experienced significant DEs and AEs when perturbed. Only the middle experienced a significant DE and AE when non-perturbed

Mathematical Model

The model in which the fingers shared errors fit the data fairly well (Figure 4). The values of the cross-over coefficients were: a=0.284±0.332, b=0.278±0.326. Thus, in the model, the update of each finger was affected by the error experienced by both the error experienced by the finger itself, and, with a smaller weighting, the other finger. The values of the gains and slacking factors were also solved for, and were g1 = 0.439±0.282, g2 = 0.491±0.343, s1 = 0.936±0.057, s2 = 0.913±0.092, B = 2.04±0.365.

We ran three simpler versions of the model: one that included no shared errors (removing a and b), one including only the shared error for the index finger (removing b), and one including only the shared error for the middle finger (removing a). Additionally, we ran a more complex version of the model in which each finger had an individualized B term (B_1 and B_2). The three simpler versions had mucher higher RMSEs than the shared error version of the model,while the more complex version had only a slightly lower RMSE (**Table 3.1**).

Table 3.1 Root Mean Square Errors of Model Versions

	Root Mean Square Error (RMSE)	Shared error comparison (t-test)
Shared error	1.2418±0.18	
No shared errors	1.329±0.184	p = 2.78e-5
One shared error (index)	1.337±0.286	p = 0.0376
One shared error (middle)	1.35±0.32	p = 0.0491
B per finger (B_1 and B_2)	1.229±0.181	p = 0.0197

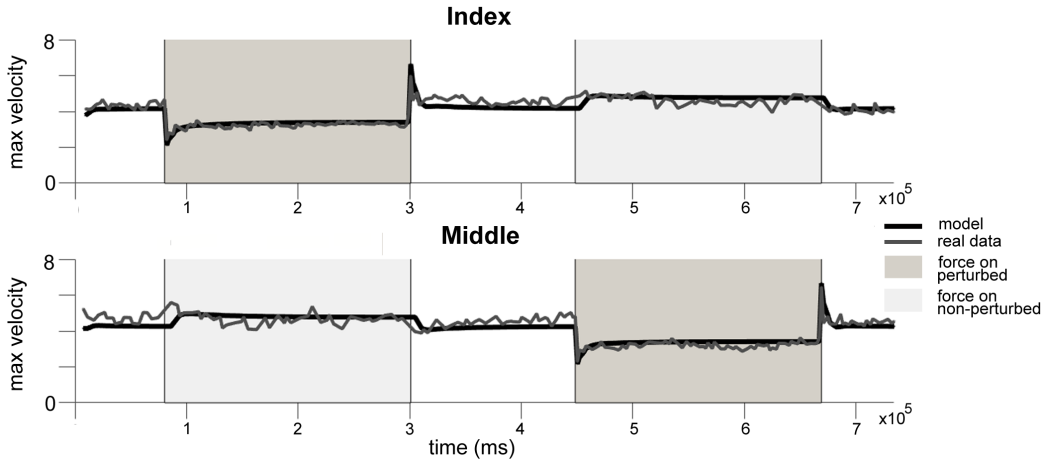

Figure 3.4 Experimentally measured movement (thin gray trace) of the index (top) and middle (bottom) finger, and model's prediction of each finger's movement (thick black trace). The dark gray shaded areas show the perturbed finger when the force field is on, while the light gray shaded areas shown the non-perturbed finger when the force is applied to the perturbed finger. When the field was on the index or middle finger, the model's prediction of that finger's movement showed a direct effect (decrease in velocity immediately when the force is applied at trial 22) and an after effect (increase in velocity immediately when the force was removed at trial 90). The non-perturbed finger was predicted to slightly increase in velocity when the force field was applied (trial 18), and to decrease in velocity when it was removed (trial 62).

E. Discussion

Finger individuation traditionally describes the extent to which the motor system can move one finger without moving the other fingers. In this study, we studied another aspect of finger individuation: whether motor adaptation of one finger influences its neighboring finger. One could imagine that the finger motor control system could have evolved, or could have established during development, finger-specific controllers that are completely independent of each other, responding only to the errors associated with the movement of the finger they control. Alternately, the fingers could lack full individuation and be influenced by the errors

that the neighboring finger experiences. The results of the present experiment and model support the second option.

Possible Limitations

Could the known mechanical coupling between the fingers have biased this result? It is conceivable that the small, unintentional movements caused by mechanical coupling between the perturbed and non-perturbed fingers might have provided the non-perturbed finger an opportunity to learn about its environment. However, if anything, these small movements would have informed the non-perturbed finger controller that it remained in an unperturbed environment. This conflicting information presumably would have worked to have reduced the error sharing.

Another issue in interpreting the results is that we found significant direct and after effects for the non-perturbed finger only when the index finger was the perturbed finger. In contrast, the model fit suggested comparable amounts of error-sharing between the fingers. This difference might be explained by relatively large variability and lack of statistical power in the experimental results when the middle finger was perturbed, whereas the model fit makes use of constraints in mathematical structure to eliminate variability.

Implications and Future Directions

The motor system achieves the ability to move one finger independently of another not by assigning individual actuators to each finger, but by calculating the multiple muscle activation map that succeeds in moving one finger while keeping the other still. In the case of error sensing, our results suggest that the error distribution map is calculated in a way to share errors, rather than isolate them. Such error sharing has been noted for other limbs. For the

arms, the transfer of adaptation between arms can occur after short-term training, stabilizing after long-term training (Joiner et al., 2013; Malfait and Ostry, 2004). Notably, this transfer is biased, as skills learned using the dominant hand often transfer to the non-dominant hand whereas skills learned on the non-dominant hand rarely transfer to the dominant hand (Criscimagna-Hemminger et al., 2003), suggesting that the motor system develops an asymmetry in the way it shares motor information between the hands based on the statistics of how each hand is used in daily life. Studies in gripping and multi-digit force production have also shown within-hand transfer of learning, which is hypothesized to occur at the planning stage and be refined through somatosensory feedback (Santello et al., 2013). In one such study, subjects were asked to minimize object roll when lifting a loaded device with a specific type of grip (Fu et al., 2011). Results demonstrated that even when the subjects were asked to change their grip by adding or removing fingers, subjects were able to learn the amount of torque required and adjust individual digit forces accordingly based off of finger position (Fu et al., 2011). The functional benefit of this type of error sharing is that humans are able to maintain consistent manipulation performance despite variability in position (Shibata et al., 2014). Taken together, these studies suggest that the way in which the motor system modifies control of limbs is based on how the fingers, arms, and hands are typically used. It remains to be known whether inter-limb transfer results from two separate internal models formed by a common error from the trained to the untrained hemisphere (Joiner et al., 2013). Similarly, recent studies have investigated how within-hand synergies are shared, but an exact model of how the motor system might control complex hand and finger movements is not known (Santello et al., 2013).

Could the lack of finger individuation we found during adaptation then have functional advantages? Finger individuation is typically viewed as a crowning achievement achieved late in evolution, which is lost when the neocortex is damaged (Kamper and Rymer, 2001; Lang and Schieber, 2003; Lemon et al., 1986; Schieber et al., 2009). However, in normal hand use, we speculate, if one finger experiences a changed dynamic environment, then the neighboring finger will also. For example, if one finger is fatigued, then the other fingers will likely be also, since fingers usually get fatigued during multiple-finger grasping. It seems rare to use one finger in an isolated way in a novel dynamic environment that the other fingers don't experience. If the fingers normally experience similar dynamic environments, then sharing errors will give a "head start" to neighboring fingers during adaptation, which is perhaps a small functional advantage. In the present experiment, the adaptation of the non-perturbed finger was non-functional, but this was likely due only to the artificiality of the experimental set paradigm.

Future work in this area should involve studying the coupling of fingers during motor adaptation in individuals with stroke. Finger individuation depends on cortico-spinal tract integrity, and thus middle cerebral artery stroke impairs the motor control of finger individuation (Kamper and Rymer, 2001; Lang and Schieber, 2003; Lawrence, DG, Kuypers, 2012). Because of the resulting deficits to fine motor skills, several robotic therapeutic techniques targeting restoration of finger individuated movements after stroke are currently being explored (Fischer et al., 2007b; Hwang et al., 2012; Susanto et al., 2015; Taheri et al., 2014; Thielbar et al., 2014). However, damage to brain areas that implement internal model formation might result in a reduction in the capacity to adapt predictive forces of a finger, and

consequently, either reliance on phylogenetically more primitive descending systems that have a hard-wired non-individuated control, or an alteration in the way errors sensed by multiple fingers are combined to control individual fingers. Both possibilities could limit the re-learning of finger individuation. Identifying alterations to finger individuated motor learning might provide a more complete picture of motor system function in stroke, and provide targets for therapies directed at restoring fine motor movements.

CHAPTER 4

Maintenance of Hand Motor Recovery Following Action Observation Treatment for Stroke

A. Abstract

Background: Current approaches to stroke rehabilitation can be extremely effective at conferring functional gains. Yet at the same time, these gains are commonly lost once therapy has ended. This situation leads to the imperative of developing methods that foster the maintenance of functional gains over the long term. We propose that shifting emphasis away from behavioral compensation and toward direct intervention in neural pathways could lead to major advances in maintenance of therapeutic gains. The present study focuses on remediation of neural pathways, testing the hypothesis that Action Observation Treatment (AOT) for stroke improves function and preserves functional gains for at least six months following therapy.

Methods: Structural and motor-task functional MRI scans were obtained in 22 healthy individuals, and 21 individuals with chronic stroke prior to, immediately following, and six months to one year after a one month course of either AOT or a control therapy (neurodevelopmental therapy; NDT). Objective and subjective measures of hand motor function were also obtained at all three time points in both treatment groups.

Results: AOT resulted in gains in motor function, both immediately after therapy and six months to one year later. No significant gains were seen following NDT at either time point. Furthermore, individuals receiving AOT performed significantly better than those receiving NDT on the Nine Hole Peg Test at maintenance. Importantly, maintenance of gains with AOT was related to stability of resting functional connectivity and accompanied by brain activation

patterns similar to those of healthy individuals. Participants in the NDT group showed neither of these imaging findings.

Conclusions: This study suggests that AOT, but not a standard physical therapy approach, remediates neural pathways critical for motor function after stroke, and that these gains are maintained over the long term.

B. Introduction

Stroke remains a major source of disability in the United States, with approximately 6.5 million individuals living with long-term impairments (Go et al., 2014). Following initial hospitalization and stabilization, stroke survivors usually undergo rehabilitative physical therapy with an emphasis on recovery of activities of daily living (ADLs)[a]. Neurodevelopmental therapy (NDT), for example, is a widely used treatment in the Western world, and has been shown to be as effective as other therapies (Huseyinsinoglu et al., 2012). Although functional gains are often seen initially, it is all too common for the stroke survivor to stagnate or even regress following the completion of such therapy (Paolucci et al., 2001). Maintenance of gains following rehabilitative therapy is a crucial but often an unsuccessful component of stroke care. It is therefore imperative to develop rehabilitative therapies that maximize functional gains, returning the individual to self-sufficiency as quickly as possible, while at the same time maintaining these gains over the long term.

[a] Abbreviations: ADL = Activities of Daily Living, NDT = Neurodevelopmental Therapy, CIMT = Constraint Induced Motor Therapy, AOT = Action Observation Treatment, MMSE = Mini Mental Status Exam, NHPT = Nine Hole Peg Test, WMFT = Wolf Motor Function Test, MAL-AOU = Motor Action Log Amount of Use, SIS = Stroke Impact Scale, Virtual Brain Transplantation, ROI = Region Of Interest, M1 = primary motor cortex, S1 = somatosensory cortex, MFG = Middle Frontal Gyrus, PMd = Premotor cortex (dorsal), PMv = Premotor cortex (ventral), SMA = Supplementary (and pre-supplementary) Motor Areas, sPAR = Superior Parietal Lobule (and intra-parietal sulcus), iPAR = Inferior Parietal Lobule, CMA = Cingulate Motor Area, THAL = thalamus, CRB = cerebellum, rsFC = Resting State Functional Connectivity, FA = Fractional Anisotropy

It is understandable that improved function may occur during the course of therapy, only to be lost upon completion. Physical therapy for upper extremity weakness generally focuses on training an individual to compensate for weakness by shifting functionality to remaining motor effectors, typically through some degree of trunk rotation/displacement, scapular elevation, shoulder abduction, and/or internal rotation (Levin et al., 2009). While this may expedite improvement in ADLs, it has limitations for long-term maintenance. The required motor adaptations confer a risk of developing new, less natural motor patterns that may lead to decreased range of motion, pain, and learned disuse (Levin et al., 2009). Furthermore, following such therapy, stroke survivors often have limited access to further therapy, partly due to the high cost of providers (Demaerschalk et al., 2010) and of specialized therapeutic equipment (Godwin et al., 2011).

Most contemporary physical therapy does not address the underlying neurophysiologic changes occurring in the brain following stroke, and thus has only indirect and unfocused effects on development of sustainable neuronal substrates. One effort aimed at remediation is constraint induced motor therapy (CIMT). In CIMT, the unaffected arm is intermittently restrained to encourage greater use of the affected arm, leading to improvement in function following stroke. However, these gains appear to be compensatory in nature (Kitago et al., 2013a) and arm restraint is often perceived as unpleasant for the stroke survivor (Page et al., 2002), thus complicating the potential for long term gains. Indeed, accumulating evidence suggests that CIMT is not superior to standard therapy in providing long term functional gains (Corbetta et al., 2010; Dahl et al., 2008). Electrical stimulation therapies aim to improve motor function by influencing neuronal activity directly (Grefkes and Fink, 2012). Although some

benefits appear to outlast the stimulation period (Hummel et al., 2005), the degree to which they are maintained is unclear (Edwardson et al., 2013). Cellular based strategies (e.g., stem cells) offer the potential for true neuronal remediation (Cramer and Riley, 2008), but these require further testing before their immediate and long term efficacy will be known. Given the extensive study of emerging therapies such as these, it is striking that their effect on long term maintenance has not received much attention.

Action observation treatment (AOT) is an emerging therapeutic technique that has the potential to address many of these shortcomings (Buccino, 2014; Small et al., 2013b). At a neuronal network level, AOT aims to the extent possible, to stimulate the brain network involved in observation and imitation of motor actions, and by doing so, to re-establish motor functioning comparable to the pre-stroke state via the repair or reorganization of neural circuitry. The rationale for this approach comes from neurophysiological data from macaque (di Pellegrino et al., 1992), in which neurons in the posterior parietal lobe and inferior premotor cortex cooperate to process perceived motor actions. This “mirror neuron system” is increasingly understood to play a role in action observation and imitation in humans(Ferri et al., 2015; Molenberghs et al., 2012). We believe that using AOT to harness this motor circuit for stroke rehabilitation represents a promising remediative approach, and has particular promise for both immediate therapeutic benefits and maintenance of these gains over the long term. Indeed, previous studies have supported the effectiveness of AOT in functional recovery following stroke (Celnik et al., 2008; Ertelt et al., 2007; Franceschini et al., 2012). In the current paper, we seek to expand upon these findings, comparing AOT to a widely used rehabilitative

treatment; furthermore, we include multiple neuroimaging techniques in order to gain insight into the mechanism underlying functional gains associated with AOT.

Objective:

We hypothesize training motor observation and imitation in ecological patient-specific tasks via AOT will facilitate normalization of brain activity required to perform motor tasks following ischemic stroke. We further expect a direct effect of this approach on the long term, with an extended maintenance phase following therapy.

C. Materials and methods

Twenty-one volunteers with chronic stroke were recruited for this study. Individuals were screened using the mini-mental state exam (MMSE) (Folstein et al., 1975), the short version of the Token Test (De Renzi and Faglioni, 1978), the Edinburgh handedness inventory (Oldfield, 1971) and Hamilton depression inventory (HAMILTON, 1960). Inclusion and Exclusion criteria are listed in **Table 4.1** and patient demographics are in **Table 4.2**. All participants provided informed consent prior to inclusion in the study, and all procedures were approved by the Institutional Review Boards of The University of Chicago and the University of California, Irvine.

Table 4.1 Inclusion/exclusion criteria

Inclusion	Exclusion
• ≥18 years old • Single stroke by clinical history • Lesion in the MCA distribution • Stroke onset ≥6 months earlier • Moderate to severe hand impairment (50≥Fugl-Meyer Score≥20) • Normal state of consciousness • Normal corrected visual and auditory acuity • Language comprehension (short Token test ≥26) • Upper extremity protective responses	• History of significant central neurological illness other than stroke • History of significant arm injury with functional residual • History of spinal cord injury • Cognitive impairment (MMSE<23) • Untreated depression (CESD≥16) • Visual neglect • Significant carotid stenosis • Metallic implants • Pregnancy • Severe spasticity in affected arm (≥3 on the Ashworth Scale)

Table 4.2 Subject characteristics

Subject	Age	Gender	Hemisphere	Handedness	Affected Hand	Location of stroke	Volume of stroke (mm3)
1	53	F	Left	Right	D	Cort/subcort	21650.8
2	59	F	Left	Right	D	Subcort	11029.3
3	54	F	Left	Right	D	Subcort	8713.1
4	63	F	Right	Right	ND	Subcort	10964.6
5	41	F	Right	Right	ND	Cort	22495.0
6	54	F	Left	Right	D	Cort/subcort	49078.0
7	57	M	Left	Right	D	Cort/subcort	17411.0
8	57	M	Left	Right	D	Cort/subcort	38703.0
9	54	F	Left	Right	D	Subcort	27677.0
10	50	M	Right	Right	ND	Subcort	3570.0
11	68	M	Left	Right	D	Subcort	1988.3
12	56	F	Left	Right	D	Subcort	6239.7
13	46	M	Left	Right	D	Subcort	325.0
14	56	F	Right	Left	D	Cort/subcort	60669.0
15	72	F	Left	Right	D	Cort	39295.3
16	37	M	Left	Right	D	Cort/subcort	83406.2
17	62	M	Left	Right	D	Subcort	22154.8
18	61	M	Left	Right	D	Subcort	978.0

19	74	M	Left	Right	D	Cort/subcort	63642.0
20	67	F	Right	Right	ND	Subcort	588.0
21	74	F	Left	Right	D	Cort/subcort	44892.0

D = dominant, ND = non-dominant, Cort = cortical, Subcort = subcortical

Randomization. Participants were randomized to treatment groups using blocked randomization, stratified primarily by baseline severity of hand motor dysfunction, and secondarily by age and education. The first half of participants was randomly assigned to AOT or NDT. Subsequent participants were assigned to one or the other group based on a match in severity of weakness (determined by time on the nine hole peg test; NHPT), and then by age and education.

Healthy Controls: Twenty-two healthy controls were included for the imaging portion of this study.

Therapeutic Interventions

Both treatment groups received 1-1.5 hours of therapy per day for four weeks (weekdays). Individuals with weakness in the dominant hand performed unimanual motor tasks, whereas those with weakness in the non-dominant hand performed bimanual tasks.

Action Observation Treatment. AOT was performed as previously described (Ertelt et al., 2007). First, a specific, goal-oriented ecological action was presented on a television screen for three minutes, and the patient was instructed to observe the action with the intention of imitating it. The actions involved fine-skilled manipulation of everyday objects. The patient subsequently executed the observed movements for three minutes. Subsequent videos showed similar actions with additional motor elements present (e.g., first reaching to grab a telephone, then reaching to grab it *and* holding it next to the ear). Following the completion of several such incremental stages of motor imitation, the entire sequence was repeated from the beginning.

By showing increasingly complex actions, imitation difficulty progressively increased throughout the month of therapy.

Control (NDT) Intervention. Individuals assigned to the control therapy received standard NDT administered by a licensed Physical Therapist who was both an APTA certified Neurological Clinical Specialist and certified in NDT (KC). As with AOT, NDT involved performance of skilled motor tasks and gradual incremental training. These sessions incorporated tasks commonly used in NDT (40-50 minutes) as well as tasks used in the AOT treatment arm (20-30 minutes). NDT was provided to each participant based on individual arm ability, and therapy progressed as needed. In the NDT therapy, the therapist demonstrated each task to the participant, who then practiced it for 3 minutes. Unlike in the AOT arm, which incorporated no verbal feedback, patients in the NDT arm received verbal feedback on the quality of whole arm and hand movements, and strategies to compensate for errors. In NDT, the focus of therapy was on the quality of movements rather than the goal. Similarities and differences between AOT and NDT are listed in **Table 4.3**.

Table 4.3 Similarities and differences between AOT and NDT

	Action Observation Therapy	**Neurodevelopmental Therapy**
Similarity	Goal Oriented Movements Incremental Intense training Uni/Bimanual	Goal Oriented Movements Incremental Intense training Uni/Bimanual
Difference	No feedback Visual Whole Movements Re-establishing movements Fine-skilled hand movements Old network remodeled	Feedback Verbal Fractionated Movements Re-learning movements Gross arm-hand movement New network recruited

Outcome measures

Performance measures were collected at three time points: (1) pre-treatment, (2) post-treatment, and (3) six months to one year post-treatment. The primary outcome measure was the difference in score on the Functional Ability Scale of the Wolf Motor Function Test (WMFT) (WOLF et al., 1989), developed specifically to assess motor function of the upper limb after stroke. Secondary measures included brain network physiology assessed by functional MRI (fMRI) and additional behavioral measures, including the Nine hole peg test (Mathiowetz et al., 1985), Luria Pre-Motor Tests (Teichner et al., 1999), the Fugl-Meyer upper arm test (Fugl-Meyer et al., 1975), the Motor Activity Log (MAL-AOU) (Uswatte et al., 2005), the NIH stroke scale (Brott et al., 1989), and the Stroke Impact Scale (SIS) (Duncan et al., 1999). Assessments were performed by a licensed physical therapist blinded to treatment group.

Imaging

Image Acquisition

We collected high-resolution T1-weighted MPRAGE scans (3T Philips, SENSE head coil) with FOV= 250 x 250, resolution = 1 x 1 x 0.6 mm, SENSE reduction factor = 1.5, TR/TE = 7.4/3.4 ms, and whole brain BOLD fMRI images using gradient echo single-shot echo-planar imaging (EPI), with FOV = 230 x 230 mm, Flip angle 70 degrees, TR = 2 sec, TE = 20 ms. In a functional MRI task, subjects performed a bimanual self-paced sequential finger tapping task, on which they were trained prior to scanning. In the scanner, cues were provided using Presentation® software (www.neurobs.com), using a block design with 10 seconds of movement (start = beeping sound; stop = voice saying “stop”) followed by 10 seconds of rest over 5:20 minutes. A

resting functional MRI scan was also collected using the same scanner parameters as the task fMRI; for this acquisition, participants are instructed to relax, but avoid falling asleep.

Functional Image Pre-processing

Data processing and analysis were performed blind to treatment group. Resting fMRI preprocessing was performed using the FMRIB Software Library (FSL; http://www.fmrib.ox.ac.uk) as follows: (1) Removal of the first five scans; (2) slice timing correction; (3) motion correction; (4) brain extraction; (5) registration to the anatomical volume; (6) removal of voxel-wise temporal mean; and (7) removal of nuisance variables including six motion parameters, global white matter and CSF signals, and temporal band pass filtering at 0.01-0.1 Hz (2^{nd} order butterworth).

Functional MRI data were processed using AFNI (Cox, 1996) as follows: (1) Removal of the first five scans; (2) Motion correction using a 6 parameter 3D registration of functional and anatomical data; (3) 3D spatial registration of functional images to the middle scan of the first run; (4) Registration of functional images to the anatomical volume; (5) Despiking of time series; (6) Mean normalization of the time series; and (7) Inspection and censoring of time points occurring during excessive motion (>1 mm).

Structural Analysis

To permit the use of standardized brain anatomical atlases despite the presence of large brain lesions, we used our virtual brain transplantation (VBT) approach. VBT transplants the anatomical data from the non-lesioned hemisphere to the lesioned hemisphere, makes a number of corrections for ipsilesional volume loss and contralesional shifting, and provides

anatomical landmarks for standard alignment and inflation algorithms developed for healthy individuals (Dick et al., 2013; Solodkin et al., 2010).

We then used the FreeSurfer software (Dale et al., 1999) to parcellate the brain (2005 Destrieux atlas). Using SUMA (Saad and Reynolds, 2004), we imported the 2D surface representations back into the 3D volume in AFNI. Multi-subject analysis was performed using an anatomical region-of-interest (ROI) approach. ROIs included the following: M1 (primary motor cortex), S1 (somatosensory cortices), MFG (middle frontal gyrus), PMd (premotor cortex, dorsal), PMv (premotor cortex, ventral), SMA (supplementary and pre-supplementary motor areas), sPAR (superior parietal lobule and intra-parietal sulcus), iPAR (inferior parietal lobule), CMA (cingulate), THAL (thalamus) and CRB (cerebellum). SMA, PMd, CRB and THAL not included in FreeSurfer were added by hand as we have done previously (Walsh et al., 2008).

Functional imaging measures

a) Functional connectivity at rest: Network stability

Stability of resting functional connectivity was determined using a sliding window approach, in which the resting fMRI time series were first divided into windows with a length of 28 seconds and an overlap (i.e., lag) of 2 seconds across windows. For each window of time series, pairwise Pearson correlation coefficients between each pair of brain regions were then determined. These correlation coefficients were then cross-correlated with themselves to find normalized autocorrelation coefficients. These values were averaged across all lags to produce the temporal stability of each pairwise functional connection. In order to compare between groups and test for relationships with measures of motor function, the mean and standard

deviation of the temporal stability measures for all regions was determined for each subject (Shen et al., 2015a, 2015b).

b) Evoked fMRI: Bimanual movements

Analysis of individual subject data was performed using multiple linear regression, comparing the signal time course per voxel to a reference waveform. Voxels were considered active when the single voxel p-value was less than 1×10^{-5}. A Monte-Carlo simulation was performed to determine that enforcing a three-dimensional contiguity requirement (three contiguous voxels or 53 mm^3) allowed us to achieve a corrected family-wise significance of $p < 0.05$. Volumes of activation within ROIs constructed as described above were then determined by calculating the number of active voxels per region and were normalized for region volume by dividing them by the total number of voxels per region.

Statistics

Measures were compared between the two stroke groups at all time points using a Wilcoxon rank sum test. Pre-therapy behavioral measures were compared between the two stroke groups using a Mann-Whitney test. Behavioral measures obtained post-therapy and at maintenance were compared to pre-therapy measures using a Wilcoxon signed-rank test. Comparisons between resting state fMRI stability measures and changes in motor function measures from baseline to immediately post-therapy and at the maintenance stage were done using linear regression.

D. Results

Demographics

The AOT group (N = 11, age 55.4 ± 7.4, 9 female) and the NDT group (N = 10, age 60.6 ± 11.9, 4 female) did not differ in any age or other demographic factor (see **Table 4.2**), but did differ in gender (AOT 81% female versus NDT 40% female).

Motor function outcome measures

In order to perform statistical analysis on the most salient data, a dimension reduction on clinical outcome measures was performed using Multiple Correlation coefficients. Indeed, this showed that all motor outcomes were statistically (>85%) represented by the Fugl-Meyer, Wolf motor test, 9-hole peg and MAL-AOU test. A summary of the significant findings is presented in **Table 4.4**.

1) Pre-therapy: The two groups were well matched in functional ability prior to therapy, as no significant differences were found between the AOT and NDT groups for any primary and secondary measures (all $p > 0.05$).
2) AOT group: When examining the within-group change in function as a result of therapy (e.g., pre-therapy to post-therapy), individuals receiving AOT had a robust treatment response, showing a significant level of improvement in the WMFT ($p = 0.003$), the MAL-AOU ($p = 0.001$), the FM ($p = 0.016$), and the NHPT ($p = 0.02$). At the maintenance phase, improvements persisted for the WMFT ($p = 0.003$), as well as the nine-hole peg test ($p = 0.004$), MAL-AOU ($p = 0.005$), and the FM ($p = 0.011$).
3) NDT group: Individuals receiving NDT showed significant differences from pre-therapy to post-therapy FM ($p = 0.02$) and WMFT ($p = 0.01$), and from pre-therapy to

maintenance FM (p = 0.02), WMFT (p = 0.03), and the MAL-AOU (p = 0.02). However, it is important to note that none of these measures would be significant if a correction for multiple comparisons is imposed (Bonferroni correction of p = 0.00625), which is not the case for much of the AOT findings.

4) AOT compared to NDT: When comparing individuals receiving AOT to those receiving NDT therapy immediately following therapy, there were no significant differences between groups. At the maintenance stage, however, individuals receiving AOT performed significantly better on the nine-hole peg test compared to those in the NDT group (p < 0.009).

Table 4.4 Motor Function Measures

	Pre-therapy	**Post-therapy**	**Maintenance**	**Change from Baseline to Post-therapy**		**Change from Baseline to Maintenance**	
	AOT vs NDT			*AOT*	*NDT*	*AOT*	*NDT*
Fugl Meyer	0.91	1.000	0.39	0.016	0.02	0.011	0.02
WMFT	0.32	0.075	1.000	**0.003**	0.01	**0.003**	0.03
NHPT	0.61	0.383	**0.009**	0.02	0.18	**0.004**	0.41
MAL AOU				**0.001**	0.06	**0.005**	0.02

Brain imaging

Relation between stability of functional connectivity and behavioral measures

To examine the relation between network stability and response to rehabilitative treatment after stroke, we tested for correlations between pre-therapy rsFC stability and motor function immediately following treatment and at the maintenance stage. There was no significant relationship between mean or standard deviation of rsFC autocorrelation values and

motor function immediately post-therapy, both for individuals receiving AOT and those receiving NDT.

However, at the maintenance stage, several significant relationships were found. For those receiving NDT, the standard deviation of pre-therapy rsFC autocorrelations was positively correlated with WMFT FA ($p < 0.03$). For those receiving AOT, pre-therapy correlations were found between stability measures and motor function: (i) mean autocorrelation values negatively correlated with WMFT (time) ($p < 0.03$) and positively correlated with WMFT FA ($p < 0.03$); and (ii) the standard deviation of autocorrelation values was positively correlated with Fugl-Meyer ($p < 0.02$) and WMFT FA [changes] ($p < 0.02$), and negatively correlated with WMFT (time) ($p < 0.01$).

Notably, there was no significant difference of stability of functional connectivity between individuals receiving AOT and those receiving NDT; this was true prior to therapy (mean: AOT = 0.1155 ± 0.0088 (mean ± standard error), NDT = 0.1299 ± 0.0098; standard deviation: AOT = 0.1182 ± 0.0047, NDT = 0.1291 ± 0.0053), immediately post-therapy (mean: AOT = 0.1366 ± 0.0083, NDT = 0.1307 ± 0.0088; standard deviation: AOT = 0.1299 ± 0.0042, NDT = 0.1293 ± 0.0044), and at maintenance (mean: AOT =0.1132 ± 0.0079; NDT = 0.1192 ± 0.0085; standard deviation: AOT = 0.1185 ± 0.0078, NDT = 0.1217 ± 0.0051). Furthermore, there were no significant differences in stability metrics with respect to change from baseline, both for change at post-therapy (mean: AOT = 0.0191 ± 0.009 (mean ± standard error), NDT = 0.0007 ± 0.01; standard deviation: AOT = 0.0109 ± 0.005, NDT = 0.0002 ± 0.005) and at maintenance (mean: AOT = 0.001 ± 0.009, NDT = -0.008 ± 0.095; standard deviation: AOT = 0.0018 ± 0.005, NDT = -0.004 ± 0.006).

Task-related functional imaging measures associated with therapy

Healthy Controls

Functional activation during the self-paced bimanual task showed consistent bilateral activation of many regions. The largest volumes of activation were found in M1, S1 and PMv, though consistent group activation was also seen in PMd, sPAR, iPAR, CRB and THAL.

Stroke Patients

Pre-therapy

Prior to therapy, individuals with stroke had larger volumes of activation in almost all regions assessed compared to healthy controls (**Figure 4.1**). This increased activation was greatest in SMA (left 230%, right 153%), thalamus (left 45%, right 72%), and CRB (left 60%, right 97%). In contrast, some regions showed decreased activation, including left MFG (left -26%), PMd (left -19%), M1 (left -11%), and S1 (left -40%). Little to no change was seen in right MFG, left PMv, right S1, and bilateral iPAR regions.

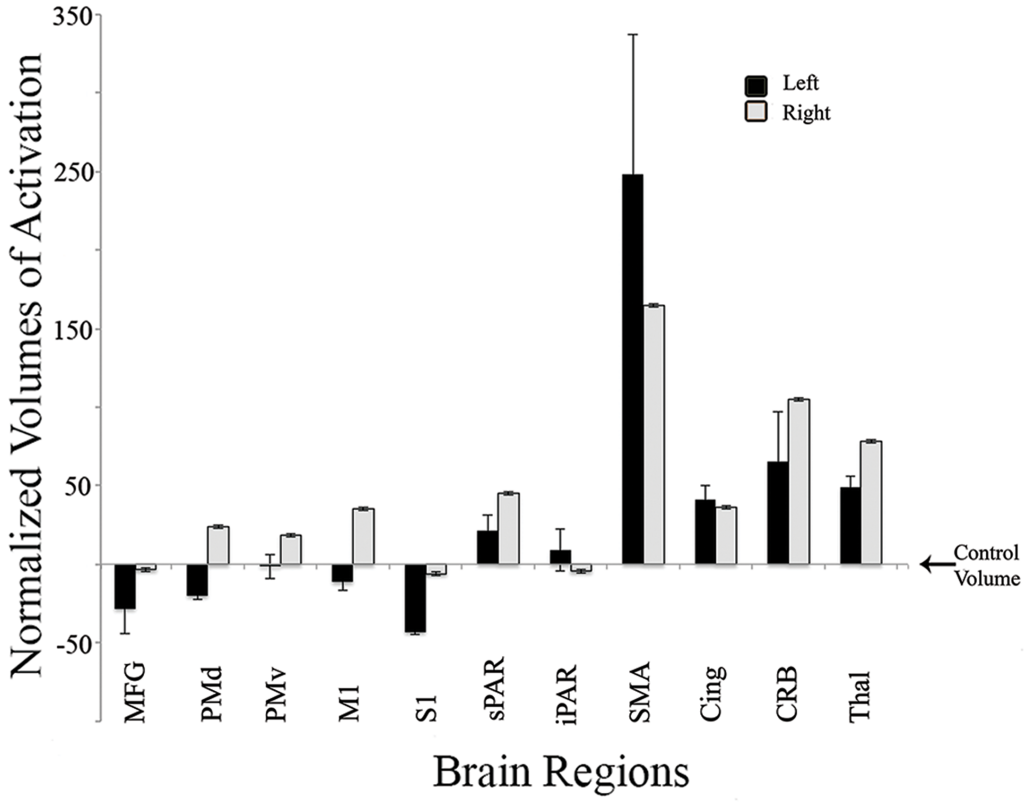

Figure 4.1 Volumes of activation (normalized for region size, ± standard error) in individuals with stroke, prior to therapy, with respect to healthy controls (i.e., positive values indicate volumes greater than controls, negative values indicate values smaller than controls). Black bars represent the left hemisphere and gray bars the right. Larger volumes of activation in stroke were most prominent in non-primary motor areas (SMA, thalamus, and cerebellum), whereas little differences or slight decreases were noted in primary motor and sensory areas.

Post-therapy

AOT: Following AOT, volumes of activation decreased in most regions compared to pre-therapy. This decrease was fairly uniform across regions assessed, both ipsilesional (range 76-93%) and contralesional (74-96%) (**Figure 4.2**).

NDT: Following NDT, volumes of activation also decreased throughout the regions assessed compared to pre-therapy levels. However, these changes were not as consistent as in AOT, with a greater variability in both ipsilesional (26-95%) and contralesional hemispheres (36-91%). This

was predominantly driven by smaller decreases in activation in PMv, PMd, thalamus, SMA, and CMA bilaterally, as well as ipsilesional M1 and contralesional S1.

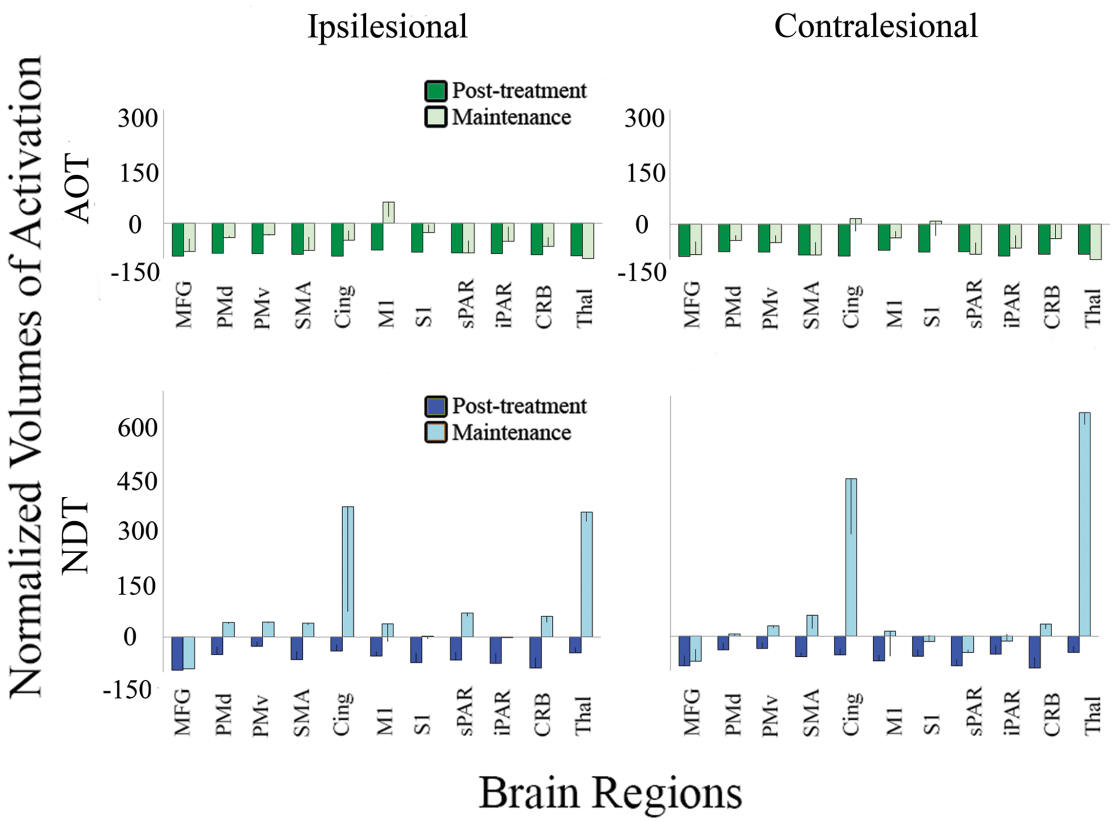

Figure 4.2 Normalized volumes of activation (± standard error) following AOT and NDT, as compared to pre-therapy levels. Immediately following both AOT and NDT (Post-Treatment), widespread decreases in activation volumes were seen in all motor regions assessed (dark blue and dark green bars). At six months to one year follow-up (Maintenance), volumes of activation in almost all regions remain reduced in the AOT group (light green), whereas the majority of regions showed increased activation following NDT (light blue bars). Of note, ipsilesional M1 showed increased activation at maintenance following AOT, but not following NDT. Conversely, NDT showed increased activation in bilateral cingulate and thalamus, whereas these increases were not seen following AOT.

Maintenance

AOT: At the maintenance phase, individuals who received AOT continued to show reduced activation in most regions including PMd, PMv, ipsilesional cingulate, S1, ipsilesional CRB, and

contralesional M1. Notable exceptions included an increase in volume of activation in ipsilesional M1 and contralesional CMA and S1. (**Figure 4.2**).

NDT: Compared to the AOT group, individuals receiving NDT had increased activation or returned to pre-therapy activation levels at maintenance. Particularly large increases were seen in bilateral cingulate and thalamus. Exceptions included ipsilesional MFG and contralesional superior parietal regions, where the volumes of activation remained reduced.

AOT vs. NDT: At maintenance, individuals who received AOT had volumes of activation that were more similar to controls, as compared to NDT. This parallel between AOT and healthy controls was seen in several regions in both hemispheres. Group differences are presented in **Table 4.5**. Individuals who received AOT tended to be more similar to controls than those receiving NDT in contralesional M1, as well as bilateral SMA, cingulate, sPAR, CRB, and thalamus. Conversely, individuals who received NDT were more similar to controls than those who received AOT in ipsilesional MFG and M1, and contralesional MFG. Of note, both groups showed some levels of increased activation in ipsilesional M1 and contralesional CMA.

Table 4.5 Volumes of activation for AOT and NDT at maintenance, relative to controls

	AOT	**NDT**	**AOT**	**NDT**
	Ipsilesional (% difference from controls)		Contralesional (% difference from controls)	
Supplementary Motor Area	30	129	-48	108
Cingulate	8	943	73	1000
Superior Parietal Lobule	-17	214	-18	85
Cerebellum	0.5	122	38	95
Thalamus	-100	378	-100	430
Middle Frontal Gyrus	180	6	180	139
Primary Motor Cortex	272	46	64	131
Premotor Cortex, dorsal	187	195	160	149
Premotor Cortex, ventral	26	25	11	22
Somatosensory cortex	-12	-11	73	9
Inferior Parietal Lobule	77	73	28	58

Summary: When comparing group activations (indicating regions in which subjects had common areas of activation), some general patterns were found. Specifically, individuals receiving AOT demonstrated a sustained decline in overall number of regions of activation through to the maintenance phase, whereas individuals receiving NDT showed an initial decline in regions of activation from pre-therapy to post-therapy, followed by a subsequent increase at the maintenance stage.

E. Discussion

Two main points summarize the results of the present study: 1) AOT confers functional gains in chronic stroke, both immediately following therapy and over the long term, and 2) baseline (post-stroke) stability of functional connectivity correlates with response to AOT but not NDT, and concomitant with the functional gains, brain activation patterns are similar to healthy controls following AOT but not after NDT.

AOT confers functional gains in chronic stroke that are maintained over the long term

This study expands upon our preliminary findings (Ertelt et al., 2007), using a larger cohort and a robust control group, to provide further evidence that AOT is efficacious in improving motor function following stroke. It is also complemented by studies showing observation/practice techniques leading to improvements in motor learning in healthy individuals (Shea et al., 2000), adult stroke (Celnik et al., 2008), Parkinson's disease (Buccino et al., 2011) and children with cerebral palsy (Buccino et al., 2012). AOT is also associated with increased force generated and increased excitability of the motor cortex (Porro et al., 2007), suggesting that AOT leads to a higher level of brain activity than motor imagery or physical training (Gatti et al., 2013).

AOT was developed following discovery of the mirror neuron system, as a novel biologically-based method that combines observation of object-manipulation with subsequent imitation of the same goal-oriented action. Although the mechanistic underpinnings are still unclear, one hypothesis implicates the neurophysiological response to experience mediated by motor imitation, i.e. repetitive actions triggered by visual input leading to alterations in neuronal activity (Small et al., 2012, 2013b). Activities of daily living are well-rehearsed motor activities; almost by definition, people are "experts" at completing these tasks (Milton et al., 2007). Therefore, it has been suggested that the brain maintains very specific representations of these activities (Milton et al., 2007). The goal of AOT therefore is to activate the mirror neuron networks associated with these ADLs, thus priming them for increased contribution to subsequent motor activity.

Most exciting is the current finding of maintenance of AOT-induced gains over the long term. It is all too common for gains made in a standard acute rehabilitation program to be lost in the long term. Indeed, Paolucci and colleagues found nearly 40% of patients experience a decline in mobility status at the 1-year follow-up (Paolucci et al., 2001). In addition, long-term gains can vary greatly between individuals. These results indicate that AOT may be particularly effective in facilitating long-term maintenance of gains, even within a heterogeneous population.

Specifically, this study found that individuals receiving AOT showed significantly better scores on the nine-hole peg test (NHPT) at the maintenance stage than those who received NDT. This is particularly interesting, as the NHPT is a measure of fine manual dexterity (Oxford Grice et al., 2003), which is a major component of the movements AOT aims to impact. Indeed, AOT is specifically designed to target skilled hand movements, as it emphasizes manipulation of common objects with finger and wrist movements. In contrast, other measures included in this study, such as the Fugl-Meyer and WMFT, include hand dexterity as one of several measures of upper extremity function, including shoulder, elbow, forearm, and wrist (Wolf et al., 2001). These measures thus put greater reliance on proximal/gross motor movements, decreasing the likeliness that differences will be seen between the two treatment groups. It is also important to note that the NHPT is a valid, reliable measure of upper extremity function following stroke (Croarkin et al., 2004), and has a high degree of correlation with other measures of hand function (Beebe and Lang, 2009). Furthermore, the NHPT was one of the main components isolated via dimension reduction in this study. It is important that the difference in NHPT scores

was seen at the maintenance phase, thus supporting our hypothesis that AOT is particularly effective at preventing regression of gains in the long-term.

Another notable finding of the current study is that, although AOT conferred greater motor benefit than NDT on several measures, only the maintenance-phase NHPT was found to be significantly greater in individuals receiving AOT than those receiving NDT. One of the complicating issues in stroke research is the large variance of functional ability commonly seen in study populations (Rehme et al., 2012), and this was also true in the current study (FM range: 3 – 52, WMFT range: 2.47 – 62.13 sec, WMFT FA range: 16 – 74). Such variance makes it particularly difficult to find significant differences, unless the study is restricted to include only a narrow range of baseline functions. Therefore, while our decision not to stratify subjects by functional ability serves as a more representative sample for a wide range of stroke outcomes, this high variance may explain the lack of significant differences between the two groups on many of the reported measures.

There are several reasons why AOT may be more effective at maintaining functional gains over the long term (see Small et al, 2013 for a review (Small et al., 2013b)). In particular, it has the potential to remediate the neural substrate required for functional recovery. Although recovery is often compensatory in nature, true remediation has been shown to be possible in animal models (Moon et al., 2009). Although the exact mechanism is still unknown, AOT may, through the recruitment of mirror neurons, facilitate the restoration of neural circuitry used for everyday movements. This theory is based on the process of indirect remediation (Lee and van Donkelaar, 1995), in which the mirror neuron circuitry is facilitated via observation of activations (as evidenced by lower motor evoked potential thresholds), thus providing an

increased role in subsequent motor output. In addition, although AOT and NDT are alike in that they both involve gradual and incremental training using identical, skilled, uni- or bimanual tasks, AOT focuses on a specific goal (e.g., pick up the orange) without trainer intervention regarding the movements, whereas NDT emphasizes the movements used (e.g., flex the wrist to pick things up) as guided by the trainer. In this context, it is easy to see how AOT could serve to facilitate remediation of neural networks that underlie these movements, and how NDT might rely on the development of compensatory strategies to accomplish the motor tasks.

After AOT, brain activity resembles patterns more consistent with healthy controls.

Resting state functional connectivity (rsFC) provides insight into the temporal relationship between brain regions, and thus the organization of neural networks of an individual (Fox and Raichle, 2007). Previous studies have provided evidence that rsFC relates to underlying neural activity and structural connectivity (Honey et al., 2009). To date, rsFC has been predominantly quantified using an average measure over the course of a scan, but such connectivity is increasingly understood to vary over time (Hutchison et al., 2013). One way to characterize such dynamic rsFC is by the stability of interactions between regions over time. For example, Shen and colleagues (Shen et al., 2015b), using metrics similar to those employed in the current study, found that homotopic functional connectivity, facilitated by direct anatomical connections, was more stable over time when compared to other types of connections. The current study found that, for individuals receiving AOT, baseline/pre-therapy rsFC stability was significantly related to degree of motor recovery. Specifically, individuals with a greater amount of overall stability between and among brain regions prior to therapy showed greater functional improvement following AOT (but not NDT). Given that those receiving AOT

also experienced greater functional improvement than those receiving NDT, it is reasonable to speculate that this stability is, at least in part, an important mechanism underlying AOT.

In this study, the positive correlation between mean stability and motor measures suggests that regions that most consistently work together are doing so more effectively in individuals with the largest improvement following AOT. Critically, no such relationship was found for those receiving NDT, suggesting that NDT receives less benefit from stable interactions among brain regions. We further examined the standard deviation of stability to gain insight into the variance throughout the system. Individuals with a greater variance of temporal rsFC stability showed greater response to AOT, but not to NDT. This greater variance may indicate that AOT takes greater advantage of a larger range of functional connectivity in the post-stroke state than NDT.

These findings thus provide empiric evidence for the mechanism of functional gains following AOT. Given that there was no significant change in stability measures following either therapy, AOT does not appear to rely on new patterns of functional connectivity to produce improved motor outcomes, but rather facilitates the re-emergence of previously developed neural architectures to produce functional gains. Interestingly, this is in accordance with the intended purpose of AOT; as described above, AOT is specifically designed to generate activity of mirror neurons with the intent of regenerating functional interactions that were lost to stroke, essentially reprising stroke-affected network connectivity. Conventional/standard rehabilitative therapies, such as NDT, aim to develop new, compensatory strategies, thus requiring the emergence of new functional connectivity. In sum, this differential response to functional stability may be, at least in part, due the ability of AOT to capitalize more efficiently

on the existing neural architecture. This notion is supported by the fact that the strength of functional connectivity depends to some degree on the qualities of the white matter pathways between regions (Hermundstad et al., 2013), which are distinctly impacted by stroke and are notoriously difficult to remediate.

This notion is further supported by the findings of task-dependent fMRI. Following AOT, the patterns of brain activation during a hand motor task become more similar to healthy controls after therapy and this change carries through to the maintenance phase. Individuals who received standard NDT developed activation patterns similar to controls over the course of the therapy, but they subsequently reverted to pre-therapy patterns at the maintenance stage. A notable exception is bilateral MFG and ipsilesional M1, with values remaining similar to controls at maintenance following NDT, whereas increases were seen following AOT. In the current parcellation, the hand-drawn PMd partially overlaps with the FreeSurfer parcellated MFG, where MFG includes the most anterior region of PMd. With this in mind, we show that PMd is robustly activated after AOT but not after NDT. This parallels previous studies showing that MFG and M1 are active during action observation (Buccino et al., 2004; Hari et al., 2014), that may represent recruitment of elements associated with the mirror neuron system. Taken together, these results may indicate the mechanism by which AOT is more effective at maintaining post-stroke reorganization over the long term. Of particular interest is the increased activation of the cerebellum seen following AOT (both post-treatment and at maintenance) but not following NDT; such increased activation has been previously shown to relate to levels of functional recovery up to six months following stroke (Small et al., 2002).

Caution is key to the interpretation of functional MRI data, as changes in BOLD signal are not directly translatable to function. However, brain patterns after stroke can relate to levels of function in motor deficits (Zemke et al., 2003), spatial neglect (Corbetta et al., 2005), and aphasia (Warburton et al., 1999). Functional recovery is correlated with the degree of recovery of neurophysiological activity in the affected primary cortical areas (Cramer, 2008). Interestingly, this also mirrors previous findings in expertise, wherein increasing skill in a movement is associated with reduced brain activation (Milton et al., 2007).

Limitations

Certain study limitations must be considered when interpreting these results. First, as the sample size is modest, these results should be considered preliminary, and warrant further investigation. Also, although AOT confers improvement in functional gains in the given cohort, it is not yet clear as to why some individuals benefit from AOT more than others. Furthermore, our method of assigning participants to treatment groups based on baseline function, age, and education led to the situation that the AOT group had a greater proportion of woman than the NDT group; however, as women tend to have poorer recovery of the upper limb than men following stroke (Coupar et al., 2012), this imbalance may in fact serve to blunt the measured benefits of AOT.

Additionally, we excluded individuals with depression to remove this as a potential confound, but it remains to be seen how depression will impact gains from AOT. Finally, as described in the results, individuals receiving NDT did show some degree of functional improvement, although this was not significant after correction for multiple comparisons. NDT

is widely used as current standard of care, and the results of the current study do not question the validity of this therapy; rather, these findings support the robustness of AOT.

CHAPTER 5

Functional Mechanisms of Recovery after Chronic Stroke: Modeling with The Virtual Brain

A. Abstract

We have seen important strides in our understanding of mechanisms underlying stroke recovery, yet effective translational links between basic and applied sciences, as well as from big data to individualized therapies, are needed to truly develop a cure for stroke. We present such an approach using The Virtual Brain (TVB), a neuroinformatics platform that employs empirical neuroimaging data to create dynamic models of an individual's human brain; specifically, we simulate fMRI signals by modeling several parameters associated with brain dynamics after stroke.

In twenty individuals with stroke and 11 controls we obtained rest fMRI, T1w, and DTI data. Motor performance was assessed pre-therapy, post-therapy, and 6-12 months post-therapy. Based on *individual* structural connectomes derived from DTI, the following steps were performed in the TVB platform: 1) Optimization of local (mesoscopic) and global parameters (conduction velocity and global coupling), 2) Simulation of BOLD signal using the optimized parameter values, 3) Validation of simulated time series by comparing frequency, amplitude, and phase of the simulated signal with the empirical time series, and 4) Multivariate linear regression of the model parameters with clinical phenotype.

Compared to controls, individuals with stroke demonstrated a consistent reduction in conduction velocity, increased local dynamics, and reduced local inhibitory coupling. A negative

relationship between local excitation and motor recovery, and a positive correlation between local dynamics and motor recovery were seen.

TVB reveals a disrupted post-stroke system favoring excitation-over-inhibition and local-over-global dynamics, consistent with existing mammal literature on stroke mechanisms. Thus, our results point to the potential of TVB to determine individualized biomarkers of stroke recovery.

B. Introduction

Previous research has provided key insights into the disease process in stroke. Studies in mammals have uncovered basic mechanisms of ischemic injury, inflammatory responses, and cellular recovery (Carmichael, 2012; Nudo, 2013). In humans, researchers have suggested predictive imaging biomarkers for disease progression and recovery, mapped associated changes in brain networks, and developed new rehabilitative therapies (Reiss et al., 2012). Despite this, stroke remains a major source of disability in the United States, with approximately 6.5 million people living with stroke, with some level of hemiparesis present in approximately 50% (Go et al., 2014). This is neither the fault of mammal nor human studies, as both are constrained by their respective study populations. Studies in mammals are well-controlled yet homogeneous, limiting their translational abilities. Human studies reflect the population at hand, yet often rely on indirect measures, obscuring the full picture. Although both share a common goal of curing stroke via the repair and reorganization of the injured brain, what is missing is a translational bridge to effectively span the divide between basic mechanisms and dynamic human brain systems.

At the same time, the neuroscience community is immersed in collecting large datasets to provide greater understanding of brain function and dysfunction. Such initiatives span normal function

(Human Connectome Project), development (NIH Pediatric Database), and brain disorders such as Alzheimer's disease (ADNI) and mental illness (Research Domain Criteria Project). While these initiatives provide the necessary empirical foundation, quantitative tools are missing to integrate these multiple datasets to "reconstruct" the brain, and provide the link between these data and those from a single person.

Over the last 6 years, a neuroinformatics platform has been developed: The Virtual Brain (TVB) (Sanz Leon et al., 2013). The defining feature of TVB is that it generates *personalized* functional neuroimaging data based on individual structural connectome data to create personalized virtual brains. These models are specific to each individual person, and contain the connectivity between parts of the brain and the dynamics of local neural populations. TVB uses structural MRI data to create the custom brain surface, diffusion-weighted MRI data to infer the anatomical connections between brain areas, and then functional MRI data as the target to modify the parameters of the model to reproduce the observed functional data. The neuroinformatics architecture of TVB houses a library of models, which catalogues the biophysical parameters that produce different empirical brain states (Ritter et al., 2013b). Global biophysical parameters represent biological mechanisms governing dynamics between brain regions, while the local biophysical parameters describe the properties of small populations of neurons integrating dynamics at the local mesoscopic level. That is, modeling in TVB comprises multiple scales of brain dynamics that are invisible to brain imaging devices and therefore TVB acts as a "computational microscope," allowing the inference of internal states and processes of the system.

TVB thus offers a novel platform to formulate biologically interpretable hypotheses on the effects of stroke and its recovery based on biophysical mechanisms governing brain dynamics. Beyond the direct clinical implications of network dysfunction in stroke, these insights can contribute a first

step to the understanding of fundamental mechanisms of the brain's structure-function relationship. TVB has been established and applied to normative data sets (Deco et al., 2012) and for learning and plasticity (Roy et al., 2014) yet a proof of concept needs to be established based on pathological states.

The objective of the present study using the TVB platform was to determine changes in local and global biophysical parameters to better understand individualized brain dynamics after stroke. In this approach, the model parameters act as a means to assess brain health, analogous to blood samples assessing physical health, and hence, parameter changes could ideally be used as potential biomarkers of stroke and/or stroke recovery. So far, such biomarkers have mostly focused on stable architectures, from behavior to fine anatomical and functional levels (Burke and Cramer, 2013). In contrast, our aim is to create a synergistic amalgamation of mathematical models with neuroimaging, where the biomarker derives from the dynamical model itself.

C. Methods

Subjects:

Twenty volunteers with chronic stroke (ages 23-74, 8 females) in the middle cerebral artery (MCA) territory and 11 age-matched controls were included in the study. Human subjects were recruited at a location that will be identified if the article is published. Demographic details and stroke characteristics of our cohort can be found in **Table 5.1**.

Motor performance was assessed with: the Functional Ability Scale of the Wolf Motor Function Test (WMFT), Nine-hole peg test, the Fugl-Meyer upper arm test, and the Motor Activity Log (MAL-14). These assessments were collected at baseline (pre-therapy), after one month of intensive hand therapy (post-therapy) and 6-12 months after therapy (maintenance).

Table 5.1 Demographics and stroke characteristics of the stroke cohort

Subject	Age	Sex	Handedness	Affected Hemisphere	Affected Hand	Stroke Location	Stroke Volume (mm^3)
1	41	F	Right	Right	ND	Cort	22495.0
2	54	F	Right	Left	D	Cort/subcort	49078.0
3	57	M	Right	Left	D	Cort/subcort	17411.0
4	57	M	Right	Left	D	Cort/subcort	38703.0
5	54	F	Right	Left	D	Subcort	27677.0
6	50	M	Right	Right	ND	Subcort	3570.0
7	23	M	Right	Left	D	Subcort	560.0
8	55	F	Right	Right	ND	Cort	6781.0
9	68	M	Right	Left	D	Subcort	1988.3
10	56	F	Right	Left	D	Subcort	6239.7
11	46	M	Right	Left	D	Subcort	325.0
12	56	F	Left	Right	D	Cort/subcort	60669.0
13	37	M	Right	Left	D	Cort/subcort	83406.2
14	62	M	Right	Left	D	Subcort	22154.8
15	57	M	Right	Right	ND	Cort/subcort	25392.0
16	66	M	Right	Left	ND	Cort/subcort	19927.0
17	61	M	Right	Left	D	Subcort	978.0
18	74	M	Right	Left	D	Cort/subcort	63642.0
19	67	F	Right	Right	ND	Subcort	588.0
20	74	F	Right	Left	D	Cort/subcort	44892.0

D = dominant hemisphere; ND = non-dominant, Cort = cortical; subcort = subcortical.

Brain Imaging:

Imaging data were acquired on a 3 Tesla Philips Achieva scanner using the following sequences:

1. High-resolution anatomical images were acquired with a 3D Magnetization Prepared Rapid Gradient Echo (MP-RAGE) sequence: FOV= 250x250, resolution=1x1x1mm, SENSE reduction factor =1.5, TR/TE=7.4/3.4ms, flip angle=8, sagittal orientation, number of slices=301 covering the whole brain.
2. Diffusion Tensor Imaging was acquired with the following sequence: FOV=224x224, TR/TE=13030/55, 72 slices, slice thickness= 2mm, resolution=0.875x0.875x2, 2 mm post-processing iso-voxel with b=1000 sec/mm^2 (and b=0), 32 diffusion directions.
3. Functional imaging acquisition at rest covering the whole brain (37 slices) was acquired using single-shot echo-planar MR (EPI) with slice thickness = 4.0 mm, FOV= 230x230, voxel size = 2.8mm x 2.8mm, TR/TE= 2000/20 ms, duration= 5 min.

Virtual Brain Transplantation:

Because of mechanical deformation consequent to large cortical strokes, the anatomical parcellation on T1w images using semi-automated methods is very difficult to achieve. Hence, a "virtual brain transplant" process was performed in accordance with a previous approach (Solodkin et al., 2010). This method replaces the cortical lesion with the homologous image from the contralesional hemisphere from the same subject. With this, brain parcellation is possible using semi-automatized software. The process consisted of the following steps:

1. Lesion segmentation by hand.
2. Using the AFNI 3dcalc function (Cox, 1996), the homologous region in the non-lesioned hemisphere was dissected and transplanted into the stroke region, effectively filling in the missing portions of the brain.

3. Manual corrections were then done in the interface between the native and transplanted T1-w images by visually examining each voxel and making voxel intensities uniform using AFNI's 3dLocalStat and 3dcalc commands.
4. The brain was then parcellated into 96 cortical and subcortical regions. The original parcellation based on a macaque template (Van Essen, 2004) was transformed to the human MNI template via PALS (Van Essen, 2005). To increase accuracy, the deformation process was carried out using landmarks (based on CARET) and functional activation patterns considered homologous between the two species (Van Essen and Dierker, 2007).

Diffusion Tensor Imaging:

Pre-processing of DTI data consisted of 1) motion correction using the FSL eddy current correction (Leemans and Jones, 2009), 2) generation of a binary brain mask from the b0 image and application of the mask to all diffusion images using the Brain Extraction Tool from FSL (Smith, 2002), 3) fitting of a diffusion tensor at each voxel using FSL's dtifit function, 4) non-linear co-registration of T1 data to the MNI brain and co-registration of T1 images to their respective DTI images producing an MNI to DTI transformation using ANTS (Avants et al., 2011), 5) white and gray matter segmentation performed on the MNI-to-T1 atlas using FAST (Zhang et al., 2001) and 6) parcellation of the gray matter into 96 regions and registration of these regions to the DTI using the T1-to-DTI transformation with a nearest neighbor interpolation.

Tractography and Structural Connectivity Matrix Generation

1. Probabilistic tractography was performed to trace the fiber bundles associated with pairs of cortical regions in the MNI space, which were defined as edges in the network (Ritter et al., 2013b; Zalesky and Fornito, 2009).

2. Two connectivity measures were extracted: a) capacities, depicting the maximum rate of transmission of information through edges, were calculated using the number of streamlines at the minimum cross-sectional area of an edge (Zalesky and Fornito, 2009); and b) distances, defined by the lengths of each edge, were calculated by averaging the lengths of all streamlines in an edge. These measures were used to generate two 96x96 structural connectivity matrices. Quality assurance to reduce false positives was performed on each structural connectivity matrix by a trained neuroanatomist (AS).

Resting State fMRI Pre-processing

Pre-processing was done in AFNI (Cox, 1996) and included the following steps: motion correction of functional and anatomical data sets (Cox and Jesmanowicz, 1999), 3D spatial registration to a reference acquisition from the rsfMRI run, registration of functional images to the T1-w volume, despiking and mean normalization of the time series, motion correction (>1mm, (Johnstone et al., 2006)) and regression of cerebrospinal fluid and white matter signals to remove slow-wave components (e.g. physiological noise) (Lund et al., 2006).

Resting State fMRI Post-processing

Average time series were extracted for each of 96 MNI regions. For each subject, a 96x96 functional connectivity matrix was generated by calculating the pair-wise correlation of the time series for each region (Ritter et al., 2013b) using the "corr" function in Matlab.

*Modeling in TVB (**Figure 5.1**):*

The Virtual Brain (TVB version 1.08) was used for all simulations (Sanz Leon et al., 2013) where the principal empirical input to the platform is the structural connectivity matrix derived from each individual subject's tractography. Based on this input, TVB simulates field potentials by integrating

global dynamics with a local (mesoscopic) model that determines the dynamics *within* brain regions. Following, BOLD signals are derived from the generated field potentials. In this work, we used the Stefanescu-Jirsa 3D (SJ3D, **Figure 5.2**) local model, as the resulting mean field model does not rely heavily on synaptic delays (Jirsa and Stefanescu, 2011; Sanz-Leon et al., 2015a; Stefanescu and Jirsa, 2008), making it compatible with the poor time resolution associated with BOLD signals. Specifically, the SJ3D model is derived from populations of bursting neurons and includes six states describing excitatory and inhibitory dynamics via the inclusion of a variety of biophysical parameters defining the local mean fields (for a list of the parameter values used in the present study see **Table 5.2**) (Hindmarsh and Rose, 1984; Stefanescu and Jirsa, 2008).

The following sequential steps were performed for each individual subject:

1) Importing of a subject-specific connectivity matrix into the TVB platform.

2) Selection of the SJ3D local model.

3) Parameter Space Estimation (exploration and fitting): We sequentially performed systematic parameter space explorations and fitting to determine the optimal values for global and local parameters in all subjects. a) Parameter space exploration: We used heat maps of global variance (mean variance of time series across all brain regions) to constrain the range of values for each model parameter (**Figure 5.3**). The range of values considered is assessed based on those values with high global variance flanked by bifurcation points (Breakspear and Jirsa, 2007). An additional advantage of this approach is that it is not only pragmatic but it can also provide information on the degree of variability and sensitivity that parameter values have onto the simulated signals. b) Parameter fitting: The final optimal value is subsequently obtained by assessing the specific value for the parameters that resulted in the best fit between the empirical and simulated signals based on three metrics described

below. The global parameters explored included conduction velocity and global coupling and the local parameters included K_{12} (excitatory on inhibitory coupling), K_{21} (inhibitory on excitatory coupling), and K_{11} (excitatory on excitatory coupling). The local parameters were chosen as they have the strongest impact on the dynamics of the SJ3D model (Stefanescu and Jirsa, 2008).

4) Stochastic Network simulation: Based on the values obtained in the parameter space exploration, we generated field potentials with the same duration (4 min) and sampling rate (TR=2s) as the empirical rsfMRI acquisition. The length of the simulated data was kept equal to the length of the empirical data in order to minimize the influence of variability over the course of the time series, as it is becoming increasingly patent that values of functional connectivity are not stable over time (Hutchison et al., 2013). White noise with Gaussian amplitude (mean = 0, standard deviation = 1) was added to each node. Numerical integration of the system was performed using stochastic Heun's method (Mannella 2002), with an integration step size of 0.0122 ms.

5) The BOLD signals were derived from the field potentials using a haemodynamic response function implemented with a gamma kernel (Boynton et al., 1996; Sanz-Leon et al., 2015a).

6) Assessing reliability of the simulated time series: Comparison between the empirical and simulated BOLD time series was done in terms of amplitude, frequency, and phase.

Amplitude: We calculated the range of amplitude by identifying the highest and lowest peaks present in the time series across all regions.

Frequency: Fast Fourier transforms of the raw and simulated time series were obtained using Matlab's "fft" function with an fs of 0.5 hz, to determine the range, profile, and peak frequencies (Ritter et al., 2013b).

Phase: This was assessed by comparing the functional connectivity matrices of the simulated

and empirical time series. We averaged all matrices from healthy controls to obtain a group control matrix, and calculated the pairwise linear correlation coefficient between the simulated functional connectivity matrix for each individual to the group.

5) Differences in parameter values between healthy controls and stroke cases were evaluated with Wilcoxon sum rank test corrected for multiple comparisons (Bonferroni).

6) Relationship with clinical phenotype

In order to determine if there was any relationship between TVB parameters and the clinical phenotype, a multiple linear regression was performed between TVB parameters (dependent variables) and the following independent variables: Motor outcome measures (Fugl-Meyer, WMFT, 9-hole peg and MAL-14), patient demographics (age, sex, presence of depression) and lesion characteristics (size, location, time after stroke, side of stroke).

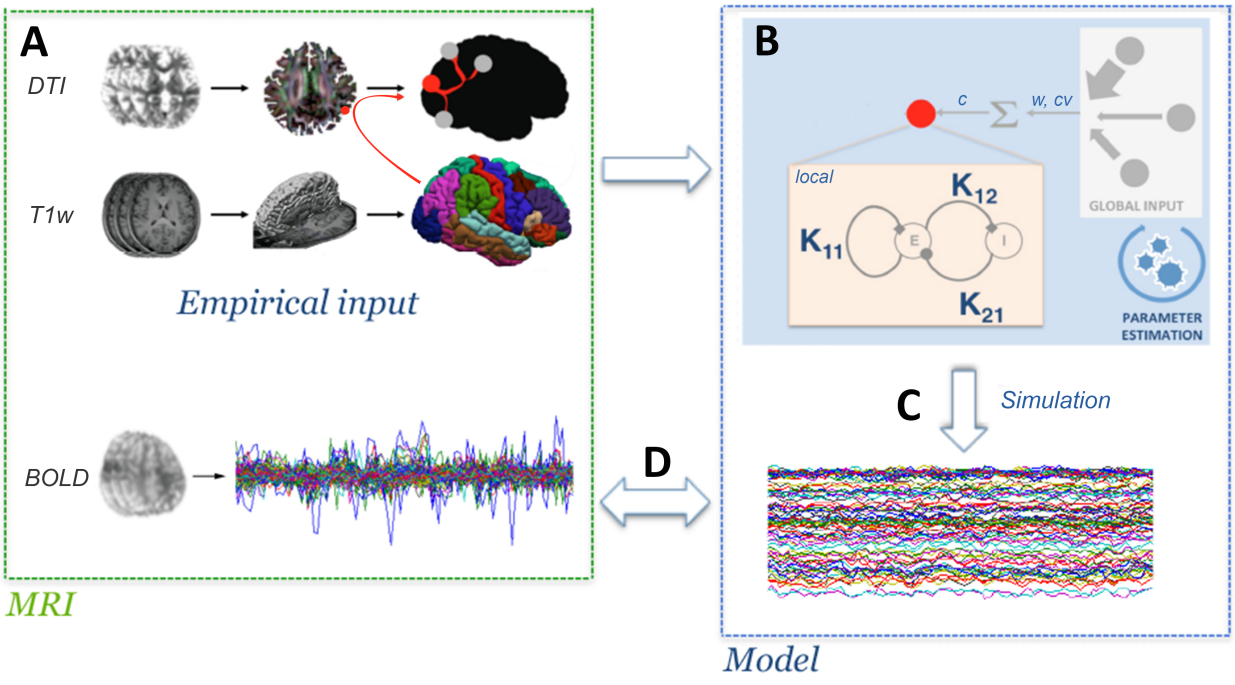

Figure 5.1 Simulation workflow in TVB.

Graphic representation depicting the sequential steps of TVB modeling. (**A**) Empirical inputs (structural connectome) are generated from DTI tractography based on T1-w brain parcellation. (**B**)

Subsequent parameter exploration at the global and local levels. (**C**) Once parameter values are obtained, the BOLD signal is simulated. (**D**) The efficacy of the simulation is calculated by correlating it to the empirical signals.

A

Mean Field Potential Time Delay Noise

$$\dot{x}_i(t) = f\big(x_i(t)\big) + c\sum_{j=1}^{N} w_{ij}x_j\big(t - \Delta t_{ij}\big) + \eta(t)$$

Stefanescu-Jirsa 3D Long-Range Structural Connectivity

B

$$\dot{\xi}_i = \eta_i - a_i\xi_i^3 + b_i\xi_i^2 - \tau_i + K_{11}\left[\sum_{k=1}^{3} A_{ik}\xi_k - \xi_i\right] - K_{12}\left[\sum_{k=1}^{3} B_{ik}\alpha_k - \xi_i\right] + IE_i$$

$$\dot{\eta}_i = c_i - d_i\xi_i^2 - \eta_i$$

$$\dot{\tau}_i = rs\xi_i - r\tau_i - m_i$$

$$\dot{\alpha}_i = \beta_i - e_i\alpha_i^3 + f_i\alpha_i^2 - \gamma_i + K_{21}\left[\sum_{k=1}^{3} C_{ik}\xi_k - \alpha_i\right] + II_i$$

$$\dot{\beta}_i = h_i - p_i\alpha_i^2 - \beta_i$$

$$\dot{\gamma}_i = rs\alpha_i - r\gamma_i - n_i$$

Figure 5.2 Equations of the Stefanescu-Jirsa 3D model.

(A) Evolution equation implemented in The Virtual Brain to simulate brain activity. The mean field potential $x_i(t)$ of a region i at time t is dependent on the local dynamics $f(x_i(t))$ provided by the Stefanescu-Jirsa-3D model, the long-range structural connectivity w, which links regions i and j and is provided by the input of individual structural connectivity matrices (weights), and noise $\eta(t)$). Time delays (Δt) are distance dependent and are provided by the structural connectivity matrices (lengths). All mathematical details of the model and its numerical implementation are provided in (Sanz-Leon et al. (2015, in press)). **(B)** Equations comprising Stefanescu-Jirsa 3D. The first 3 (ξ, η, τ) equations represent the excitatory sub-population of neurons within a local region, while the last 3 equations (α, β, γ) represent the inhibitory sub-population of neurons in that region. IE and II denote the input current to the excitatory and inhibitory populations of each node, respectively. The first of each of the two sets of equations accounts for neuron potentials. The second and third equations account for the

transport of ions across the membrane through ion channels. Note that the dynamics of these populations are dependent on the interactions between inhibitory and excitatory influences (K_{12}, K_{21}, K_{11}).

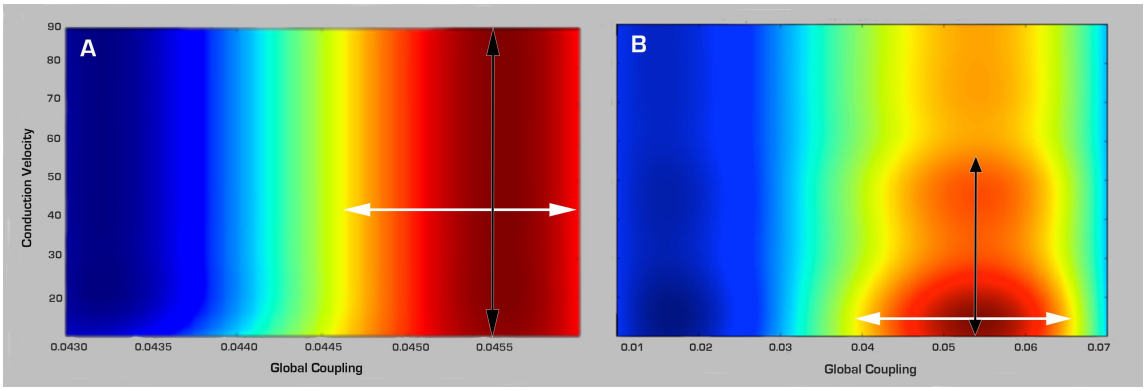

Figure 5.3 Examples of global parameter space exploration in healthy controls and stroke. Two examples of heat graphs of global variance (mean variance of the time series across all regions) used to narrow down the range of parameter values more suitable for modeling in (**A**) a healthy control and (**B)** a stroke case. Global coupling is shown on the x-axis and conduction velocity (m/s) on the y-axis. Colors indicate degree of global variance with hotter colors indicating higher values. White arrows show the range of values considered for global coupling limited by bifurcation points (yellow). Black arrows point to the range in conduction velocity considered in each case. Note the higher range of values associated with global coupling and lower for conduction velocity in the stroke case.

Table 5.2 State variables and parameters of the Stefanescu-Jirsa 3D model and corresponding range of values used in the present study

Parameter	Value	Description
a, b, c, d	1, 3, 1, 5	Constants affecting faster ion channels
R	0.006	Constant affecting slower ion channels
S	4	Bursting strength of model
μ and σ	2.2, 0.3	Mean and dispersion of input current in each node
X_0	-1.6	Leftmost equilibrium point of X
IE, II	Derived from μ and σ	Models excitability of each node and mode (IE for excitatory input, II for inhibitory input)
Long-range Coupling	0.01-1.0	Coupling scaling factor for connections between nodes
Conduction velocity	10-100	Scales delay for defined internode distances
β, γ	4, 5	Corresponding values for IPs
K_{12},K_{21},K_{11}	0.01-1.0	Models coupling between excitatory and inhibitory populations within nodes

Values used for the simulation included long-range coupling, conduction velocity, and K_{12}, K_{21}, and K_{11} optimized via parameter space explorations. Default values were used for all other variables.

D. Results

Weights of structural connections after stroke

The weights of connections in the control group had a mean (± SD) of 10.16 ± 1.03, (range 8.75-12.07), and in the stroke cohort had a mean of 9.76 ± 1.57 (range 6.41-10.35) (**Figure 5.4**). Yet, there were no statistical differences in mean, distribution shape between the groups (Kolmogorov-Smirnov test; p_a = 0.42), or skewness (controls = -0.083; stroke = -0.082; t-test: p=0.35 and 0.29 respectively).

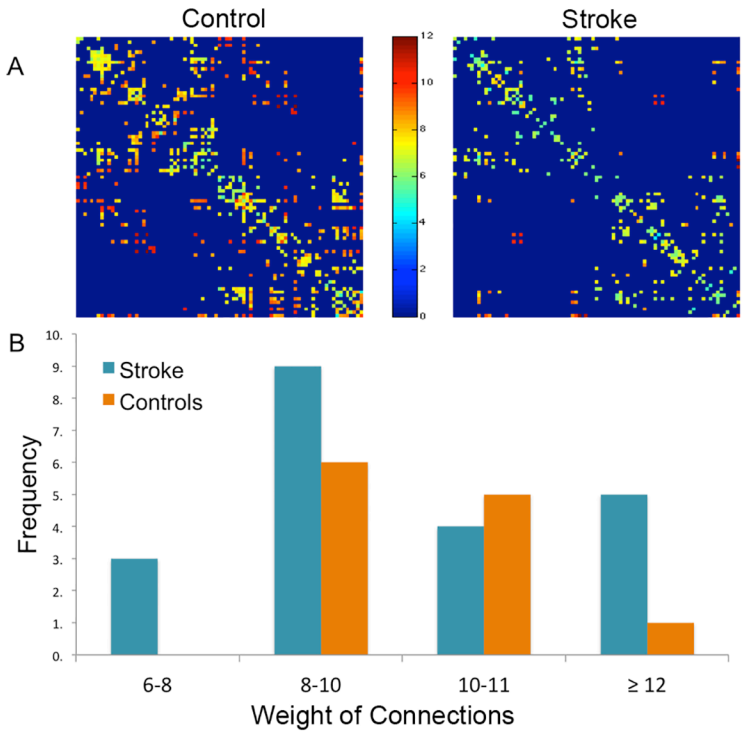

Figure 5.4 Weights of structural connections in stroke and healthy controls.

(**A**) Structural connectivity matrices in a healthy control (left) and one individual with stroke (right). Dark blue denotes absence of connections while hotter colors indicate stronger weights. (**B**) Frequency distribution of weight of connections in healthy controls (orange bars) and stroke (blue bars).

*BOLD simulations generated with TVB correlated with the empirical BOLD responses (**Figure 5.5**)*

The frequency spectrums of the simulated and the empirical BOLD responses had similar ranges (0-0.25 Hz) and mean peak (empirical = 0.05+0.035 Hz; simulated = 0.03+0.023 Hz). Although the mean amplitudes were similar (empirical = 8.15; simulated = 9.49), the range of values was wider in the empirical signals (0.17 – 87.43) than those found in the simulated BOLD (3.79 – 22.64). The relative phases of the regions within simulated and empirical time series were similar as assessed by the mean correlation coefficient between their respective functional connectivity matrices (mean = 0.27±0.02; p_b = 0. 9e-12 Fisher Z-transformation). These validated simulations provided us with specific parameter values at both the global and the local levels associated with healthy control subjects and after stroke.

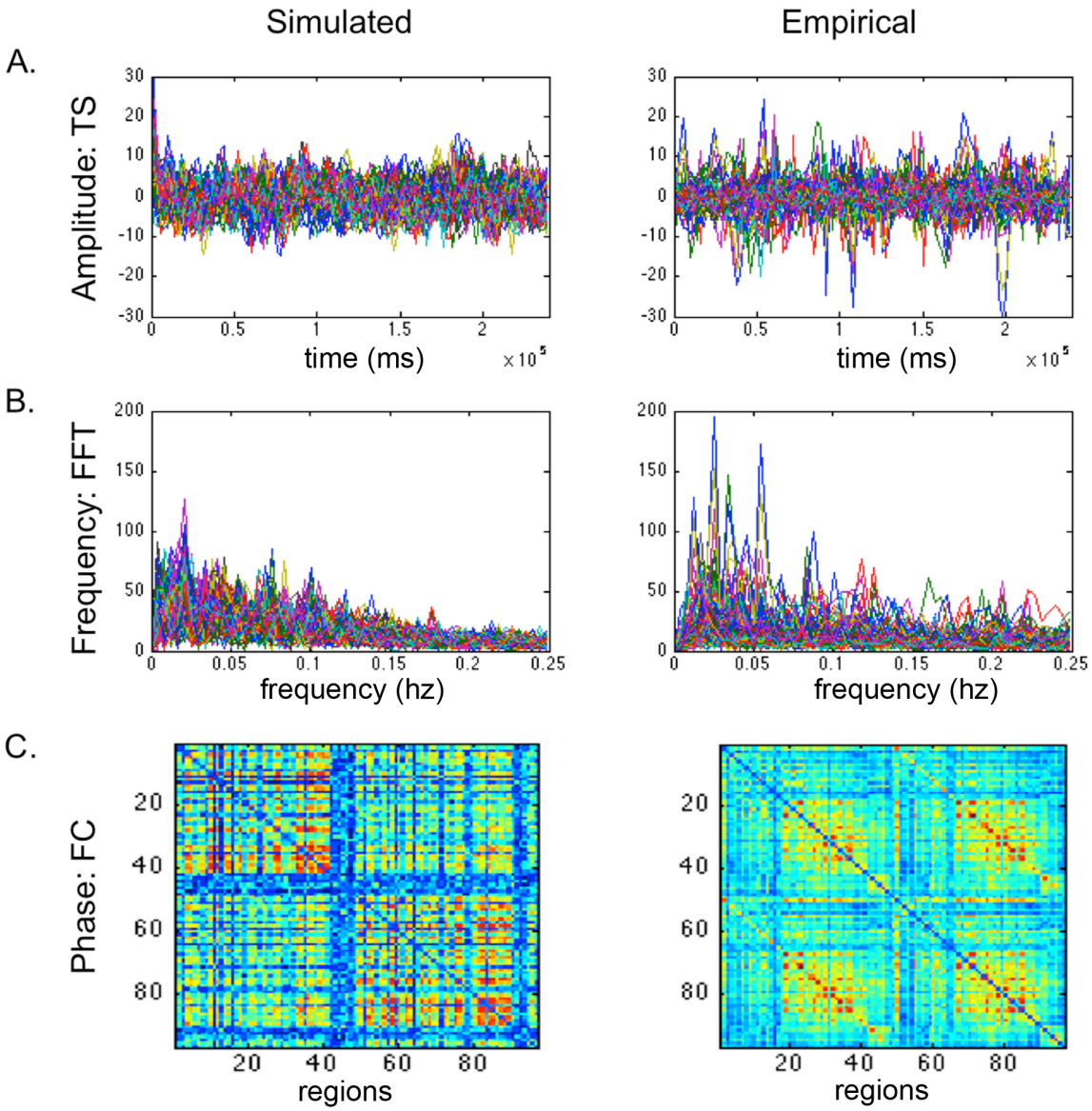

Figure 5.5 Comparison of simulated and empirical BOLD signals.

(**A**) Amplitude: Example of a raw simulated (left) and empirical (right) time series (TS). Amplitudes are indicated by the maxima and minima of the time series. (**B**) Frequency: Frequency distribution graphs (FFT) of the simulated (left) and empirical (right) time series. Note that both empirical and simulated signals have the same range, profiles, and peaks. (**C**) Phase: Functional connectivity (FC) matrix based on simulated time series (left) and the empirical group matrix (right).

*Stroke was associated with reliable changes in global and local parameters (**Table 5.3**)*

Although qualitative in nature, the color-coded graphic representation of the variance distribution done as part of the parameter space exploration (**Figure 5.3**) provides a glimpse into

differences of combined values for the two global parameters: long-range coupling (x axis) and conduction velocity (y axis) in healthy controls and in stroke subjects, with warm colors representing higher variance. These explorations demonstrated at this early stage of analysis that the range of optimal parameter values (hot colors) in controls had similar topology of the distribution of variance as well as concrete values. In contrast, stroke cases displayed high variations in both topology and values, where although some had similar distribution patterns as the healthy controls (e.g. Panel C), others had scattered, fragmented patterns (panels D and E). Similar observations were found with respect to local parameters.

Numerically, differences in parameter values between healthy controls and the stroke cohort are as follows:

Global Parameters

a. Conduction velocity: The range of modeled conduction velocities obtained via TVB in healthy controls ranged from 45 to 90 m/s with a mean of 62 ± 10 m/s. In contrast, the conduction velocities in stroke subjects had a range between 12 and 80 m/s with a mean of 46 ± 21 m/s. Comparison between the two groups with Wilcoxon rank sum test (p_c = 0.05) was marginally significant after correction for multiple comparisons.

b. Long-range coupling (rescale factor of incoming activity linking global with local dynamics): In healthy controls, the mean was 0.053 ± 0.009 (range 0.044-0.047) and in cases with stroke the mean was 0.061 ± 0.016 (range 0.04-0.09). Wilcoxon sum rank test showed this difference was significant after correction for multiple comparisons (p_c = 0.013).

In addition, it is important to note that the trend in all stroke cases where the values were different from those in controls was consistent: that is, it presented always as a decrease in conduction

velocities (N = 12) and an increase in long-range coupling (N = 14). The rest of the stroke cases did not show differences with healthy controls.

Local parameters derived from the Stefanescu-Jirsa3D model

a. K_{12} (coupling of excitatory over inhibitory populations within brain regions): The values of K_{12} in stroke had a mean of 0.49 ± 0.338 (range 0.12-0.55) and in controls the mean was 0.225 ± 0.166 (range 0.12-0.55). Statistical comparison between the two groups resulted in a $p_c = 0.17$.

b. K_{21} (coupling of inhibitory over excitatory populations): This variable (healthy control mean = 0.804 ± 17, range=0.3-0.9) was significantly reduced in the stroke group (mean = 0.674 ± 0.302; range 0.1-0.9; $p_c = 0.01$).

c. K_{11} (influence between excitatory populations): The values of K_{11} in controls had a mean of 0.883 ± 0.142 (range 0.6-0.95) and in stroke cases had a mean of 0.613 ± 0.301 (range 0.1-0.99). Comparison between the two groups with Wilcoxon sum rank test gave a $p_c = 0.1$.

In summary, compared to values in healthy controls, there was a higher long-range coupling and a decrease of local inhibitory dynamics represented by the local parameter K_{21} along with a trend towards a reduction of conduction velocity.

Group	Variable	Range	Mean	SD	Wilcoxon Rank Sum (p)
Control	Global Variables:				
	Global Coupling	0.044-0.047	0.053	0.009	
	Conduction Velocity	45-90	61.9	9.9	
	Model Variables:				
	K_{12}	0.12-0.55	0.49	0.338	
	K_{21}	0.3-0.9	0.804	0.17	
	K_{11}	0.6-0.95	0.833	0.142	
Stroke	Global Variables:				
	Global Coupling	0.04-0.09	0.061	0.016	0.013
	Conduction Velocity	12-80	46	21	0.05
	Model Variables:				
	K_{12}	0.1-0.8	0.369	0.257	0.17
	K_{21}	0.1-0.9	0.674	0.302	0.01
	K_{11}	0.1-0.99	0.613	0.301	0.1

Table 5.3 Summary of long-range and local parameters used in TVB to simulate BOLD time series in healthy controls and individuals with stroke.
SD = standard deviation. p = probability resulting from the Wilcoxon sum rank test comparing parameter values between the two groups.

Global and local parameters were correlated with clinical phenotype

Multiple linear regression analysis to establish a relationship between modeling parameters and some clinical metrics did not show a correlation. The following clinical elements were considered in this preliminary assessment: stroke phenotype (size, location, time after stroke, side of stroke), depression, patient demographics (age, sex), and severity of impairment.

Next, we assessed the relationship between parameter values with recovery from stroke immediately after therapy and after one year (maintenance) using a multiple linear regression. This analysis showed a negative relationship between K_{12} and Fugl-Meyer scores both post-therapy (t=-2.386; p_d =0.038) and at maintenance one year later (t=-3.824; p_d=0.005). In addition, long-range coupling had a positive relationship with the Wolf Motor Function Test (t=2.461; p_d =0.039) at maintenance. Thus, these two parameters derived from modeling based on pre-therapy conditions

were related to long-term motor gains rather than the physical features of the stroke or the patient's demographics (**Figure 5.6**).

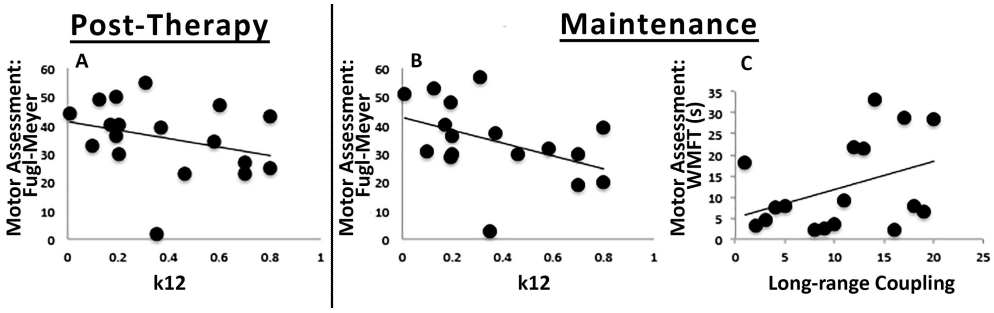

Figure 5.6. Correlation between modeling parameters and post-therapy motor outcomes.

Scatterplots showing correlation between modeling parameters (x-axis) and post-therapy motor outcomes (y-axis). Clear relationships were found between (A) k12 and Fugl-Meyer (Post-therapy), (B) k12 and Fugl-Meyer (Maintenance), and (C) Global coupling and WMFT (Maintenance).

	Comparison of Interest	Data Structure	Type of Test	Exact p value
a	Weights of connections: stroke vs. control	Normal	Kolmogorov-Smirnov test	0.42
b	Pearson's correlation coefficients: simulated vs. empirical functional connectivity matrices	Normal after Z-transformation	T test	0.9e-12
c	TVB parameters: stroke vs. control	Control: Non-normal Stroke: Normal	Wilcoxon rank sum test	Conduction Velocity: 0.05
				Long-range Coupling: 0.013
				K_{12}: 0.17
				K_{21}: 0.01
				K_{11}: 0.1
d	Regression: TVB parameters with subject demographics, lesion characteristics and recovery	Normal	Multiple linear regression	Post-Therapy: K_{12} - Fugl-Meyer: 0.038
				Maintenance: K_{12} – Fugl-Meyer: 0.005 Long-range Coupling – WMFT: 0.039

Table 5.4 Statistical Table

E. Discussion

The main result of the study showed that the simulation of BOLD signals using TVB in stroke enables the identification of key changes associated with large-scale neural dynamics in individual patients. Overall, our results showed that, compared to healthy controls, individuals with stroke have a consistent reduction in conduction velocity and a relative increase in local-over-global brain dynamics. Further, the identified parameters were related to functional outcomes such that these parameters predicted long term recovery after therapy. Taken together, these results not only back TVB as an effective tool in identifying dynamic brain changes in stroke spanning multiple scales, but also specifically identify potential predictors of recovery in stroke at the individual level. This study suggests that TVB may be a powerful platform for the application of large-scale modeling in understanding brain mechanisms at an individual subject level.

Stroke is related to consistent global and local parameter changes

The successful simulation of empirical rfMRI data in this study facilitated a particularly salient finding; the dynamic model derived from stroke subjects had a significant decrease in the local parameter K_{21} and a consistent long-range coupling increase, accompanied by a trend in decreased conduction velocity. Two aspects of these results are of special interest: the first relates to the nature of the statistical outcomes and the second to the biological interpretation of these changes.

1) Imaging-derived metrics in humans in general have high variance (Mueller et al., 2013a); consequently, analytical measures have been developed to minimize it (Fischl et al., 1999a). Further, this variance is amplified by stroke (Rehme et al., 2012), and has compelled researchers to stratify patients with precise criteria (Cramer, 2010), resulting in low sample sizes and high inter-study variability. In contrast, even when we used minimal exclusion criteria when selecting participants,

changes seen after stroke were highly consistent, where all the cases that had a parameter change with respect to controls had the same directionality and relatively low variance. Given the high level of subject variability (as expected for a cohort including a large range of clinical phenotypes), we find this consistency somewhat surprising. However, we are not suggesting high reliability of our modeling, as the definitive answer will result from expanding the assessment to a larger population where the predictive value of the parameter changes can be formally assessed.

2) Stroke survivors exhibited a significant decrease in K_{21}, a parameter at the mesoscopic level that represents the influence of inhibitory on excitatory neuronal populations. A decrease in K_{21} thus indicates local dis-inhibition. These results are highly consistent with existing data on the basic mechanisms of stroke at the cellular level. For example, rodent models of MCA stroke show an imbalance in the density of excitatory and inhibitory receptors in tissue surrounding the lesion (Schiene et al., 1996). Specifically, they suggest a decrease in GABA receptor expression in widespread ipsilesional cortical areas and a concomitant increase of N-methyl-D-aspartate (NMDA) receptor expression in the contralesional hemisphere.

In the context of stroke in humans, hyper-excitability has been described in two experimental paradigms:

1) Studies using TMS to test cortical excitability after stroke have shown a decrease in the current needed to elicit motor evoked potentials (MEPs) and an increase in their amplitude (Hallett, 2007) along with an expansion in the area producing them (Liepert et al., 2000) suggesting dis-inhibition in motor cortices (Shimizu, 2002). Furthermore, decreasing the hyper-excitability via repetitive low frequency stimulation (Takeuchi et al., 2005) along with a reduction of the TMS stimulation area (Liepert et al., 2000) has been related to motor recovery (Hallett, 2007).

2) Increased activity in motor and non-motor regions has been reported in fMRI studies after stroke (Rehme and Grefkes, 2013). Although this has been explained as a recruitment of supplementary areas to assist movement (Rehme and Grefkes, 2013), others have related it to widespread cortical hyper-excitability (Buchkremer-Ratzmann et al., 1996), suggesting long-range cortico-cortical inputs (Logothetis et al., 2001) with increased activation via decreased inhibition (Blicher et al., 2009; Liepert, 2003). Functional recovery has in turn been associated with the degree of recovery of activity in the affected cortical areas (Cramer, 2008).

Complementing the above, our results show a correspondence between local and global levels. Indeed, the reduction in local inhibitory influence over excitatory populations was accompanied by an increase in long-range coupling, reflecting an imbalance after stroke between global and local brain dynamics, favoring the latter. That is, local dynamics exert a stronger influence than global dynamics following stroke. In this case, the imbalance could be exacerbated by the decrease in conduction velocity. Interestingly, this imbalance has also recently been modeled in other brain diseases. For example, early stages of schizophrenia have been associated with a breakdown of local dynamics occurring prior to the disruption of global dynamics occurring later on in disease progression (van den Berg et al., 2012; Rubinov et al., 2009).

A particularly interesting finding was the trend associated with decrease in conduction velocity in individuals with stroke as it has previously been described through measurements of central motor conduction times (CMCT) via transcranial magnetic stimulation (TMS) in the primary motor cortex. Immediately following stroke, CMCT decreases and correlates with functional measures (Abbruzzese et al., 1991; Pennisi, 2002) tending towards an incomplete normalization over the long-term (Heald et al., 1993). That said there is a paucity of information on decrease conduction velocity on cortico-cortical

connections. The bulk of knowledge derives from studies in rodents showing structural changes to axons and oligodendrocytes in the primary lesion and the ischemic penumbra (Rosenzweig and Carmichael, 2015). And although some degree of remyelination occurs in the recovery phase, the process is often arrested before completion (Syed et al., 2008). In human autopsy samples, there is an increase in nodal and paranodal lengths adjacent to lacunar lesions (Hinman et al., 2015), which may lead to decreased conduction velocities (Rasband, 2011). Our results thus provide direction for future animal studies, exemplifying the translational nature of TVB findings.

TVB thus appears to be effective at modeling brain activity in healthy brains and those impacted by disease processes, and has the novel capability of studying brain dynamics at multiple scales, including at a level that has thus far only been available via animal models or surrogate neuroimaging markers in humans. Applying this method of modeling, which is tied directly to biological mechanisms, to existing large datasets opens up the possibility to experiment with expanded models of brain states, including a myriad of diseases and their potential treatments.

Potential Predictors of Motor Recovery after Stroke

Our results demonstrated that local (K_{12}) and global (long-range coupling) parameters, derived from pre-therapy conditions, were significantly correlated with motor gains post-therapy and at maintenance. Furthermore, both parameters point in the same direction, as poor recovery was associated with an increase in local excitatory influences and with an emphasis on local dynamics, whereas values closer to controls correlated with better recovery.

Interestingly, TVB parameters in stroke did not correlate with severity of disease at the pre-stroke time point, even though the structural connectivity matrix used in the modeling coincided with this time point. In addition, other physical features of the stroke (size, location) or patient

demographics (sex, age) did not correlate with the modeled parameters. Finally, neither lesion characteristics nor patient demographics correlated with recovery, highlighting the unique predictive potential of these parameters.

The question then becomes to what extent these parameter estimates can be used as predictors of recovery at the individual patient level. . While a cross-validation approach using the current data set could serve to answer this question, a new and larger stroke cohort is ideal in obtaining estimates of the sensitivity and the specificity of our markers, due to high variance in stroke. However, there is clear value of our observations even with this limitation. At present, biomarkers for stroke recovery have been limited by the use of "substitute or surrogate" measures derived from brain imaging or electrophysiology, mainly due to the inability to measure *in vivo* more ideal basic elements, i.e., at molecular or cellular levels (Burke and Cramer, 2013). Indeed, such elements may be observed more closely in animal models, but are difficult to translate to humans due to the limited homology between species. Specifically, the Stefanescu-Jirsa 3D model used in this study evolved from the mesocopic level Hindmarsh-Rose model. The Hindmarsh-Rose model itself is rooted in the principles of the Hodgkin-Huxley neuron equations, in addition to dynamics based on bursting neurons found in invertebrate circuitry (Hindmarsh and Rose, 1984). Further, the neural behaviors described by the Hindmarsh-Rose model have been biologically verified in other animal models (Gu, 2013; Selverston and Ayers, 2006). Therefore, while any model of the meso-scale does not encompass the complexity of brain processes at the cellular level, there is likely emergence of behavior from the cellular level to the mesoscopic level, exhibiting deterministic behavior that can be modeled and also observed *in vivo*.

That is, the transition between the macro- and microscopic level is represented by population dynamics at the mesoscopic level (Mitra, 2014). From this, one could conclude that the path towards

basic biomarkers should include the intermediate mesoscopic level. Indeed, TVB allows one not only to estimate parameters at that level but also to link it to the macroscopic global whole-brain level. TVB is not unique in considering biophysical parameters as exemplified by inference models based on DCM (Moran et al., 2011). Basically, there are no conceptual differences in the inferential goals between TVB and DCM but they do differ in the detailed mechanics. For example, whereas TVB develops the model at the level of large-scale networks, DCM focuses on portions of these networks. Second and perhaps the key contrast is that while DCM fits the parameter of the model but does not generate data, TVB uses the model to generate data making these two approaches highly complementary.

An interesting and unique aspect of TVB is its highly individualized approach as parameter estimates are derived from individualized structural connectivity matrices obtained from each subject, at hence, it can provide the first step to customize *individual* therapeutic interventions. For example, our ongoing work is beginning to test potential "virtual interventions" by modifying specific parameters changed after stroke and determining the degree of restoration of brain dynamics on each stroke patient.

A second ability of this modeling approach is to use the model of an individual patient's brain connectivity that can be objectively measured and evaluated as an indicator of normal biological processes (such as resting state activity, rsfMRI), pathogenic processes, or pharmacologic responses to therapeutic intervention (Group, 2001). Dynamics of rsfMRI are highly non-stationary (Allen et al., 2014) and existing metrics, including the direct correlation between functional and structural connectivity, are so far incapable of addressing this issue satisfactorily (Goni, 2013). A number of studies have therefore used generative modeling to parse the relationship between structural and functional connectivity. A recent study (Andersen et al., 2014) demonstrated that the fusion of TVB-like

network modeling with structural neuroimaging explains the non-stationary dynamics observed in rsfMRI. Thus we propose a conceptual paradigm shift, in which the dynamic model shifts the non-stationary functional data from imaging at the mesoscopic scale to a more deterministic set of coefficients in a brain model. In other words, complex dynamics cannot be captured by stationary imaging analyses, but can be generated by a data-constrained mechanistic model of brain circuit dynamics, as seen in the generative modeling approach detailed in stroke (Brodersen et al., 2011). Thus, the mathematical model could be seen as a compact generator of dynamics-based biomarkers, or even as the biomarker itself. The primary benefit, as we demonstrated here, is that it becomes easier to understand disease mechanisms by evaluating the coefficients of the model.

Of note, the approach used in this study to validate the simulated time series was to compare frequency, amplitude and phase of the simulated and empirical signals. After the refinement of the TVB models, future studies will incorporate a larger variety of multi-dimensional analyses, particularly with respect to temporal variability in resting state signals. Furthermore, the current study determined optimal values of local parameters applied to all brain regions. Future studies will focus on local parameters for subsets of brain regions, e.g., changing parameters of nodes within and/or around a stroke lesion to determine how this impacts the resultant simulated brain activity. We also note that the translational power of our findings depend upon the reproducibility of parameters for a given brain state, the answer for which will emerge with expanded application of TVB to other cohorts. The results from this study thus confirm that TVB allows the assessment of biophysical variables previously unattainable in human studies. This method provides a potentially important and novel application of large-scale modeling, in which we can probe brain dynamics and biomarkers on an individual level.

Therefore, The Virtual Brain has the potential to become an important step towards the development of individualized medicine in stroke.

CHAPTER 6

The Virtual Brain: Modeling Biological Correlates of Recovery after Chronic Stroke

A. Abstract

There currently remains considerable variability in stroke survivor recovery. To address this, developing individualized treatment has become an important goal in stroke treatment. As a first step, it is necessary to determine brain dynamics associated with stroke and recovery. While recent methods have made strides in this direction, we still lack physiological biomarkers. The Virtual Brain (TVB) is a novel application for modeling brain dynamics that simulates an individual's brain activity by integrating their own neuroimaging data with local biophysical models. Here, we give a detailed description of the TVB modeling process and explore model parameters associated with stroke. In order to establish a parallel between this new type of modeling and those currently in use, in this work we establish an association between a specific TVB parameter: Long-range coupling that increases after stroke with metrics derived from graph analysis.

We used TVB to simulate the individual BOLD signals for 20 patients with stroke and 10 healthy controls. We performed graph analysis on their structural connectivity matrices calculating degree centrality, betweenness centrality and global efficiency. Linear regression analysis demonstrated that long-range coupling is negatively correlated with global efficiency ($p=0.038$), but is not correlated with degree centrality or betweenness centrality.

Our results suggest that the larger influence of local dynamics seen through the long-range coupling parameter is closely associated with a decreased efficiency of the system. We

thus propose that the increase in the long-range parameter in TVB (indicating a bias towards local over global dynamics) is deleterious because it reduces communication as suggested by the decrease in efficiency. The new model platform TVB hence provides a novel perspective to understanding biophysical parameters responsible for global brain dynamics after stroke, allowing the design of focused therapeutic interventions.

B. Introduction

Heterogeneity of functional outcomes following stroke remains a major limitation to stroke rehabilitation. While the majority of stroke survivors suffer from motor impairment, particularly in the upper extremities(Nichols-Larsen et al., 2005), the degree and type of this impairment and the level of recovery following rehabilitation is highly variable(Reinkensmeyer et al., 2012). The functional basis for variation in patient deficits is still poorly understood, and there is no consensus on a theoretical or empirical framework for linking brain injury to functional deficits(Jirsa et al., 2010). In order to address this issue, recent approaches in stroke rehabilitation have aimed at the development and the optimization of individualized treatments that maximize long-term functional gains (Cramer, 2010; Munshi and Sharma, 2015).

To this end, different theoretical approaches have been used. The most general method has probed stratification measures based on patient demographics, behavioral outcomes, affective states, brain function and lesion characteristics (Burke and Cramer, 2013; Cramer, 2010; Munshi and Sharma, 2015). None have been shown as a reliable biomarker. Particularly noticeably has been the presence of an inconsistent relationship between brain lesion and the

resulting functional deficits (Burke and Cramer, 2013), likely due to the inherent complexity of damage in a highly interconnected brain.

Researchers have thus turned to network analysis to understand stroke (Baldassarre et al., 2014; Carter et al., 2012; Smith et al., 2013). In this approach, one of the goals is to explain the observed variations after stroke and predict recovery. Interestingly, the initial efforts with network analysis focused on alterations to specific pathways as the key links to understand behavior (Carter et al., 2012; Ward, 2003). For example, while some functional connectivity studies showed that lesions within the motor areas can cause dysfunction of remote brain regions (Carter et al., 2010; Rehme and Grefkes, 2013; Wang et al., 2010b), others showed a relationship between improved motor function and strengthening inter-hemispheric and intra-hemispheric connectivity involving the primary motor cortex (Grefkes and Ward, 2013). An important issue in interpreting such relationships is that the changes may reflect either the abnormal functioning of a damaged network, or the formation of a different network that results in new behavioral patterns.

Furthermore, while these initial studies have been an important development, their main limitation is that they assume stable, localized changes within specific sub-networks, obliterating global changes, with the consequence that these potential biomarkers have been very adequate as descriptors at the group level but not in individual patients (Mueller et al., 2013b).

Recently, the neuroimaging community has begun to focus on connectomics, or the mapping of all connections at the whole brain level. These connectomes, derived from structural (DTI) or functional outputs (fMRI, EEG) have recently been termed “big data”,

referring to datasets that require the generation of large amounts of multi-modal imaging data, (including raw, pre-processed, and intermediate data), for a high number of subjects (Poldrack and Gorgolewski, 2014). These initiatives span normal function (Human Connectome Project (Sotiropoulos et al., 2013), CONNECT (Assaf et al., 2013), Brainnetome (Jiang, 2013), development (NIH Pediatric Database) and brain disorders such as Alzheimer's disease (Alzheimer's Disease Neuroimaging Initiative).

In order to help interpret such large datasets, graph theory is increasingly used to distinguish inherent patterns that likely correlate with brain networks at the whole brain level. Using connectomics and graph theory, specific brain regions can be understood as nodes (Rubinov and Sporns, 2010), and lesions can be understood as damage to nodes and/or the connections among them. With these methods, stroke has been shown to produce changes in both structural and functional network connectivity, particularly related to the organization of "hubs", or highly interconnected nodes (Crossley et al., 2014; Sporns, 2014). Graph theory provides an assessment of the changes at an organizational level. However, this approach still suffers from some limitations, mainly the inability to determine dynamical changes in a constantly changing brain and the lack of concrete biophysical substrates for understanding those dynamics. Consequently, according to Smith et al, one of the major challenges in the field of functional connectomics "*will be to enable application of biologically interpretable models using large numbers of nodes in a robust and practical way*"(Smith et al., 2013).

In other words, although tackling questions about brain network dynamics in both healthy and stroke populations requires a great deal of data, simply collecting more data is not itself an answer. While these efforts provide the necessary empirical foundation, they lack a

computational and theoretical framework with quantitative tools to link these multiple datasets to “reconstruct” the brain, and provide the link between these data and the brain function of individuals.

In this context, novel theoretical perspectives have been proposed based upon the nature of the brain as a large-scale network (Ghosh et al. 2008; Jirsa et al. 2010; Deco, Jirsa, McIntosh 2011,2013). The implementation of the framework has been significantly accelerated by The Virtual Brain (TVB), a novel large-scale neural modeling platform (Sanz-Leon 2013, 2015, Woodman et al 2014). TVB uses neuroimaging data to parameterize a model and because individual data is used, the individual person’s brain can become a “virtual brain”.

The Virtual Brain (TVB, thevirtualbrain.org) was developed as a platform for modeling the dynamics of large-scale neural systems(Jirsa et al., 2010; Ritter et al., 2013b). TVB integrates structural long-range connectivity generated from empirical DTI data with mesoscopic, or local level models (at each node/ region of interest (ROI)). By combining these two scales (global connectivity with local dynamics), TVB is able to predict and simulate an individual’s brain activity, essentially modeling a virtual representation of their brain. TVB thus lies at the intersection of experimental and theoretical neuroscience, making it well positioned to provide a link between population and individual datasets.

The models available in TVB integrate the anatomical connectivity between parts of the brain (provided by DTI) and the dynamics of local neural populations (embedded in the platform). Using these models, TVB has the flexibility to generate simulated data ranging from local field potentials to EEG and fMRI BOLD signals, allowing for a multi-modal link between simulated and empirical data. The scalable architecture of TVB allows us to include

neurophysiological information (e.g., receptor distributions, ion channels) adding another level of detail and bringing the model's behavior closer to the real brain. Spatiotemporal motifs as present in empirical EEG/fMRI data can be reproduced to a large degree (Ritter et al. 2013). Because biophysical parameters are invisible to brain imaging devices, TVB acts as a "computational microscope" that allows the inference of internal states and processes of the large-scale model.

TVB therefore serves as a powerful research tool to that has the potential to utilize big data and to develop and test advanced theories of brain dynamics. The individualization of TVB allows the creation of one model per person and systematically assesses the modeled biophysical parameters related to individual differences. The natural extension of this approach goes further into clinical applications, deriving parameters that both relate to biophysics and predict clinical outcome, making TVB an ideal tool for addressing limitations in stroke research.

The objective of this manuscript is two-fold:

1) To give a thorough overview of the modeling method employed using The Virtual Brain as it pertains to stroke, with the goal of providing details for those interested in using it in the context of stroke.
2) To provide a link between one of the TVB parameters (long-range coupling) to current whole brain analytical approaches based on graph analysis.

C. Materials and Methods

Subjects

Twenty individuals with ischemic stroke in the middle cerebral artery territory (41.13±23.78 months post-onset) and 10 age-matched controls were recruited for the study. Demographics for all stroke subjects are shown in **Table 6.1**.

Table 6.1 Demographics and stroke characteristics of the stroke cohort

Subject	Age	Sex	Handedness	Affected Hemisphere	Affected Hand	Stroke Location	Stroke Volume (mm^3)
1	41	F	Right	Right	ND	Cort	22495.0
2	54	F	Right	Left	D	Cort/subcort	49078.0
3	57	M	Right	Left	D	Cort/subcort	17411.0
4	57	M	Right	Left	D	Cort/subcort	38703.0
5	54	F	Right	Left	D	Subcort	27677.0
6	50	M	Right	Right	ND	Subcort	3570.0
7	23	M	Right	Left	D	Subcort	560.0
8	55	F	Right	Right	ND	Cort	6781.0
9	68	M	Right	Left	D	Subcort	1988.3
10	56	F	Right	Left	D	Subcort	6239.7
11	46	M	Right	Left	D	Subcort	325.0
12	56	F	Left	Right	D	Cort/subcort	60669.0
13	37	M	Right	Left	D	Cort/subcort	83406.2
14	62	M	Right	Left	D	Subcort	22154.8
15	57	M	Right	Right	ND	Cort/subcort	25392.0
16	66	M	Right	Left	ND	Cort/subcort	19927.0
17	61	M	Right	Left	D	Subcort	978.0
18	74	M	Right	Left	D	Cort/subcort	63642.0

19	67	F	Right	Right	ND	Subcort	588.0
20	74	F	Right	Left	D	Cort/subcort	44892.0

D = dominant hemisphere; ND = non-dominant, Cort = cortical; subcort = subcortical.

Imaging Acquisitions

Magnetic resonance images were collected using a 3T Philips scanner and an 8 channel SENSE head coil for signal reception and body coil transmitter for signal excitation. The following sequences were used:

4. High-resolution anatomical images (T1-w): 3D Magnetization Prepared Rapid Gradient Echo (MP-RAGE) sequence, FOV= 250x250, resolution=1x1x1mm, SENSE reduction factor =1.5, TR/TE=7.4/3.4ms, flip angle=8, sagittal orientation, number of slices=301 covering the whole brain.
5. Diffusion Tensor Imaging (DTI): FOV=224x224, TR/TE=13030/55, 72 slices, slice thickness= 2mm, resolution=0.875x0.875x2, 2 mm post-processing iso-voxel with b=1000 sec/mm^2 (and b=0), 32 diffusion directions.
6. Functional imaging acquisition at rest (rsfMRI): whole brain (37 slices), single-shot echo-planar MR (EPI), slice thickness = 4.0 mm, FOV= 230x230, voxel size = 2.8mm x 2.8mm, TR/TE= 2000/20 ms, duration= 5 min.

rsfMRI Pre-processing

Resting state fMRI pre-processing analysis was performed using AFNI functions (Cox, 1996) and included the following steps:

1. Motion correction using a 6 parameter 3D registration of functional and anatomical data sets (Cox and Jesmanowicz, 1999).
2. 3D spatial registration to a reference acquisition from the first fMRI run.

3. Registration of functional images to the anatomical volume.
4. Despiking of the time series.
5. Mean normalization of the time series.
6. Inspection and censoring of time points occurring during excessive motion (>1mm; (Johnstone et al., 2006).
7. Regression of cerebrospinal fluid and white matter signals to remove slow drift in the fMRI signal.

Pre-processing : Structural Connectivity

Brain Parcellation

Parcellating image data that contain lesions with the use of semiautomated schemes produce inaccurate results due to the absence of tissue and consequent mechanical deformation. We therefore developed the "Virtual Brain Transplant" (VBT). This method effectively replaces the lesion produced by the cortical stroke with T1-with images of brain tissue from the contralesional hemisphere from the same subject (Solodkin et al., 2010). This method allows us to use a semiautomated parcellation scheme subsequent to the transplant. The VBT process consisted of the following steps **(Figure 6.1)**:

5. Lesion segmentation by hand.
6. The high-resolution anatomical T1-w brain images and lesion masks were uploaded to a transplantation pipeline, which dissected the MRI brain tissue from the non-lesioned hemisphere homologous to the lesion, and transplanted it into the lesioned hemisphere at the site of the lesion, filling in the missing portions of the brain.
7. After the initial transplant was done, manual corrections in the interface between the

native and transplanted T1-w images were performed.

8. The brain was segmented into 83 cortical and subcortical regions using the Lausanne 2008 (Freesurfer) parcellation scheme within the Connectome Mapper Toolkit (Fischl et al., 1999b; Gerhard et al., 2011).

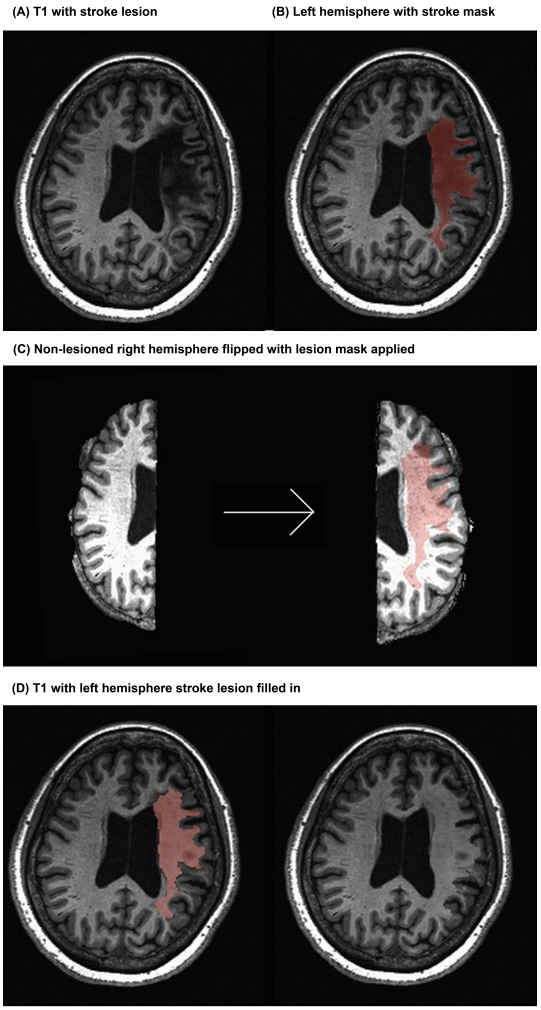

Figure 6.1 Virtual Brain Transplant Method.
Virtual Brain Transplant is done in stroke cases with cortical damage with the goal of being able to parcellate the brain. This graphic representation summarizes the process of replacing the damaged portion of the brain with the homologous non-stroke tissue. (A) T1-w image showing the lesion (left hemisphere) of one subject. (B) Close-up of the left hemisphere, demarcating the lesion mask in red. (C) Segregation of the right and left hemispheres (left) and after the right hemisphere has been flipped having the lesion mask applied (right). (D) Depiction of the tissue from the right hemisphere applied to the lesion in the left hemisphere (left) and the resulting transplanted brain volume (right).

T1-w to DTI Alignment

The T1-w anatomical image was then aligned to a reference b=0 sec/mm^2 DTI image, using a 6 degrees of freedom linear transformation with FSL's FLIRT function (Jenkinson et al., 2002). This transformation was also applied to the Freesurfer parcellations.

DTI Tractography

We performed the following steps:

1. DWI were aligned to the same reference b=0 sec/mm^2 image used to align the corrected T1-w via Virtual Brain Transplant to DTI. Distortions caused by eddy currents and head motion were corrected using the FSL eddy current correction (12 degrees of freedom linear transformation), and the diffusion gradient vectors rotated accordingly (Leemans and Jones, 2009). That is, the T1-w images with the "transplanted masks" are used to supply the region of interest landmarks for tractography, but do not directly impact the tractography algorithm as the transplant is not performed in the DWI space.
2. The diffusion-weighted images were resampled to 2mm isotropic resolution (Wedeen et al., 2008).
3. White matter deterministic tractography of DTI data was performed in Trackvis software (Wedeen et al., 2008) using the FACT algorithm (Mori and van Zijl, 2002). Threshold values of a maximum of 60 degrees turning angle and a minimum of 0.20 fractional anisotropy were used as stopping criteria for the tracking algorithm. These thresholds take into account the decrease in signal in regions with the lesion. The fractional anisotropy threshold is particularly useful in terminating tracks before they enter regions containing the lesion. These regions, filled with CSF, have fractional anisotropy values close to zero. Therefore

white matter pathways ordinarily connecting two ROIs will not be tracked if the ROI is completely lesioned, despite appearing intact in the transplanted T1-w image from which the parcellation is made. If a parcellation is partially compromised by the lesion then white matter pathways will also be partially tracked as reflected by a lesser number of streamlines.

Generation of Structural Connectivity Matrices

Using the Connectome Mapper Toolkit, two connectivity metrics were extracted for each pathway in order to generate two structural connectivity matrices that quantify connectivity between all pairs of the cortical regions for each subject:

1. Weights, defined as Fractional anisotropy (FA)*number of streamlines in the pathway (note that per the white matter deterministic tractography of DTI data, pathways connecting regions impacted by the lesion will show a decreased number of streamlines and potentially altered FA. This metric reflects the maximum rate of transmission of information through edges (Zalesky and Fornito, 2009). The number of streamlines in the pathway was assessed using the deterministic FACT algorithm.
2. Lengths of the individual tracts, defined in millimeters, were derived after smoothing the tractography with a B-Spline filter (Wedeen et al., 2008).

These matrices are symmetrical, as connections using DTI are considered unidirectional (Ritter et al., 2013a).

Modeling with The Virtual Brain

Modeling with TVB involves three initial steps, namely the import of individual structural connectivity matrices (obtained as described above), the selection of a biophysical local model, and the choice of relevant biophysical parameter values. TVB has several types of local models

available, each one taking into account different biophysical parameters. Hence, whereas some are focused on field potentials (Stefanescu-Jirsa 2D and 3D), others are focused on firing rates (Wilson-Cowan, Brunel-Wang, Jansen-Rit) or are phenomenological (Generic 2D, Kuramoto, Epileptor). In our previous efforts, since we simulated the BOLD response, the mesoscopic model used was the Stefanescu-Jirsa 3D (SJ3D), one of the more complex and refined models in the repertoire of TVB.

The reasoning behind this choice were not only the obvious relationship between the BOLD response and local field potentials(Sotero and Trujillo-Barreto, 2008; Stefanescu and Jirsa, 2008; Turner, 2003) but the additional fact that the BOLD signal has poor time resolution and the model does not rely heavily on synaptic delays. Concretely, the Stefanescu-Jirsa 3D model is a reduced form of the Hindmarsh-Rose model(Stefanescu and Jirsa, 2008), which forecasts individual neuronal behavior. The SJ3D model predicts local dynamics using 6 differential equations that include variables representing *physiological properties* such as neuron membrane potentials, transport of ions across the membrane through fast and slow ion channels, and the dynamic coupling of excitatory and inhibitory neuronal populations.

The sequential steps for modeling in TVB are as follows (Graphical depiction can be found in **Figure 6.2**):

1. Importing the two metrics derived from individualized SC matrices (weights (FA*number of fibers) and lengths) representing connections between regions, along with the T1-w structural data providing individual brain topology.
2. Parameter Space Exploration (PSE): The goal of this process is the optimization of the model parameters. When applying TVB methodology to stroke, one can classify the numerous

parameters included in the modeling into two categories: Global parameters that will model brain dynamics between nodes, and local parameters that will describe brain dynamics within nodes. In the first category, the two main parameters to optimize are conduction velocity and long-range coupling. Likewise the biophysical parameters within the Stefanescu-Jirsa 3D model to be used are those providing the coupling between excitatory and inhibitory populations within the local regions: K_{11} (excitatory on excitatory), K_{12} (excitatory on inhibitory), K_{21} (inhibitory on excitatory). This exploration systematically explores the entire range of available values for each parameter, and identifies the value with the highest overall distribution of variance **(Figure 6.3)** as the optimal parameter value to be used on each individual for the actual signal simulation. The order of optimization can be done as follows:

a. Long-range coupling and conduction velocity: starting ranges are 0.001-0.1 global coupling, 1-100 conduction velocity.
b. K_{12} and k_{21}: starting ranges are 0-1.0 for both. K_{12} is optimized first, and the identified value is then used when optimizing K_{21}.
c. K_{11}: starting range is 0-1.0.

3. Simulating the BOLD response: Based on the values obtained in the parameter exploration, simulation of the BOLD time series should reflect the same duration (4 min) and sampling rate (TR=2s) of the empirical MRI acquisition. Noise is added to each node. The noise to be used is white with Gaussian amplitude (mean = 0, standard deviation = 0). Numerical integration of the system is performed using stochastic Heun's method (Manella, 2002), with an integration step size of 0.0122 ms.

4. Validating the simulated brain signals: This is done by comparing the simulated and empirical time series in terms of their amplitude, frequency, and phase.

    a. Amplitude: the range is calculated by identifying the highest and lowest peaks present in the time series across all regions. The overall mean is calculated by averaging the mean amplitude per region across all regions. Mean amplitudes should be similar. An example is shown in **Figure 6.4A.**

    b. Frequency: is computed via Fast fourier transforms of the time series with Matlab's "fft" function with an fs of 0.5 hz to determine the range, profile, and peak frequencies. The maximum frequency for simulated signals should be around 0.25 Hz that coincides with the empirical BOLD responses. An example is shown in **Figure 6.4B.**

    c. Phase: can be done by calculating the pair-wise covariance of the time series for each region for each subject(Ritter et al., 2013a) using the "corr" function in Matlab, which results in a functional connectivity matrix for each subject. In order to smooth the data, one can average all matrices from groups of interest to obtain a group control matrix, and then calculate the pairwise linear correlation coefficient between the simulated functional connectivity matrix for each individual to the group **(Figure 6.5)**. Results from this analysis should reveal similar phases between empirical and simulated signals. Significance of the correlation can be achieved via Fisher Z-transformation.

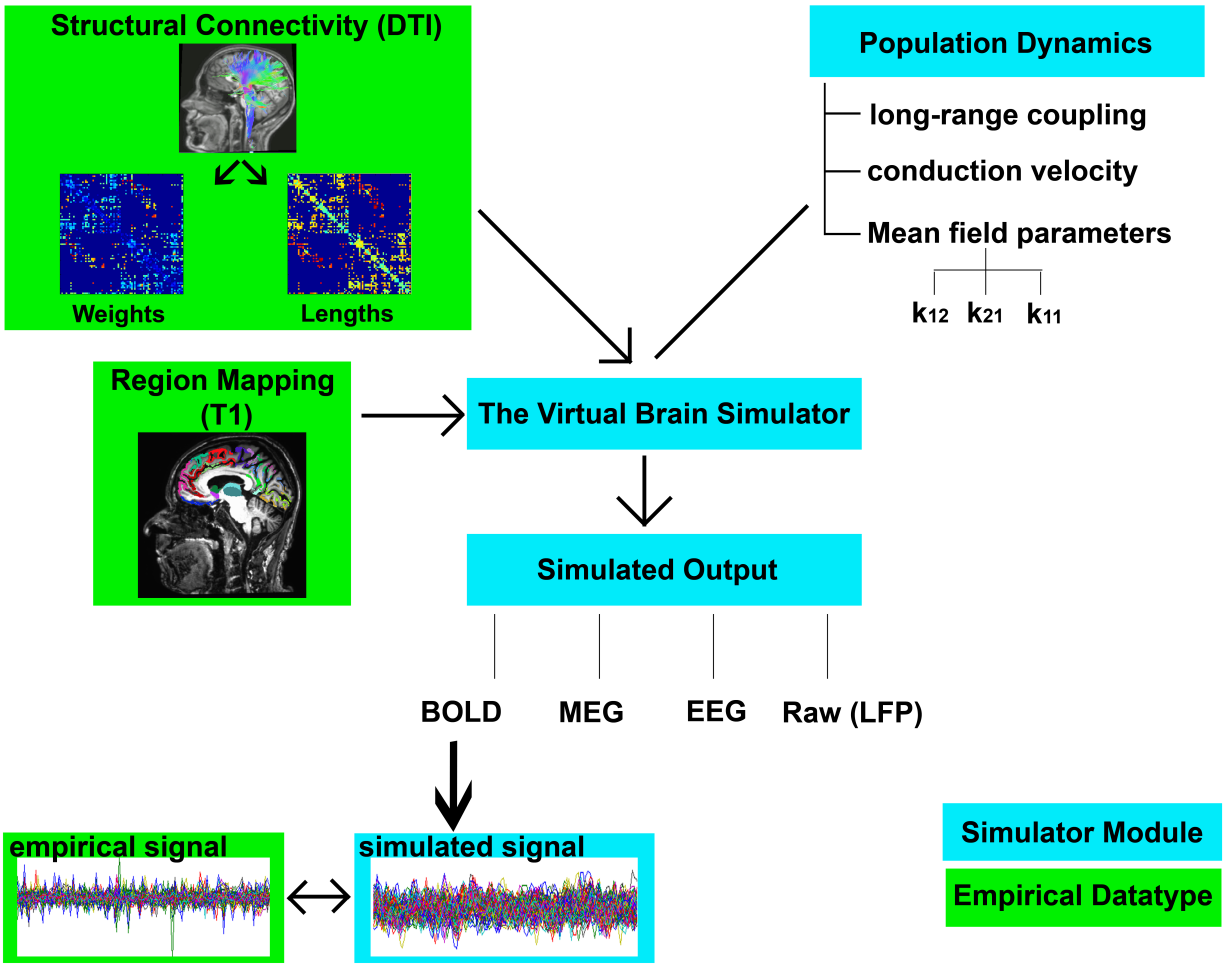

Figure 6.2: Flowchart of TVB Modeling.
Graphic representation depicting the elements involved in TVB modeling. Components shown in green boxes represent empirically collected data. Elements shown in blue boxes represent modeling components within the TVB platform. Empirical input to the TVB consists of 2 structural connectivity matrices (weights and lengths) derived from DTI and a brain parcellation derived from T1-w acquisition. Modeling within TVB includes both global and local parameters resulting in the simulation of biological signals including BOLD. Finally the reliability of the simulation is then compared to the empirical signals.

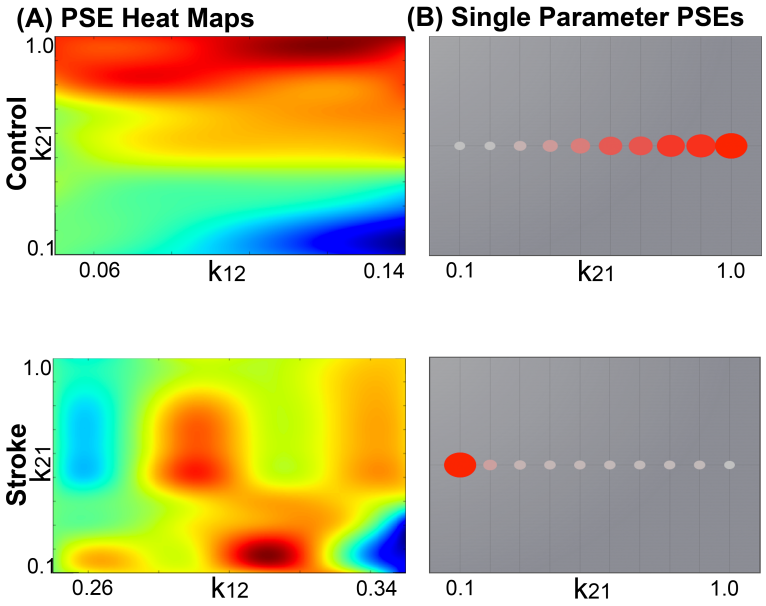

Figure 6.3: Example Global Parameter Space Explorations in Healthy and Stroke Cases.
This figure represents the two viewing options for multiple parameter or single parameter explorations. (A) Parameter explorations of the K_{12} and K_{21} variables (coupling between inhibitory and excitatory populations) in one healthy control (top) and one stroke case (bottom). Heat maps depict the distribution of system variance, with hotter colors indicating values of parameters that yield higher variance. High resolution of heat maps allows for identification of precise parameter values related to high variance. (B) Parameter exploration of the K_{21} variable alone, after optimization has been completed. Colored circles depict degree of variance at each value of K_{21}.

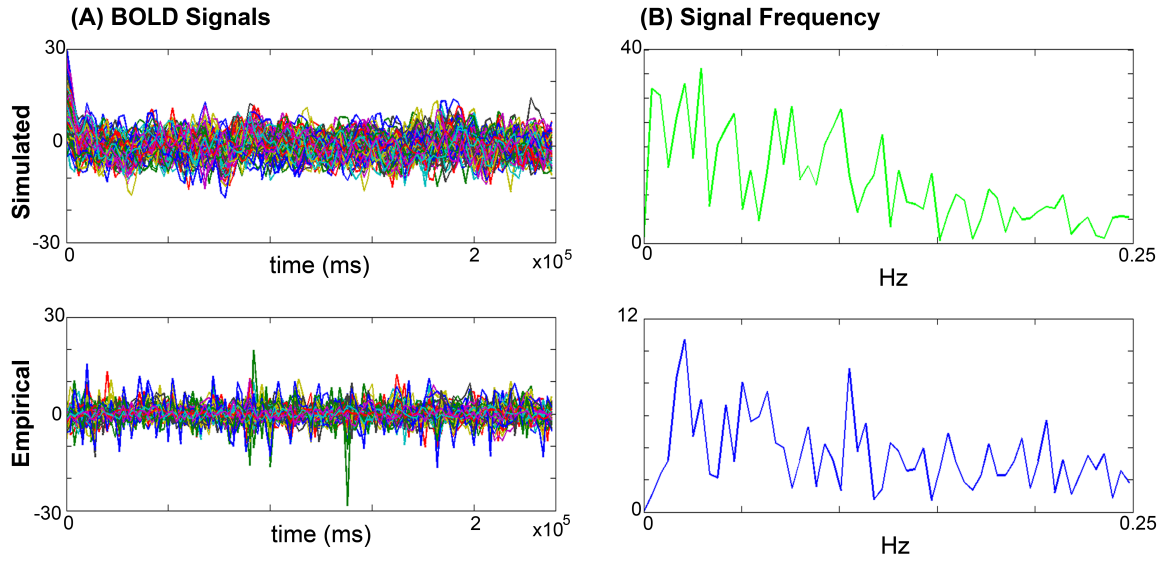

Figure 6.4 Comparisons of Simulated and Empirical Signals: Amplitude and Frequency.
(A) BOLD Time series: Example of a simulated (top) and empirical (bottom) time series. Note the similarity of amplitudes as indicated by the maxima and minima. (B) Frequency: Example frequency distribution graphs for primary motor cortex (M1) of the simulated (top) and empirical (bottom) time series where both signals have similar profiles and peaks.

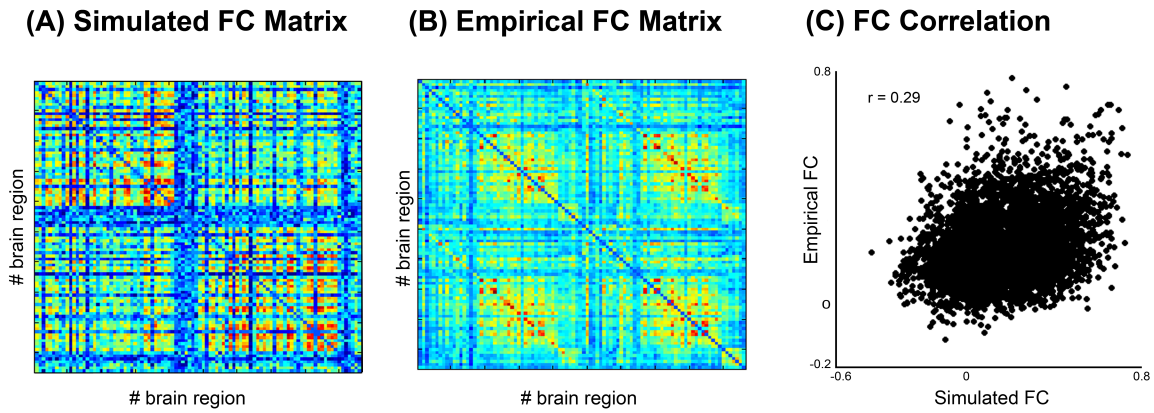

Figure 6.5 Comparison of Simulated and Empirical Signals: Phase.
(A) Functional connectivity matrix from simulated data modeled from one subject. (B) Average functional connectivity matrix from empirical data from all healthy subjects. (C) Correlation of functional connectivity between simulated (x-axis) and empirical (y-axis) time series.

Comparison between Healthy Controls and Stroke

We found an increase in long-range coupling in the stroke group compared to healthy controls. The meaning of long-range coupling is not intuitive, especially when compared to

other parameters more closely linked to biophysical features such as conduction velocity, channel dynamics, or the coupling between excitatory and inhibitory neuronal populations. The long-range coupling function is applied to the activity propagated between brain region regions by the structural pathways before it enters the local dynamic equations of the model. Its primary purpose is to rescale the incoming activity to a level appropriate to model. At a more intuitive level this parameter describes the balance between the global and the local dynamics. In other words, an increase in long-range coupling suggests a preponderance of local over long-range brain dynamics.

In order to put this parameter in the context of current network analytical approaches, in this manuscript we determined the relationship between the modeled long-range coupling in stroke cases with structural network metrics derived from graph analysis including degree centrality, betweenness centrality and global efficiency.

Graph Analysis

Graph Analysis Metrics

Based on the deterministic tractography performed for each individual subject, a binary adjacency matrix A_{ij} was generated whose elements represent the connections (edges) between nodes *i* and *j* (Drakesmith et al., 2015; Shu et al., 2011; Zhang et al., 2015). From these matrices, three measures of functional integration were obtained: average degree centrality, average betweenness centrality, and global efficiency as others have done (Achard and Bullmore, 2007; Betzel et al., 2014; Bullmore and Bassett, 2011), using the NetworkX software (Schult and Swart, 2008) (mathematical notation adapted from (Rubinov and Sporns, 2010)):

1. Average Degree Centrality is the number of nodes adjacent to node *i*, averaged across all nodes in the graph(Bullmore and Sporns, 2009):

$$k_{av} = \frac{1}{n}\sum_{i \in N} k_i = \frac{1}{n}\sum_{i,j \in N} a_{ij}$$

where n is the number of nodes in the graph, and N is the set of those nodes; k_i is the degree centrality for node *i*, and a_{ij} equals 1 when nodes *i* and *j* are nearest neighbors and zero otherwise. This is the simplest measure of centrality, and is commonly used to discriminate between well-connected nodes (hubs) and less well-connected nodes(Bullmore and Bassett, 2011).

2. Average Betweenness Centrality refers to the fraction of shortest paths between any pair of nodes in the network that travel through a given node averaged across all nodes (Sporns et al., 2007):

$$b_{av} = \frac{1}{n}\sum_{i \in N} b_i = \frac{1}{n}\sum_{i \in N} \frac{2}{(n-1)(n-2)} \sum_{\substack{h,j \in N \\ h \neq j, h \neq i, j \neq i}} \frac{p_{hj}(i)}{p_{hj}}$$

where b_i is the betweenness centrality for node i; p_{hj} is the number of shortest paths between nodes h and j, and $p_{hj}(i)$ is the number of shortest paths between *h* and *j* that pass through node *i*. This is the oldest and most commonly used measure of centrality(Bullmore and Bassett, 2011) where "shortest" refers to the path between two nodes that contains the least number of intermediate nodes.

3. Global Efficiency is the average of the inverse of the shortest path length between all nodes (minimum number of edges traversed to connect one node to another)(Bullmore and Sporns, 2009; Crossley et al., 2014):

$$E = \frac{1}{n}\sum_{i \in N} E_i = \frac{1}{n}\sum_{i \in N} \frac{\sum_{i \in N, j \neq i} d_{ij}^{-1}}{n-1}$$

where d_{ij}^{-1} is the inverse of the shortest path length between nodes *i* and *j*. For binary matrices, a network where each node has a direct connection to all other nodes in the graph has maximal global efficiency, equal to 1, while a partially disconnected network has lower global efficiency (Achard and Bullmore, 2007).

Comparison of graph analysis metrics between groups

To test for differences in degree centrality, betweenness centrality, and global efficiency between healthy and stroke cases, we used the Wilcoxon-rank sum test. Significance threshold was set to p= 0.017 (Bonferroni correction). A simple linear regression analysis was used to correlate TVB long-range coupling (independent variable) with graph analysis metrics (dependent variables).

D. Results

Comparison of Graph Analysis Metrics between stroke cases and healthy controls

Results from the Wilcoxon rank sum test showed no significant differences between healthy controls and stroke cases in degree centrality (p= 0.11), betweenness centrality (p=0.86), or global efficiency (p=0.0822). However, the distributions of each graph analysis metric between the two groups showed differences (**Figure 6.6**). Specifically, global efficiency showed a trend towards lower values in stroke cases compared to controls (p = 0.04), but not degree centrality (p = 0.22) nor betweeness centrality (p = 0.95). While there was not a statistical difference in distribution of degree centrality between healthy and stroke populations, a large amount of subjects showed lower values of degree centrality.

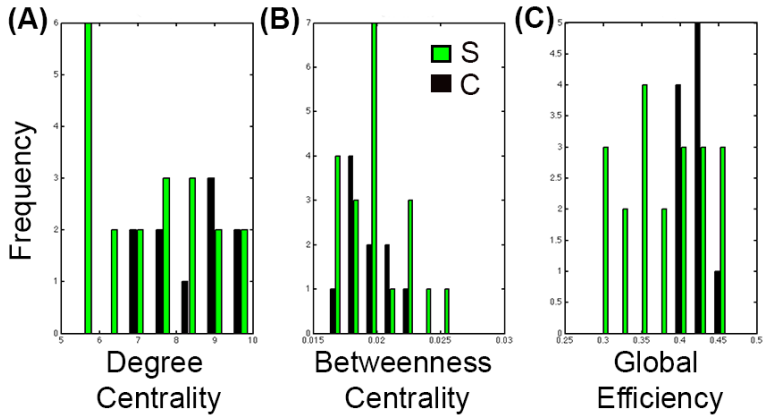

Figure 6.6 Distributions of Graph Analysis Metrics in Control and Stroke Cases.
Distribution graphs comparing the control (black) and stroke (green) cases for (A) degree centrality, (B) betweenness centrality, and (C) global efficiency. Note that distributions in stroke shift to the left for global efficiency but not for degree centrality nor for betweenness centrality.

Correlation between Long-range Coupling and Graph Analysis Metrics

Linear regression analysis showed that the only graph analysis metric associated with the TVB long-range coupling parameter was global efficiency **(Figure 6.7)**. That is, higher values of global coupling were correlated with lower values of global efficiency (t=-2.19, p=0.038). There was no significant correlation between global coupling and degree centrality (p=0.7) or betweenness centrality (p=0.6).

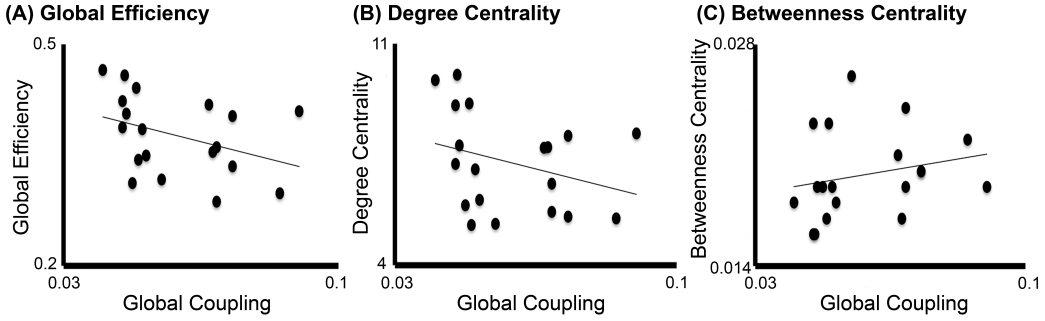

Figure 6.7 Correlation between Global Coupling and Graph Analysis Metrics.
Correlation graphs between global coupling (x-axes) and graph analysis metrics (y-axes): (A) global efficiency (B) degree centrality (C) betweenness centrality. Only global efficiency correlated significantly with long-range coupling (p=0.038), but not degree centrality (p=0.7) or betweenness centrality (p=0.6).

E. Discussion

We have demonstrated that TVB can be a novel tool for identifying biophysical biomarkers of stroke recovery, showing that 1) the parameters associated with TVB modeling directly link structural imaging data to biophysical processes associated with brain dynamics; 2) the models are individualized, as they are based on the specific structural connectome from each person; and 3) TVB parameters can be correlated with other metrics not currently associated with biological parameters (i.e. graph analysis metrics). Importantly, this study harnessed the relationship between TVB and graph analysis, wherein the latter supplies an additional description of changes in relationships between different brain regions, while TVB supplies the neurobiological mechanisms responsible for them. The here outlined steps using TVB offer a unique method, providing a new dimension to the study of stroke.

TVB integrates macroscopic and mesoscopic levels to predict brain dynamics

There is currently no way to directly measure the local parameters modeled in TVB in humans. Whereas global measures derived from imaging data have been used as potential biomarkers of stroke recovery (Burke and Cramer, 2013; Milot and Cramer, 2008), the parameters considered within TVB at the local level represent a dimension reduction derived from processes at the cellular or even molecular levels. That is, the mesocopic level represents the transitional state between the macro and micro-scales(Mitra, 2014). Thus these parameters better inform us of underlying brain mechanism responsible for brain dynamics that current imaging analyses are unable to access, such as dynamics between excitatory and inhibitory neuronal populations and ion channel properties. In this way, TVB can assist to generate

hypothesis associated with basic mechanisms that are responsible for the changes in brain dynamics associated with stroke.

In this context is important to mention that TVB can have wide applicability in the clinical setting because the input required for its operation can be minimal. In ideal circumstances, the experimental data needed are T1w, fMRI (or EEG, MEG) and DTI. However, some of these categories may not be necessary when only physiological data are available (e.g. EEG) without anatomical or connectivity data. In these cases, TVB platform includes normalized anatomical data (a parcellated cortical surface based on the MNI atlas) and a theoretical structural connectome based on the CocoMac database (Jirsa et al., 2010; Kötter, 2004). For stroke cases, while it is preferable to have anatomical data, it is still possible to run accurate simulations by manually modifying this provided structural connectome to exemplify the individual lesions.

The resulting TVB models are individualized

There is large consensus on the importance of individualized medicine as one of the means to improve medical care. In this sense, a central feature of TVB is its direct focus on individual subjects' brain dynamics. The structural connectivity matrix of each individual drives the modeling producing the individualized simulated brain activity whereas the applicability of previous studies have been at the group level (Mueller et al., 2013b). By generating reliable simulations the system provides a window into the state of biophysical parameters associated with it in each person and hence enables the development of customized, individualized therapies and treatments.

There are a myriad of stroke therapies currently under investigation, including constraint-induced motor therapy (Kitago et al., 2013b; Wolf, Steven L, Winstein,Carolee J., Miller, J. Phillip, Thompson, Paul A., Taub, Edward, Uswatte, Gitendra, Morris, David, Blanton, Sarah, Nichols-Larsen, 2008; Wolf et al., 2006), action observation therapy (Ertelt et al., 2007; Small et al., 2013b), neurostimulation (e.g., transcranial magnetic stimulation, transcranial direct-current stimulation) (Agosta et al., 2014; de Aguiar et al., 2014), robotic therapy (Rosati et al., 2011; Taheri et al., 2012), and cellular based (e.g. stem cell) therapies (Tang et al., 2015), that have shown limited degrees of effectiveness, due perhaps to the fact that they are not specifically targeting brain mechanisms responsible for individual dysfunction. This is a reflection of the paucity in our understanding of basic mechanisms generating individual brain dynamics. Having new hypotheses applicable to each patient will enable us to generate new therapeutic interventions that specifically target the elements producing particular brain states. Furthermore, the more we learn about basic processes based on animal studies for instance, the more we can modify current TVB local models and hence, obtain more sophisticated simulations.

TVB parameters can be related to other network metrics

An additional feature of parameters derived from TVB is that they can be contrasted with other measures. Our results showed a trend towards decreased global efficiency in stroke that measures the network's capacity for communication, with greater efficiency indicating better overall communication (Achard and Bullmore, 2007; Rubinov and Sporns, 2010). In other words, network communication is impaired after stroke. Interestingly, degree centrality and

betweeness centrality after stroke were not different from healthy controls probably due to the large variance of stroke size.

The negative correlation between global efficiency and the modeled long-range coupling provides unique insight into the network structure of the brain following stroke. We have previously observed increased long-range coupling after stroke, intuitively indicating a higher influence of local dynamics on brain activity than long-range dynamics. In this context it is important to remember that the global model is derived from the structural connections between nodes and hence one would expect that shorter (direct) paths that originate from damaged nodes should be compromised. The graph analysis results suggest that the post-stroke connectivity between nodes is done through less efficient, longer paths (Rubinov and Sporns, 2010). Therefore, decreased global efficiency and increased long-range coupling after stroke suggest a breakdown in the ability to transfer information between regions, weighting the activity towards local dynamics. Our findings therefore highlight the global impact of stroke, despite its relatively focal damage. This novel finding in stroke is consistent with studies in other neurological diseases such as schizophrenia where imbalances between local and global dynamics, specifically a breakdown of local structure and a shift towards global dynamics has been suggested (van den Berg et al., 2012).

Limitations

TVB as any modeling approach is laden with limitations. Among them:

1. The fact that TVB simulations depend on structural connectivity assumes the structural matrices having reasonable reliability. This is very relevant in stroke because the damage can produce mechanical distortions of tissue. In our case we have used the Virtual Brain

Transplant to minimize these issues. Additionally, there are many definitions of "weights" of connections (Hagmann et al., 2008; Lohse et al., 2014) although novel approaches promise at least high intra-individual reliability in the reconstruction (Besson et al., 2014). In our case, we used a surrogate measure reflecting the "number of fibers per pathway". This is the reason why we normalized the number of streamlines between nodes by the FA of the particular pathway.

2. The weights of connections are currently based on the size (number of streamlines) of the pathways, yet the particular features of the synaptic connections are not taken into consideration. For example, the penetrance of a smaller pathway could be larger than a bigger pathway if the former establishes the synaptic contact with more proximal versus distal dendrites. This type of information is available for other species but is not yet known in humans.

Future Directions and Clinical Impact

The ability of generating a Virtual Brain from any individual opens up an interesting venue for therapeutics. Once a hypothesis is derived from the biophysical parameters affected by the stroke, the effects on brain dynamics can be tested within the TVB platform by modifying the parameters for an individual case. In this way, TVB can be used as a test for potential therapeutic interventions before they are tested in animal models or individual patients.

TVB thus has the potential to revolutionize stroke treatment in the future, by allowing for:

1. The application to "big data". While the current study used a smaller sample size, once we have parameter changes, future studies can more readily utilize TVB in a large number of patients.

2. The ability to study longitudinal brain changes in stroke, from acute and sub-acute to chronic stroke. Because of the predictive potential of TVB, the inclusion of patients at early stages can provide the identification of powerful biomarkers for recovery.
3. The individualization of treatment with minimal input: one single MRI scan including the anatomical scan, DTI, and resting state fMRI.
4. The ability to perform whole brain modeling, integrating the particular intercommunication between nodes (DTI-derived) to local biophysical models associated with concrete basic functional parameters.
5. The opportunity to identify tangible targets for treatment that are testable within the application itself.
6. An Open source platform: It is possible to add new, more sophisticated mesoscopic and microscopic models via the open source nature of TVB. Therefore new developments on basic physiological knowledge can be easily integrated in the future.
7. Allowing the simulation of resting state brain activity, as was done in this study, but also of evoked responses through a built-in feature that allows for stimulation of brain areas, with features determined by the modeler.

CHAPTER 7

A New Neuroinformatics Approach to Precision Medicine in Neurology: The Virtual Brain

A. Introduction

An ongoing effort to achieve personalized data-driven approaches to treatment has heralded the emergence of Precision Medicine (for a full review see Duffy 2015). Under Precision Medicine, patients are not stratified by disease or disease sub-type, but modeled and treated as individual cases using a plethora of information: genomic, epigenetic, environmental, lifestyle and medical history. The ultimate goal is to develop computational models that integrate data and knowledge from both the clinic and basic research to gain a mechanistic understanding of disease, in turn enabling personalized treatment (Duffy, 2015; Wolkenhauer et al., 2014). These models encompass multiple scales of biological organization, from the molecular and cellular levels to the tissue, organ and entire organism models, and aim to predict mechanisms of disease and responses to treatment (Wolkenhauer et al., 2014). This type of individualized treatment is especially valuable to the treatment of neurological disease, where the high variability among patients in response to any given treatment necessitates the need for specialized treatment protocols (Hamburg and Collins, 2010; Jung and Lee, 2015; Matthews et al., 2014).

The road to achieving Personalized Medicine has been defined by two driving components: 1) the collection of “big data”, and 2) neuroinformatics and network methods to process and interpret “big data”. The term “big data” refers to datasets that include the generation of large amounts of multi-modal imaging data (raw, pre-processed, and

intermediate data) for a high number of subjects (Poldrack and Gorgolewski, 2014). There has been a recent push to collect these datasets, as evidenced by such initiatives as the Human Connectome Project (Sotiropoulos et al., 2013), CONNECT (Assaf et al., 2013), Brain connectome (Jiang, 2013), the NIH Pediatric Database, and the Alzheimer's Disease Neuroimaging Initiative.

While these data provide the necessary empirical foundation to begin to build a more complete picture of each individual patient, interpreting these datasets requires the use of extensive neuroinformatics processes involving brain network and connectionist methods of studying brain function (Catani and ffytche, 2005; Deco and Kringelbach, 2014; Hartman et al., 2011; McIntosh, 2000). The theory behind these methods it that a greater understanding of individual variability in brain disease is facilitated by viewing brain anatomy and function from a distributed network perspective, where the brain can be thought of as a complex network composed of different nodes linked by connections (Bullmore and Sporns, 2009; Hartman et al., 2011; Sporns et al., 2004). These connections may refer to the anatomical links between individual neurons, or the fiber pathways between neuronal populations or anatomically segregated brain regions (Cabral et al., 2014). Through such connections, information is shared between neurons and between brain regions (McIntosh, 2000). A perturbation to the system in a specific brain region will thus have a distributed network effect by conveying changes to remote parts of the brain.

In constructing a brain network model, the structural pathways connecting brain regions can be inferred by detecting white matter tracts using diffusion weighted imaging, and the functional connections between brain regions can be inferred by calculating temporal

correlations between neural activity measures (functional MRI, EEG, PET) (Betzel et al., 2014; Cabral et al., 2013, 2014). Some recent imaging studies have provided evidence that damage to specific brain regions results in disturbance of a network via changes to regions and the connections among them, suggesting that some of the observed variability in symptoms and deficits may be a result of brain network disruption (Breakspear and Jirsa, 2006; Ward, 2003; Ward and Cohen, 2004). Ultimately, applying these imaging methods to neurologic disease allows for investigation into the "potential spread of disease along connections in brain networks" (Verstraete and Foerster, 2015), and importantly, may allow for the identification of brain measures that correlate with disease.

More recently, the generation of multi-scale brain network models has become a popular new approach. These brain network models are defined as high dimensional systems with significant numbers of parameters governing structure and dynamics (Sanz-Leon et al., 2015b), and help to give a deeper understanding of the underlying physiological mechanisms to brain function in health and disease (Cabral et al., 2012; Horwitz et al., 2013). In this context, The Virtual Brain (TVB) is a novel, bioinformatics platform that models individualized brain activity using empirical structural data (Sanz Leon et al., 2013). Specifically, TVB creates virtual representations of an individual's brain by generating individualized functional neuroimaging data based on the individual's structural connectome data. These personalized brain models contain the connectivity between parts of the brain and the dynamics of local neural populations. TVB uses structural MRI data to create a custom brain surface, diffusion-weighted MRI data to infer anatomical connections between brain areas, and functional MRI data as the target by which the model parameters are modified. The TVB platform offers several models

containing biophysical parameters that produce different empirical brain states (Ritter et al., 2013b). These biophysical parameters exist at the global level, representing biological mechanisms governing dynamics between brain regions, and the local level, describing the properties of small populations of neurons integrating dynamics at the local mesoscopic level. Thus, modeling in TVB involves multiple scales of brain dynamics that are invisible to brain imaging devices and therefore allows the inference of internal states and processes of the brain. TVB has thus far been applied to normative data sets (Deco et al., 2012), learning and plasticity (Roy et al., 2014), and pathological states (Falcon et al. 2016)

Due to its multi-scale modeling approach that allows for the assessment of biological mechanisms that govern brain dynamics on an individual basis, as well as its application to big data, The Virtual Brain is the ideal tool to further the development of Precision Medicine. The objective of this article is to demonstrate two different cases that successfully utilized The Virtual Brain as a potential biomarker.

B. Modeling with TVB

Large-scale brain network models in general, and TVB brain model in particular, have three critical components, network connectivity, neural mass model and MRI lesions. First, procedures to reconstruct connectivity from DTI data nowadays reliably extract structural network connectivity with high anatomical precision and efforts are on the way to develop more advanced methods proving robust and reproducible on subject and group levels (Besson et al., 2014). Thus there is hope that patient specific connectomes may soon enter in clinical routine use. Second, neural mass models are placed at the network nodes (brain regions) and determine the dynamic nature of the interactions. Third, neural mass models need not

necessarily to be derived from biophysical mechanisms, but rather need to capture the dynamic repertoire of the neural population. It is in this dynamical sense that they have to be biophysically realistic, not in the traditional bottom-up causal sense.

In summary, TVB uses empirical neuroimaging data to create dynamic models of the human brain. The models contain the complete connectivity between parts of the brain and the dynamics of local neural populations. TVB uses structural MRI data to create the custom brain surface, diffusion-weighted MRI data to infer the anatomical connections between brain areas, and then functional MRI data as target to modify the parameters of the model to reproduce the observed functional data. The neuroinformatics architecture houses a library of models, which catalogues the biophysical parameters that produce different empirical brain states (Ritter et al., 2013a; Sanz Leon et al., 2013). These biophysical parameters are invisible to brain imaging devices, thus TVB acts as a "computational microscope" that allows the inference of internal states and processes of the system.

In the practical sense, and in order to reconstruct the anatomical connectivity on each patient, we acquire the following MRI sequences: High-resolution T1w anatomical images and Diffusion Tensor Imaging. The anatomical T1w acquisition will guide on the reconstruction of the patient's individual brain network topography and connection topology in a 3D physical space.

As we are reproducing (simulating) functional data, in order to assess the model we also acquire resting state functional MRI (rsfMRI) for 5 min in the stroke patients to create functional connectivity matrices calculating the pair-wise covariance of the time series from each brain region (Ritter et al., 2013b).

C. Clinical Applications of TVB modeling

The software platform for TVB has already been established and applied to normative data sets (Deco & Jirsa, 2012) for learning and plasticity (Roy et al. 2014) and we have begun assessments in epilepsy (Jirsa) and stroke (Solodkin). These two last topics will be described below.

C.1. EPILEPSY

Objective: Structural anomalies such as hamartoma, pachygyria, etc. (as observed for in the MRI) can be identified. EEG recording further informs the clinician on the evolution of the epileptic seizure and allows the formulation of first hypotheses of the location of the Epileptogenic Zone (EZ), defined as the hypothetical area in the brain responsible for the origin and early organization of the epileptic activity (Talairach & Bancaud, 1966). The Propagation Zone (PZ) comprises areas that are recruited during the seizure evolution, but are by themselves not epileptogenic. Hence, based on structural anomalies and the first assessment on EZ, estimation of TVB Parameters (epileptogenicity, anomalies) are set in the network model to predict the propagation pattern of seizures in order to explore brain intervention strategies.

TVB Modeling: In epilepsy, the Epileptor is a neural mass model that has been derived purely based on mathematical reasoning. It provides a complete taxonomy of epileptic seizures including onset, offset and seizure evolution characteristics. Once a seizure type has been determined for a particular patient, then the taxonomy (Jirsa et al., 2014) offers a mathematical formulation of a generative model that can be used as a network node in the VEP model. Integration of MRI lesions into the VEP model is possible, but not evident due to the challenge

in translating the lesion into model parameters. Reasonable candidates are excitability and local connectivity, because localized tissue abnormalities are likely to alter these two parameters in the context of our network perspective. MRI lesions provide a spatial map of altered parameters that thus enter into the VEP model and affect the network dynamics. The emergent dynamic effects, the seizures in the current context, will crucially depend on the interplay between network node model (Epileptor), patient specific structural connectivity (from DTI), and spatial maps of excitability (EZ, PZ) and MRI lesions.

Conclusions:

Despite the heavy sequelae from medically refractory epilepsy, there is a potentially curative procedure - surgical resection of the EZ (Najm et al 2006; Rosenow et al 2001). However, to be effective, this procedure depends on correct identification of the EZ, which is often unclear (Bulacio et al 2012). A comprehensive pre-surgical evaluation is necessary to pinpoint the EZ as well as to identify the risks of neurologic morbidity such as visual or speech impairment (Wiley et al. 1988; Jayakar et al. 1994; Adelson et al. 1995; Jayakar 1999). Various non-invasive and invasive methods are used. Non-invasive techniques include scalp EEG and video-EEG monitoring, neuropsychological tests, speech-language studies, and brain imaging (MRI, PET, Ictal SPECT). Of these methods, to this date the highest predictor of surgical success is identification of a single visible MRI lesion (Bulacio et al 2012; Jeha et al. 2007; Lopez-Gonzalez et al. 2012). In patients with non-lesional MRI, localization and surgical success in seizure control are even more challenging (Jeha et al. 2007). Despite the advances in imaging technologies, a significant number of surgical patients with focal epilepsy (~25%) continue to

have non-lesional MRIs (Jeha et al. 2007; Widdess-Walsh et al. 2007) and calls for novel approaches.

Jirsa et al (2016) propose such a novel approach to brain interventions based on large-scale brain network based models that are derived from non-invasive structural data of individual patients. The Virtual Epileptic Patient (VEP) model provides the perfect test bed for clinical hypothesis testing of questions linked to network-based mechanisms. Questions outside of this framework will be more difficult or impossible to address by our top-down approach and are the focus of other efforts (Markram et al., 2015) emphasizing the bottom-up approach. The latter approaches are a promising avenue for the future, our top-down approach is feasible today.

C.2. STROKE

In previous studies (Falcon et al 2016; accepted), we found a consistent pattern of TVB parameter changes associated with long-term motor recovery. These included a hyper-excitable state at the local level, a trend towards lower conduction velocities in cortico-cortical connectivity and an imbalance between local and global dynamics favoring the former. Here we hypothesize that the reestablishment of parameter values in our TVB modeling in individual patients, will produce brain dynamics with a closer resemblance to the dynamics in healthy controls. That is, we suggest the possibility of reestablishing healthier brain dynamics even when the primary damage remains (Virtual Therapy).

TVB modeling: In stroke, the Stefanescu Jirsa 3-D model (SJ3D) is also a neural mass model based on biophysical parameters describing interactions within a population of neurons, including coupling between and within excitatory and inhibitory populations, resting neuronal

membrane potential, membrane excitability, and behavior of ion channels. The SJ3D Model within The Virtual Brain (TVB version 1.08) is used for all simulations (Sanz Leon et al., 2013, Sanz Leon et al 2015) that has several sequential steps as reported previously (Falcon et al., 2015). Here, we report the steps to evaluate The Virtual Therapy, where we test if parameter restoration to healthy control values re-establishes brain dynamics in stroke cases.

The following steps were performed:

1) The correlation between the average control functional connectivity matrix and the matrices with each stroke subject was calculated as baseline value.
2) Virtual Therapy: Parameters that changed after stroke were adjusted on each patient to mimic those in the average control value (i.e. global coupling, conduction velocity, coupling between inhibitory and excitatory local populations).
3) Brain signals were re-simulated with the modified parameter values and the consequent functional connectivity matrices were generated.
4) The correlation with the healthy control average functional connectivity was re-calculated post Virtual therapy.
5) The change in correlation was calculated by subtracting the original correlation with healthy controls to the post-adjustment correlation. We also calculated % change from baseline (pre- Virtual Therapy) correlation using the following algorithm: (Post-Virtual Therapy correlation – Pre- Virtual Therapy correlation)/(Pre- Virtual Therapy correlation) * 100

`Of the 20 stroke subjects included, 17 saw increased correlation of resting state functional connectivity with the healthy control average (seen as a positive change in correlation) after modifying a subset of the parameters (**Figure 7.1**). Apart from the 3 subjects who saw 0% change, the range of % change for the remaining subjects was 5-85.7%. Of all combinations of parameter modifications attempted, the majority of subjects saw the most improvement when the combination of global coupling and k12 was modified, that is when the balance between global and local dynamics and the excessive excitation are restored. These results are of relevance as our previous results showed that these parameters were correlated with long-term motor recovery (Falcon et al 2016; accepted).

Furthermore for all subjects, the parameter, "global coupling", was the one with the larger influence as it was present in the parameter combination that resulted in the largest increase in correlation with healthy controls. The biological significance of this parameter is not intuitive and warrants further exploration. However, our previous work (Falcon et al., 2015) has shown in the context of graph analysis, that it is negatively correlated with global efficiency, or a network's capacity for communication (Bullmore and Sporns, 2009). Although a correlation was found, unfortunately it does not provide an interpretation in precise biological terms. Our current efforts are now focusing on possible biophysical factors that could provide neurobiological grounding to this elusive parameter but others, such as Yang et al (Yang et al., 2014) have suggested that it is associated with an overall change in connection strengths perhaps associated with the regulation of local feedback inhibition (Deco et al., 2014).

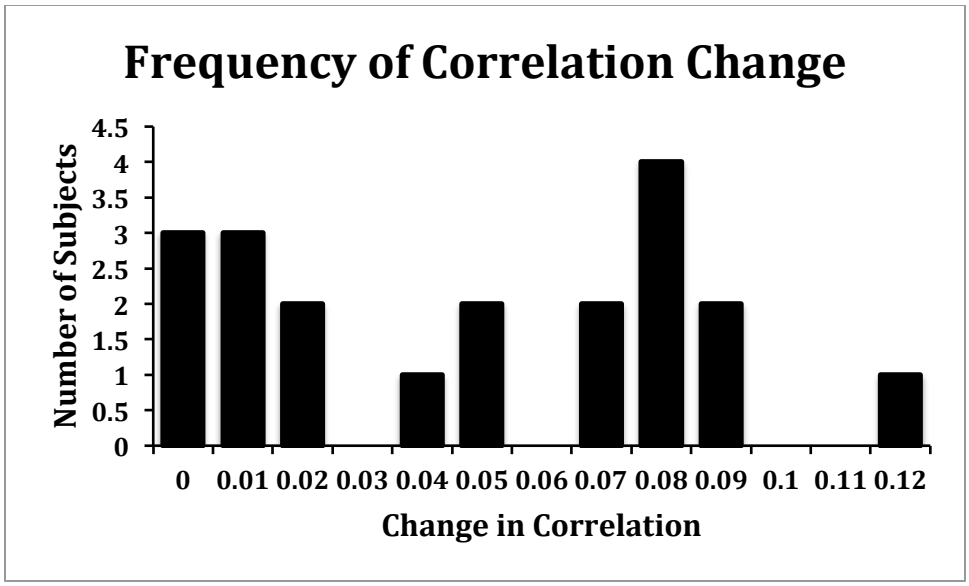

Figure 7.1 Frequency of change in correlation of rsFC with healthy controls. Correlations with healthy controls increased with a range of 0.01-0.12. Three subjects showed no change in correlation. No subjects showed a decrease in correlation with healthy controls (negative change).

D. General Summary

We have described two cases involving two different neurological diseases in which The Virtual Brain can be used as a potential biomarker of disease. In this context, a biomarker is a surrogate clinical measure that ideally reflects underlying biological processes on the cellular/molecular level that can be used as an indicator of disease state (Burke 2014). The defining feature of a biomarker is that it is consistently reliable for each individual, allowing it to be used to diagnose disease, monitor disease progression, and predict patient response to treatment (Berger & Reindl 2015, Agrawal and Biswas 2015). Because of their utility in medical practice and the fact that they represent a critical step towards achieving Precision Medicine, researchers are actively seeking biomarkers of brain injury as a means to personalize treatment and track individual recovery. Currently, there is a paucity of biomarkers associated with

neurological disease as most approaches use correlative outcomes rather than biomarkers. For instance some reports show brain activity related to progressive damage or recovery (Burke & Cramer 2015) have prove to be sensitive, specific, minimally invasive, and relatively easy and inexpensive to measure (Harris & Sadiq 2014, Agrawal and Biswas 2015). However, they lack a direct relation to underlying processes. Therefore, the degree to which they can assist with prognosis and treatment is limited. In contrast, our multiscale approach has the potential to identify biomarkers as they provide a direct link to the underlying physiology highlighting targets for treatment.

An important clinical application of The Virtual Brain is that the model of an individual patient's brain can act as an indicator of pathogenic processes and pharmacologic responses to therapeutic intervention (Group, 2001). That is, using The Virtual Brain, complex brain dynamics are generated by a data-constrained mechanistic model of brain circuit dynamics utilizing physiological parameters. Specific model parameters may then be identified as linked to different disease states, thus the TVB model acts as a compact generator of dynamics-based biomarkers (Falcon et al 2016). Further, the results from these studies show that TVB can then be used to test the reliability of candidate biomarkers by modeling brain dynamics in response to interventions targeting specific parameters correlated with disease.

The Virtual Brain as a biomarker

We first aimed to determine whether modifying parameters associated with stroke that were different from healthy controls for each stroke patient would affect brain activity; that is, if it was possible to test the effect of administering a "Virtual Therapy" on brain dynamics. The modified parameters were identified previously as being significantly related to stroke (Falcon

et al 2016) and included global parameters: long-range coupling and conduction velocity, and local parameters: excitatory-on-inhibitory coupling and inhibitory-on-excitatory coupling. Interestingly, while the majority of subjects did show an improvement in correlation of resting state functional connectivity with healthy controls, a closer investigation showed that each subject responded better to a unique combination of these parameters, rather than all subjects responding optimally to the same parameter modification combination. This highlights the sensitivity of TVB modeling to detect global level differences based on individual parameters between subjects.

One limitation in the development and implementation of viable individualized treatments is the inability to directly assess efficacy of different treatments (Matthews et al 2014). Through this study, we are able to assess efficacy of different "virtual treatments" on brain dynamics.

At the risk of overselling, we believe that our project provides the basis for a more deliberate integration of computational neuroscience into clinical approaches for diagnosis and treatment of brain disorders. The technological advances in biomedical imaging yield unprecedented information on the brain structure and function, yet such data are severely under-utilized for clinical decision support. The application of secondary prevention is obvious, where computational model based on a patient's own data can help constrain diagnoses and the choices of individualized therapeutic interventions. There is, we believe, an even more exciting potential application in primary, and perhaps tertiary prevention, wherein the combination of informatics approaches on big data and computational models of early

detection can help the individual monitor their own brain health and introduce effective mitigation strategies in the case of elevated risk of pathology.

CHAPTER 8

Comments on Stroke Findings

The experiments described in the previous chapters aimed to find brain changes related to stroke recovery, utilizing a dataset with longitudinal measures. This dataset was unique in several aspects: whereas many other studies assessing stroke recovery have strict entry criteria, this study allowed even people with severe motor deficits following stroke to participate. Additionally, data was collected at three time points for each subject, the third time point being a maintenance time point that occurred 6-12 months after the completion of therapy, a longer follow-up time point than many other studies assessing stroke recovery.

One conclusion of the initial group level analysis (Chapter 4) was that pre-therapy brain variability predicted long-term functional recovery functional measures at maintenance; that is, more variability led to better recovery. Interestingly, was seen only in the cohort of stroke patients that underwent Action Observation Therapy (AOT), a novel rehabilitation therapy focusing on recovery of fine motor movements. The development of AOT was based on the mirror neuron system, as well as the organization and utility of the tracts comprising the cortico-spinal tract. The findings presented here provide evidence that AOT utilizes and strengthens the remaining brain pathways that were used in motor skills prior to the stroke, rather than relying on new, compensatory pathways that may not be as efficient in motor recovery.

Similar to the previous results in SCA6, the findings from Chapter 4 indicated network level changes that correlate with disease, but are not directly related to the mechanism of stroke or recovery. Therefore, we next asked what biological variables on an individual basis

were responsible for such group level changes. In the subsequent studies, we utilized The Virtual Brain to assess brain changes in individuals across multiple brain scales, as type of analysis has the capacity of providing a true biomarker of disease because, unlike other network analyses, this level of modeling engages the meso- and implicitly, the microscopic level brain mechanisms underlying large-scale network changes (Sanz Leon et al., 2013). Indeed, modeling with The Virtual Brain identified specific parameters as candidate biomarkers; that is, they represent brain processes that correlated with stroke recovery, as seen in Chapter 5. Importantly, one of these parameters, long-range coupling, is non-intuitive, thus the change that occurs in stroke is hard to interpret. Chapter 6 utilized graph theory metrics to further investigate long-range coupling, finding a correlation with how efficient the brain communicates information between regions. Finally, the utility of The Virtual Brain in furthering individualized, or precision medicine, was displayed in Chapter 7, wherein altering the previously identified parameters in stroke cases had a normalizing effect on brain behavior.

Through these latter studies, we have identified a novel modeling method that allows us for the first time to investigate levels in the living human brain that have previously been inaccessible. Additionally, the models that we have created are specific for individuals, allowing us to go beyond group level analyses that, particularly in stroke, suffer from high variability. Finally, the personalization that we were able to achieve in identifying and modifying mechanisms associated with recovery is not limited to stroke, thus making this a promising new method to aid in the identification of biomarkers of any neurologic disease.

SUMMARY AND CONCLUSIONS

The experiments comprising this dissertation explored candidate biomarkers of two contrasting models of neurologic disease using novel network analysis methods. The identification of biomarkers is central to the development of individualized medicine, as these provide the means to develop a prognosis based on a single measurement. While some progress has been made in identifying biomarkers for several neurologic diseases including Alzheimer's Disease (Fiandaca et al., 2014), Parkinson's Disease (Nalls et al., 2015; Scholz et al., 2012) and Huntington's Disease (Rizk-Jackson et al., 2011), many other neurologic diseases, including SCA6 and Ischemic Stroke, are still lacking viable biomarkers.

Both diseases posed different benefits and challenges in this endeavor. Because SCA6 is an autosomal dominant degenerative disorder, precise genetic models can be studied as early as the pre-symptomatic stage. However, its rarity results in typically small sample sizes. On the other hand, while stroke is much more common, it is also highly variable, further complicating the ability to find one measure that can consistently describe patient severity. Attempts to stratify stroke patients based on any number of characteristics have had only limited success (Cramer, 2010). Therefore, for each of these diseases, we employed different approaches to account for these challenges, while maintaining a network approach.

As stated in the Introduction, to qualify as a clinically viable biomarker, a measure should meet the following specifications: they should represent a mechanism at the cellular/molecular level that correlates with disease, and is sensitive enough to accurately reflect disease severity on an individual basis. Further, biomarkers of neurological disease typically fall under one of three categories of sensitivity: a) indirectly correlated with disease; b)

directly correlated with disease; c) directly related to molecular and cellular disease processes. Many current studies approach the search for biomarkers that fall under the second category, where any correlates of disease, regardless of whether they are a direct consequence of disease process, are investigated. These correlates are helpful in gaining information on the range of signs and symptoms of individual patients, rarely are they consistent enough to have clinical use in diagnosis or prognosis.

The work presented here used novel network analyses to identify effects of brain disease that are evident in brain dynamics beyond those directly related to the area of the primary or secondary lesions. Here, I will assess the success of the findings of studies in SCA6 and stroke, based on their adherence to the specified criteria and the level of biomarker under which they fell.

The results found in Chapter 1, which identified early functional and structural changes in SCA6, fall under the second category of biomarker. That is, the found changes are at the network level. Biomarkers at the network level, which might include strength of correlation between two different brain regions, describe a global level result of disease. However, these are typically surrogate measures that still do not provide a direct tie to basic mechanisms (Burke and Cramer, 2013). A future analysis stemming from these results should therefore attempt to identify the underlying physiological mechanisms that might constitute the compensatory changes seen in pre-symptomatic patients.

At the finest level, or the third category of biomarkers, studies at the cellular and molecular level can assess direct mechanisms of disease. While the experiment in Chapter 4 also falls under the network level of analysis, The work in stroke using The Virtual Brain

modeling platform (Chapters 5-7) falls under the mechanistic level of analysis, identifying parameters for each individual subject that represent meso-scopic level mechanisms that are associated with recovery. Manually adjusting these parameters in the model had a corrective effect on the resulting modeled brain activity, thus these parameters may have the potential to be clinically viable biomarkers for stroke recovery. Going forward, these analyses should be applied to a larger population to test the predictive power of these different parameters. Additionally, individual regions associated with the lesion location for a specific patient can be probed, rather than just global changes, to further personalize the modeling process. From these future endeavors, the goal is to create a library of parameters and values associated with stroke in order to optimize the modeling process and make it a more clinically viable method of determining treatment plans.

These studies comprise some of the first forays into a new field of brain analysis, in which on a subject-by-subject basis, multiple scales are explored to bridge the global level connectivity changes associated with neurologic disease with their underlying mechanistic underpinnings. Accordingly, while the mechanisms identified that correlate with stroke are not yet proven to be true biomarkers, they are the first to represent meso- and microscopic level processes in living humans that show consistent changes in a highly variable population. Therefore, the results from these studies hopefully provide evidence that novel network analyses and advances in computational modeling methods can herald a new era of biomarker exploration to pave the way for individualized medicine.

REFERENCES

Abbruzzese, G., Morena, M., Dall'Agata, D., Abbruzzese, M., and Favale, E. (1991). Motor evoked potentials (MEPs) in lacunar syndromes. Electroencephalogr. Clin. Neurophysiol. Potentials Sect. *81*, 202–208.

Abdulkadir, A., Ronneberger, O., Wolf, R.C., Pfleiderer, B., Saft, C., and Klöppel, S. (2013). Functional and structural MRI biomarkers to detect pre-clinical neurodegeneration. Curr. Alzheimer Res. *10*, 125–134.

Abuhassan, K., Coyle, D., Belatreche, A., and Maguire, L. (2014). Compensating for synaptic loss in Alzheimer's disease. J. Comput. Neurosci. *36*, 19–37.

Achard, S., and Bullmore, E. (2007). Efficiency and cost of economical brain functional networks. PLoS Comput. Biol. *3*, e17.

Ackl, N., Ising, M., Schreiber, Y.A., Atiya, M., Sonntag, A., and Auer, D.P. Hippocampal metabolic abnormalities in mild cognitive impairment and Alzheimer's disease. Neurosci. Lett. *384*, 23–28.

Adler, D.E., and Milhorat, T.H. (2002). The tentorial notch: anatomical variation, morphometric analysis, and classification in 100 human autopsy cases. J. Neurosurg. *96*, 1103–1112.

Agosta, S., Herpich, F., Miceli, G., Ferraro, F., and Battelli, L. (2014). Contralesional rTMS relieves visual extinction in chronic stroke. Neuropsychologia *62*, 269–276.

Agrawal, M., and Biswas, A. (2015). Molecular diagnostics of neurodegenerative disorders. Front. Mol. Biosci. *2*.

de Aguiar, V., Paolazzi, C.L., and Miceli, G. (2014). tDCS in post-stroke aphasia: The role of stimulation parameters, behavioral treatment and patient characteristics. Cortex. *63C*, 296–316.

Allen, E.A., Damaraju, E., Plis, S.M., Erhardt, E.B., Eichele, T., and Calhoun, V.D. (2014). Tracking whole-brain connectivity dynamics in the resting state. Cereb. Cortex *24*, 663–676.

Allen, J.S., Damasio, H., and Grabowski, T.J. (2002). Normal neuroanatomical variation

in the human brain: an MRI-volumetric study. Am. J. Phys. Anthropol. *118*, 341–358.

Andersen, K.W., Madsen, K.H., Siebner, H.R., Schmidt, M.N., Mørup, M., and Hansen, L.K. (2014). Non-parametric Bayesian graph models reveal community structure in resting state fMRI. Neuroimage *100*, 301–315.

Arbuckle, J. (1989). AMOS: ANALYSIS OF MOMENT STRUCTURES; SOFTWARE REVIEW. Am. Stat.

Arbuckle, J. (1992). AMOS 3.1 documentation package. Philadelphia Temple Univ.

Armstrong, R.A. (2014). When to use the Bonferroni correction. Ophthalmic Physiol. Opt. *34*, 502–508.

Ashizawa, T., Figueroa, K.P., Perlman, S.L., Gomez, C.M., Wilmot, G.R., Schmahmann, J.D., Ying, S.H., Zesiewicz, T.A., Paulson, H.L., Shakkottai, V.G., et al. (2013). Clinical characteristics of patients with spinocerebellar ataxias 1, 2, 3 and 6 in the US; a prospective observational study. Orphanet J. Rare Dis. *8*, 177.

Assaf, Y., Alexander, D.C., Jones, D.K., Bizzi, A., Behrens, T.E.J., Clark, C. a, Cohen, Y., Dyrby, T.B., Huppi, P.S., Knoesche, T.R., et al. (2013). The CONNECT project: Combining macro- and micro-structure. Neuroimage *80*, 273–282.

Atwood, H.L., and Wojtowicz, J.M. (1999). Silent Synapses in Neural Plasticity: Current Evidence. Learn. Mem. *6*, 542–571.

Avants, B.B., Tustison, N.J., Song, G., Cook, P.A., Klein, A., and Gee, J.C. (2011). A reproducible evaluation of ANTs similarity metric performance in brain image registration. Neuroimage *54*, 2033–2044.

Baldassarre, A., Ramsey, L., Hacker, C.L., Callejas, A., Astafiev, S. V, Metcalf, N. V, Zinn, K., Rengachary, J., Snyder, A.Z., Carter, A.R., et al. (2014). Large-scale changes in network interactions as a physiological signature of spatial neglect. Brain *137*, 3267–3283.

Bartley, A. (1997). Genetic variability of human brain size and cortical gyral patterns. Brain *120*, 257–269.

Beaulieu, C. The basis of anisotropic water diffusion in the nervous system - a technical

review. NMR Biomed. *15*, 435–455.

Beebe, J.A., and Lang, C.E. (2009). Relationships and responsiveness of six upper extremity function tests during the first six months of recovery after stroke. J. Neurol. Phys. Ther. *33*, 96–103.

Behrens, T.E.J., Woolrich, M.W., Jenkinson, M., Johansen-Berg, H., Nunes, R.G., Clare, S., Matthews, P.M., Brady, J.M., and Smith, S.M. (2003). Characterization and propagation of uncertainty in diffusion-weighted MR imaging. Magn. Reson. Med. *50*, 1077–1088.

Bennett, M.R. (1999). The early history of the synapse: from Plato to Sherrington. Brain Res. Bull. *50*, 95–118.

van den Berg, D., Gong, P., Breakspear, M., and van Leeuwen, C. (2012). Fragmentation: loss of global coherence or breakdown of modularity in functional brain architecture? Front. Syst. Neurosci. *6*, 20.

Berger, T., and Reindl, M. (2015). Antibody biomarkers in CNS demyelinating diseases - a long and winding road. Eur. J. Neurol. *22*, 1162–1168.

Berlucchi, G. (2010). Some Aspects of the History of the Law of Dynamic Polarization of the Neuron. From William James to Sherrington, from Cajal and Van Gehuchten to Golgi. J. Hist. Neurosci.

Berlucchi, G., and Buchtel, H.A. (2009). Neuronal plasticity: historical roots and evolution of meaning. Exp. Brain Res. *192*, 307–319.

Besson, P., Lopes, R., Leclerc, X., Derambure, P., and Tyvaert, L. (2014). Intra-subject reliability of the high-resolution whole-brain structural connectome. Neuroimage *102 Pt 2*, 283–293.

Betzel, R.F., Byrge, L., He, Y., Goñi, J., Zuo, X.-N., and Sporns, O. (2014). Changes in structural and functional connectivity among resting-state networks across the human lifespan. Neuroimage *102 Pt 2*, 345–357.

Blicher, J.U., Jakobsen, J., Andersen, G., and Nielsen, J.F. (2009). Cortical excitability in chronic stroke and modulation by training: a TMS study. Neurorehabil. Neural Repair *23*, 486–493.

Bohanna, I., Georgiou-Karistianis, N., Hannan, A.J., and Egan, G.F. (2008). Magnetic resonance imaging as an approach towards identifying neuropathological biomarkers for Huntington's disease. Brain Res. Rev. *58*, 209–225.

Bour, L.J., van Rootselaar, A.F., Koelman, J.H.T.M., and Tijssen, M.A.J. (2008). Oculomotor abnormalities in myoclonic tremor: a comparison with spinocerebellar ataxia type 6. Brain *131*, 2295–2303.

Boynton, G.M., Engel, S.A., Glover, G.H., and Heeger, D.J. (1996). Linear systems analysis of functional magnetic resonance imaging in human V1. J. Neurosci. *16*, 4207–4221.

Breakspear, M., and Jirsa, V.K. (2006). Neuronal Dynamics and Brain Connectivity Introduction : Dynamics and the Brain. 3–64.

Breakspear, M., and Jirsa, V.K. (2007). Neuronal Dynamics and Brain Connectivity. In Handbook of Brain Connectivity, V.K. Jirsa, and A.R. Mcintosh, eds. (Springer), pp. 3–64.

Broca, P. Remarques sur le siège de la faculté du langage articulé, suivies d'une observation d'aphémie (perte de la parole). Bull. La Société D'anatomie *2e serie*, 330–357.

Brodersen, K.H., Schofield, T.M., Leff, A.P., Ong, C.S., Lomakina, E.I., Buhmann, J.M., and Stephan, K.E. (2011). Generative embedding for model-based classification of fMRI data. PLoS Comput. Biol. *7*, e1002079.

Brott, T., Adams Jr., H.P., Olinger, C.P., Marler, J.R., Barsan, W.G., Biller, J., Spilker, J., Holleran, R., Eberle, R., Hertzberg, V., et al. (1989). Measurements of acute cerebral infarction: a clinical examination scale.

Brouillette, A.M., Öz, G., and Gomez, C.M. (2015). Cerebrospinal Fluid Biomarkers in Spinocerebellar Ataxia: A Pilot Study. Dis. Markers *2015*, 413098.

Buccino, G. (2014). Action observation treatment: a novel tool in neurorehabilitation. Philos. Trans. R. Soc. Lond. B. Biol. Sci. *369*, 20130185.

Buccino, G., Vogt, S., Ritzl, A., Fink, G.R., Zilles, K., Freund, H.-J., and Rizzolatti, G. (2004). Neural Circuits Underlying Imitation Learning of Hand Actions. Neuron *42*, 323–

334.

Buccino, G., Gatti, R., Giusti, M.C., Negrotti, A., Rossi, A., Calzetti, S., and Cappa, S.F. (2011). Action observation treatment improves autonomy in daily activities in Parkinson's disease patients: results from a pilot study. Mov. Disord. *26*, 1963–1964.

Buccino, G., Arisi, D., Gough, P., Aprile, D., Ferri, C., Serotti, L., Tiberti, A., and Fazzi, E. (2012). Improving upper limb motor functions through action observation treatment: a pilot study in children with cerebral palsy. Dev. Med. Child Neurol. *54*, 822–828.

Buchkremer-Ratzmann, I., August, M., Hagemann, G., and Witte, O.W. (1996). Electrophysiological transcortical diaschisis after cortical photothrombosis in rat brain. Stroke. *27*, 1105–1109; discussion 1109–1111.

Bullmore, E., and Sporns, O. (2009). Complex brain networks: graph theoretical analysis of structural and functional systems. Nat. Rev. Neurosci. *10*, 186–198.

Bullmore, E.T., and Bassett, D.S. (2011). Brain graphs: graphical models of the human brain connectome. Annu. Rev. Clin. Psychol. *7*, 113–140.

Burke, E., and Cramer, S.C. (2013). Biomarkers and predictors of restorative therapy effects after stroke. Curr. Neurol. Neurosci. Rep. *13*, 329.

Butteriss, D., Chinnery, P., and Birchall, D. (2005). Radiological characterization of spinocerebellar ataxia type 6. Br. J. Radiol. *78*, 694–696.

Buttner, N., Geschwind, D., Jen, J.C., Perlman, S., Pulst, S.M., and Baloh, R.W. (1998). Oculomotor phenotypes in autosomal dominant ataxias. Arch. Neurol. *55*, 1353–1357.

Cabezas, C., and Buño, W. (2011). BDNF is required for the induction of a presynaptic component of the functional conversion of silent synapses. Hippocampus *21*, 374–385.

Cabral, J., Hugues, E., Kringelbach, M.L., and Deco, G. (2012). Modeling the outcome of structural disconnection on resting-state functional connectivity. Neuroimage *62*, 1342–1353.

Cabral, J., Fernandes, H.M., Van Hartevelt, T.J., James, A.C., Kringelbach, M.L., and Deco, G. (2013). Structural connectivity in schizophrenia and its impact on the dynamics of spontaneous functional networks. Chaos *23*, 046111.

Cabral, J., Kringelbach, M.L., and Deco, G. (2014). Exploring the network dynamics underlying brain activity during rest. Prog. Neurobiol. *114*, 102–131.

Carmichael, S.T. (2012). Brain excitability in stroke: the yin and yang of stroke progression. Arch. Neurol. *69*, 161–167.

Carter, A.R., Astafiev, S. V, Lang, C.E., Connor, L.T., Rengachary, J., Strube, M.J., Pope, D.L.W., Shulman, G.L., and Corbetta, M. (2010). Resting interhemispheric functional magnetic resonance imaging connectivity predicts performance after stroke. Ann. Neurol. *67*, 365–375.

Carter, A.R., Shulman, G.L., and Corbetta, M. (2012). Why use a connectivity-based approach to study stroke and recovery of function? Neuroimage *62*, 2271–2280.

Catani, M., and ffytche, D.H. (2005). The rises and falls of disconnection syndromes. Brain *128*, 2224–2239.

Catani, M., and Mesulam, M. (2008). The arcuate fasciculus and the disconnection theme in language and aphasia: history and current state. Cortex. *44*, 953–961.

Catani, M., and Thiebaut de Schotten, M. (2008). A diffusion tensor imaging tractography atlas for virtual in vivo dissections. Cortex. *44*, 1105–1132.

Caveney, E.J., and Cohen, O.J. (2011). Diabetes and Biomarkers. J. Diabetes Sci. Technol. *5*, 192–197.

Celnik, P., Webster, B., Glasser, D.M., and Cohen, L.G. (2008). Effects of action observation on physical training after stroke. Stroke. *39*, 1814–1820.

Christova, P., Anderson, J.H., and Gomez, C.M. (2008). Impaired eye movements in presymptomatic spinocerebellar ataxia type 6. Arch. Neurol. *65*, 530–536.

Cohen, J., MacWhinney, B., Flatt, M., and Provost, J. (1993). PsyScope: An interactive graphic system for designing and controlling experiments in the psychology laboratory using Macintosh computers. Behav. Res. Methods, Instruments, Comput. *25*, 257–271.

Corbetta, D., Sirtori, V., Moja, L., and Gatti, R. (2010). Constraint-induced movement therapy in stroke patients: systematic review and meta-analysis. Eur. J. Phys. Rehabil. Med. *46*, 537–544.

Corbetta, M., Kincade, M.J., Lewis, C., Snyder, A.Z., and Sapir, A. (2005). Neural basis and recovery of spatial attention deficits in spatial neglect. Nat. Neurosci. *8*, 1603–1610.

Coupar, F., Pollock, A., Rowe, P., Weir, C., and Langhorne, P. (2012). Predictors of upper limb recovery after stroke: a systematic review and meta-analysis. Clin. Rehabil. *26*, 291–313.

Coupé, P., Fonov, V.S., Bernard, C., Zandifar, A., Eskildsen, S.F., Helmer, C., Manjón, J. V, Amieva, H., Dartigues, J.-F., Allard, M., et al. (2015). Detection of Alzheimer's disease signature in MR images seven years before conversion to dementia: Toward an early individual prognosis. Hum. Brain Mapp.

Cox, R.W. (1996). AFNI: software for analysis and visualization of functional magnetic resonance neuroimages. Comput. Biomed. Res. *29*, 162–173.

Cox, R.W., and Jesmanowicz, A. (1999). Real-time 3D image registration for functional MRI. Magn. Reson. Med. *42*, 1014–1018.

Cramer, S.C. (2008). Repairing the human brain after stroke: I. Mechanisms of spontaneous recovery. Ann. Neurol. *63*, 272–287.

Cramer, S.C. (2010). Stratifying patients with stroke in trials that target brain repair. Stroke. *41*, S114–S116.

Cramer, S.C., and Riley, J.D. (2008). Neuroplasticity and brain repair after stroke. Curr. Opin. Neurol. *21*, 76–82.

Cricchi, F., Di Lorenzo, C., Grieco, G.S., Rengo, C., Cardinale, A., Racaniello, M., Santorelli, F.M., Nappi, G., Pierelli, F., and Casali, C. (2007). Early-onset progressive ataxia associated with the first CACNA1A mutation identified within the I-II loop. J. Neurol. Sci. *254*, 69–71.

Criscimagna-Hemminger, S.E., Donchin, O., Gazzaniga, M.S., and Shadmehr, R. (2003). Learned dynamics of reaching movements generalize from dominant to nondominant arm. J. Neurophysiol. *89*, 168–176.

Croarkin, E., Danoff, J., and Barnes, C. (2004). Evidence-Based Rating of Upper-Extremity Motor Function Tests Used for People Following a Stroke. Phys. Ther. *84*, 62–74.

Crossley, N.A., Mechelli, A., Scott, J., Carletti, F., Fox, P.T., McGuire, P., and Bullmore, E.T. (2014). The hubs of the human connectome are generally implicated in the anatomy of brain disorders. Brain *137*, 2382–2395.

Dahl, A.E., Askim, T., Stock, R., Langørgen, E., Lydersen, S., and Indredavik, B. (2008). Short- and long-term outcome of constraint-induced movement therapy after stroke: a randomized controlled feasibility trial. Clin. Rehabil. *22*, 436–447.

Dale, A.M., Fischl, B., and Sereno, M.I. (1999). Cortical surface-based analysis. I. Segmentation and surface reconstruction. Neuroimage *9*, 179–194.

Daunizeau, J., David, O., and Stephan, K.E. (2011). Dynamic causal modelling: A critical review of the biophysical and statistical foundations. Neuroimage *58*, 312–322.

Dean, P., Porrill, J., Ekerot, C.-F., and Jörntell, H. (2010). The cerebellar microcircuit as an adaptive filter: experimental and computational evidence. Nat. Rev. Neurosci. *11*, 30–43.

Deco, G., and Kringelbach, M.L. (2014). Great expectations: using whole-brain computational connectomics for understanding neuropsychiatric disorders. Neuron *84*, 892–905.

Deco, G., Jirsa, V.K., Robinson, P.A., Breakspear, M., and Friston, K. (2008). The dynamic brain: from spiking neurons to neural masses and cortical fields. PLoS Comput. Biol. *4*, e1000092.

Deco, G., Senden, M., and Jirsa, V. (2012). How anatomy shapes dynamics: a semi-analytical study of the brain at rest by a simple spin model. Front. Comput. Neurosci. *6*, 68.

Deco, G., Ponce-Alvarez, A., Hagmann, P., Romani, G.L., Mantini, D., and Corbetta, M. (2014). How local excitation-inhibition ratio impacts the whole brain dynamics. J. Neurosci. *34*, 7886–7898.

DeFelipe, J. (2013). Cajal and the discovery of a new artistic world: the neuronal forest. Prog. Brain Res. *203*, 201–220.

Demaerschalk, B.M., Hwang, H.-M., and Leung, G. (2010). US cost burden of ischemic stroke: a systematic literature review. Am. J. Manag. Care *16*, 525–533.

Dennis, E.L., and Thompson, P.M. (2014). Functional brain connectivity using fMRI in aging and Alzheimer's disease. Neuropsychol. Rev. *24*, 49–62.

Destrieux, C., Fischl, B., Dale, A., and Halgren, E. (2010). Automatic parcellation of human cortical gyri and sulci using standard anatomical nomenclature. Neuroimage *53*, 1–15.

Di, X., Rypma, B., and Biswal, B.B. (2014). Correspondence of executive function related functional and anatomical alterations in aging brain. Prog. Neuropsychopharmacol. Biol. Psychiatry *48*, 41–50.

Dick, A.S., Raja Beharelle, A., Solodkin, A., and Small, S.L. (2013). Interhemispheric Functional Connectivity following Prenatal or Perinatal Brain Injury Predicts Receptive Language Outcome. J. Neurosci. *33*, 5612–5625.

Drakesmith, M., Caeyenberghs, K., Dutt, A., Zammit, S., Evans, C.J., Reichenberg, A., Lewis, G., David, A.S., and Jones, D.K. (2015). Schizophrenia-like topological changes in the structural connectome of individuals with subclinical psychotic experiences. Hum. Brain Mapp.

Dronkers, N.F., Plaisant, O., Iba-Zizen, M.T., and Cabanis, E.A. (2007). Paul Broca's historic cases: high resolution MR imaging of the brains of Leborgne and Lelong. Brain *130*, 1432–1441.

Du, X., Wang, J., Zhu, H., Rinaldo, L., Lamar, K.-M., Palmenberg, A.C., Hansel, C., and Gomez, C.M. (2013). Second cistron in CACNA1A gene encodes a transcription factor mediating cerebellar development and SCA6. Cell *154*, 118–133.

Duffy, D.J. (2015). Problems, challenges and promises: perspectives on precision medicine. Brief. Bioinform. bbv060 – .

Duncan, P.W., Wallace, D., Lai, S.M., Johnson, D., Embretson, S., and Laster, L.J. (1999). The stroke impact scale version 2.0. Evaluation of reliability, validity, and sensitivity to change. Stroke. *30*, 2131–2140.

Eccles, J.C., Nicoll, R.A., Taborikova, H., and Willey, T.J. (1975). Medial recticular neurons projecting Rostrally. J Neurophysiol *38*, 531–538.

Edwardson, M.A., Lucas, T.H., Carey, J.R., and Fetz, E.E. (2013). New modalities of

brain stimulation for stroke rehabilitation. Exp. Brain Res. *224*, 335–358.

Emken, J.L., Benitez, R., Sideris, A., Bobrow, J.E., and Reinkensmeyer, D.J. (2007). Motor adaptation as a greedy optimization of error and effort. J. Neurophysiol. *97*, 3997–4006.

Ertelt, D., Small, S., Solodkin, A., Dettmers, C., McNamara, A., Binkofski, F., and Buccino, G. (2007). Action observation has a positive impact on rehabilitation of motor deficits after stroke. Neuroimage *36 Suppl 2*, T164–T173.

Van Essen, D.C. (2004). Surface-based approaches to spatial localization and registration in primate cerebral cortex. Neuroimage *23 Suppl 1*, S97–S107.

Van Essen, D.C. (2005). A Population-Average, Landmark- and Surface-based (PALS) atlas of human cerebral cortex. Neuroimage *28*, 635–662.

Van Essen, D.C., and Dierker, D.L. (2007). Surface-based and probabilistic atlases of primate cerebral cortex. Neuron *56*, 209–225.

Falcon, M.I., Riley, J.D., Jirsa, V., McIntosh, A.R., Shereen, A.D., Chen, E.E., and Solodkin, A. (2015). The Virtual Brain: Modeling Biological Correlates of Recovery after Chronic Stroke. Front. Neurol. *6*, 228.

Ferri, S., Peeters, R., Nelissen, K., Vanduffel, W., Rizzolatti, G., and Orban, G.A. (2015). A human homologue of monkey F5c. Neuroimage *111*, 251–266.

Fiandaca, M.S., Mapstone, M.E., Cheema, A.K., and Federoff, H.J. (2014). The critical need for defining preclinical biomarkers in Alzheimer's disease. Alzheimer's Dement. *10*, S196–S212.

Finger, S., Koehler, P.J., and Jagella, C. (2004). The Monakow concept of diaschisis: origins and perspectives. Arch. Neurol. *61*, 283–288.

Fischer, H.C., Stubblefield, K., Kline, T., Luo, X., Kenyon, R. V, and Kamper, D.G. (2007a). Hand rehabilitation following stroke: a pilot study of assisted finger extension training in a virtual environment. Top Stroke Rehabil. 2007 Jan-Feb;14(1)1-12. *14*, 1–12.

Fischer, H.C., Stubblefield, K., Kline, T., Luo, X., Kenyon, R. V, and Kamper, D.G.

(2007b). Hand rehabilitation following stroke: a pilot study of assisted finger extension training in a virtual environment. Top. Stroke Rehabil. *14*, 1–12.

Fischl, B., Sereno, M.I., Tootell, R.B., and Dale, A.M. (1999a). High-resolution intersubject averaging and a coordinate system for the cortical surface. Hum. Brain Mapp. *8*, 272–284.

Fischl, B., Sereno, M.I., and Dale, A.M. (1999b). Cortical surface-based analysis. II: Inflation, flattening, and a surface-based coordinate system. Neuroimage *9*, 195–207.

Folstein, M.F., Folstein, S.E., and McHugh, P.R. (1975). “Mini-mental state”. A practical method for grading the cognitive state of patients for the clinician. J. Psychiatr. Res. *12*, 189–198.

Forman, S., and Cohen, J. (1995). Improved assessment of significant activation in functional magnetic resonance imaging (fMRI): use of a cluster-size threshold. … Reson. ….

Fornito, A., Zalesky, A., and Breakspear, M. (2015). The connectomics of brain disorders. Nat. Rev. Neurosci. *16*, 159–172.

Fox, M.D., and Raichle, M.E. (2007). Spontaneous fluctuations in brain activity observed with functional magnetic resonance imaging. Nat. Rev. Neurosci. *8*, 700–711.

Franceschini, M., Ceravolo, M.G., Agosti, M., Cavallini, P., Bonassi, S., Dall’Armi, V., Massucci, M., Schifini, F., and Sale, P. (2012). Clinical relevance of action observation in upper-limb stroke rehabilitation: a possible role in recovery of functional dexterity. A randomized clinical trial. Neurorehabil. Neural Repair *26*, 456–462.

Frick, A., Åhs, F., Engman, J., Jonasson, M., Alaie, I., Björkstrand, J., Frans, Ö., Faria, V., Linnman, C., Appel, L., et al. (2015). Serotonin Synthesis and Reuptake in Social Anxiety Disorder. JAMA Psychiatry *72*, 794.

Fridriksson, J., Holland, A.L., Coull, B.M., Plante, E., Trouard, T.P., and Beeson, P. (2002). Aphasia severity: Association with cerebral perfusion and diffusion. Aphasiology *16*, 859–871.

Friedman, N., Chan, V., Reinkensmeyer, A.N., Beroukhim, A., Zambrano, G., Bachman, M., and Reinkensmeyer, D.J. (2014). Retraining and assessing hand movement after

stroke using the MusicGlove: Comparison with conventional hand therapy and isometric grip training. J. Neuroengineering Rehabil. Res. *11*, 76.

Frisoni, G.B., and Weiner, M.W. (2010). Alzheimer's Disease Neuroimaging Initiative special issue. Neurobiol. Aging *31*, 1259–1262.

Friston, K.J., Harrison, L., and Penny, W. (2003). Dynamic causal modelling. Neuroimage *19*, 1273–1302.

Fu, Q., Hasan, Z., and Santello, M. (2011). Transfer of learned manipulation following changes in degrees of freedom. J. Neurosci. *31*, 13576–13584.

Fugl-Meyer, A.R., Jääskö, L., Leyman, I., Olsson, S., and Steglind, S. (1975). The post-stroke hemiplegic patient. 1. a method for evaluation of physical performance. Scand. J. Rehabil. Med. *7*, 13–31.

Funahashi, R., Maruyama, T., Yoshimura, Y., and Komatsu, Y. (2013). Silent synapses persist into adulthood in layer 2/3 pyramidal neurons of visual cortex in dark-reared mice. J. Neurophysiol. *109*, 2064–2076.

Gatti, R., Tettamanti, A., Gough, P.M., Riboldi, E., Marinoni, L., and Buccino, G. (2013). Action observation versus motor imagery in learning a complex motor task: a short review of literature and a kinematics study. Neurosci. Lett. *540*, 37–42.

Gerhard, S., Daducci, A., Lemkaddem, A., Meuli, R., Thiran, J.-P., and Hagmann, P. (2011). The connectome viewer toolkit: an open source framework to manage, analyze, and visualize connectomes. Front. Neuroinform. *5*, 3.

GESCHWIND, N. (1965). DISCONNEXION SYNDROMES IN ANIMALS AND MAN. Brain *88*, 237–237.

Geschwind, N. (1970). The organization of language and the brain. Science *170*, 940–944.

Geschwind, D.H., Perlman, S., Figueroa, K.P., Karrim, J., Baloh, R.W., and Pulst, S.M. (1997). Spinocerebellar ataxia type 6. Frequency of the mutation and genotype-phenotype correlations. Neurology *49*, 1247–1251.

Gierga, K., Schelhaas, H.J., Brunt, E.R., Seidel, K., Scherzed, W., Egensperger, R., de

Vos, R.A.I., den Dunnen, W., Ippel, P.F., Petrasch-Parwez, E., et al. (2009). Spinocerebellar ataxia type 6 (SCA6): neurodegeneration goes beyond the known brain predilection sites. Neuropathol. Appl. Neurobiol. *35*, 515–527.

Giunti, P., Mantuano, E., Frontali, M., and Veneziano, L. (2015). Molecular mechanism of Spinocerebellar Ataxia type 6: glutamine repeat disorder, channelopathy and transcriptional dysregulation. The multifaceted aspects of a single mutation. Front. Cell. Neurosci. *9*, 36.

Globas, C., du Montcel, S.T., Baliko, L., Boesch, S., Depondt, C., DiDonato, S., Durr, A., Filla, A., Klockgether, T., Mariotti, C., et al. (2008). Early symptoms in spinocerebellar ataxia type 1, 2, 3, and 6. Mov. Disord. *23*, 2232–2238.

Go, A.S., Mozaffarian, D., Roger, V.L., Benjamin, E.J., Berry, J.D., Blaha, M.J., Dai, S., Ford, E.S., Fox, C.S., Franco, S., et al. (2014). Heart disease and stroke statistics--2014 update: a report from the American Heart Association. Circulation *129*, e28–e292.

Godwin, K.M., Wasserman, J., and Ostwald, S.K. (2011). Cost associated with stroke: outpatient rehabilitative services and medication. Top. Stroke Rehabil. *18 Suppl 1*, 676–684.

Gomez, C.M., Thompson, R.M., Gammack, J.T., Perlman, S.L., Dobyns, W.B., Truwit, C.L., Zee, D.S., Clark, H.B., and Anderson, J.H. (1997). Spinocerebellar ataxia type 6: gaze-evoked and vertical nystagmus, Purkinje cell degeneration, and variable age of onset. Ann. Neurol. *42*, 933–950.

Goni, J. (2013). Resting-brain functional connectivity predicted by analytic measures of network communication.

Grefkes, C., and Fink, G.R. (2012). Disruption of motor network connectivity post-stroke and its noninvasive neuromodulation. Curr. Opin. Neurol. *25*, 670–675.

Grefkes, C., and Ward, N.S. (2013). Cortical Reorganization After Stroke: How Much and How Functional? Neuroscientist.

Grefkes, C., Nowak, D.A., Eickhoff, S.B., Dafotakis, M., Küst, J., Karbe, H., and Fink, G.R. (2008). Cortical connectivity after subcortical stroke assessed with functional magnetic resonance imaging. Ann. Neurol. *63*, 236–246.

Greschwind, N., and Galaburda, A. (1987). Cerebral lateralization: Biological mechanisms, associations, and pathology.

Group, B.D.W. (2001). Biomarkers and surrogate endpoints: preferred definitions and conceptual framework. Clin. Pharmacol. Ther. *69*, 89–95.

Gu, H. (2013). Biological experimental observations of an unnoticed chaos as simulated by the Hindmarsh-Rose model. PLoS One *8*, e81759.

Hagmann, P., Cammoun, L., Gigandet, X., Meuli, R., Honey, C.J., Wedeen, V.J., and Sporns, O. (2008). Mapping the structural core of human cerebral cortex. PLoS Biol. *6*, e159.

Hallett, M. (2007). Transcranial magnetic stimulation: a primer. Neuron *55*, 187–199.

Hamburg, M.A., and Collins, F.S. (2010). The path to personalized medicine. N. Engl. J. Med. *363*, 301–304.

HAMILTON, M. (1960). A rating scale for depression. J. Neurol. Neurosurg. Psychiatry *23*, 56–62.

Hari, R., Bourguignon, M., Piitulainen, H., Smeds, E., De Tiège, X., and Jousmäki, V. (2014). Human primary motor cortex is both activated and stabilized during observation of other person's phasic motor actions. Philos. Trans. R. Soc. Lond. B. Biol. Sci. *369*, 20130171.

Harris, V.K., and Sadiq, S.A. (2014). Biomarkers of therapeutic response in multiple sclerosis: current status. Mol. Diagn. Ther. *18*, 605–617.

Hartman, D., Hlinka, J., Palus, M., Mantini, D., and Corbetta, M. (2011). The role of nonlinearity in computing graph-theoretical properties of resting-state functional magnetic resonance imaging brain networks. Chaos *21*, 013119.

Heald, A., Bates, D., Cartlidge, N.E., French, J.M., and Miller, S. (1993). Longitudinal study of central motor conduction time following stroke. 1. Natural history of central motor conduction. Brain *116 (Pt 6*, 1355–1370.

Hekman, K.E., and Gomez, C.M. (2015). The autosomal dominant spinocerebellar ataxias: emerging mechanistic themes suggest pervasive Purkinje cell vulnerability. J.

Neurol. Neurosurg. Psychiatry *86*, 554–561.

Hermundstad, A.M., Bassett, D.S., Brown, K.S., Aminoff, E.M., Clewett, D., Freeman, S., Frithsen, A., Johnson, A., Tipper, C.M., Miller, M.B., et al. (2013). Structural foundations of resting-state and task-based functional connectivity in the human brain. Proc. Natl. Acad. Sci. U. S. A. *110*, 6169–6174.

Hersch, S.M., and Rosas, H.D. (2008). Neuroprotection for Huntington's disease: ready, set, slow. Neurotherapeutics *5*, 226–236.

Hess, G., Aizenman, C.D., and Donoghue, J.P. (1996). Conditions for the induction of long-term potentiation in layer II/III horizontal connections of the rat motor cortex. J Neurophysiol *75*, 1765–1778.

Hindmarsh, J.L., and Rose, R.M. (1984). A Model of Neuronal Bursting Using Three Coupled First Order Differential Equations. Proc. R. Soc. B Biol. Sci. *221*, 87–102.

Hinman, J.D., Lee, M.D., Tung, S., Vinters, H. V, and Carmichael, S.T. (2015). Molecular disorganization of axons adjacent to human lacunar infarcts. Brain *138*, 736–745.

Hlinka, J., Hartman, D., and Paluš, M. (2012). Small-world topology of functional connectivity in randomly connected dynamical systems. Chaos *22*, 033107.

Hoffland, B.S., Bologna, M., Kassavetis, P., Teo, J.T.H., Rothwell, J.C., Yeo, C.H., van de Warrenburg, B.P., and Edwards, M.J. (2012). Cerebellar theta burst stimulation impairs eyeblink classical conditioning. J. Physiol. *590*, 887–897.

Honey, C.J., Sporns, O., Cammoun, L., Gigandet, X., Thiran, J.P., Meuli, R., and Hagmann, P. (2009). Predicting human resting-state functional connectivity from structural connectivity. Proc. Natl. Acad. Sci. U. S. A. *106*, 2035–2040.

Horwitz, B., Hwang, C., and Alstott, J. (2013). Interpreting the effects of altered brain anatomical connectivity on fMRI functional connectivity: a role for computational neural modeling. Front. Hum. Neurosci. *7*, 649.

Hummel, F., Celnik, P., Giraux, P., Floel, A., Wu, W.-H., Gerloff, C., and Cohen, L.G. (2005). Effects of non-invasive cortical stimulation on skilled motor function in chronic stroke. Brain *128*, 490–499.

Huseyinsinoglu, B.E., Ozdincler, A.R., and Krespi, Y. (2012). Bobath Concept versus constraint-induced movement therapy to improve arm functional recovery in stroke patients: a randomized controlled trial. Clin. Rehabil. *26*, 705–715.

Hutchison, R.M., Womelsdorf, T., Allen, E.A., Bandettini, P.A., Calhoun, V.D., Corbetta, M., Della Penna, S., Duyn, J.H., Glover, G.H., Gonzalez-Castillo, J., et al. (2013). Dynamic functional connectivity: promise, issues, and interpretations. Neuroimage *80*, 360–378.

Hwang, C.H., Seong, J.W., and Son, D.-S. (2012). Individual finger synchronized robot-assisted hand rehabilitation in subacute to chronic stroke: a prospective randomized clinical trial of efficacy. Clin. Rehabil.

Ingram, J.N., Körding, K.P., Howard, I.S., and Wolpert, D.M. (2008). The statistics of natural hand movements. Exp. Brain Res. *188*, 223–236.

Irle, E. (1987). Lesion size and recovery of function: some new perspectives. Brain Res. *434*, 307–320.

Ishikawa, K., Watanabe, M., Yoshizawa, K., Fujita, T., Iwamoto, H., Yoshizawa, T., Harada, K., Nakamagoe, K., Komatsuzaki, Y., Satoh, A., et al. (1999). Clinical, neuropathological, and molecular study in two families with spinocerebellar ataxia type 6 (SCA6). J. Neurol. Neurosurg. Psychiatry *67*, 86–89.

Ito, M. (2006). Cerebellar circuitry as a neuronal machine. Prog. Neurobiol. *78*, 272–303.

Jacobi, H., Reetz, K., du Montcel, S.T., Bauer, P., Mariotti, C., Nanetti, L., Rakowicz, M., Sulek, A., Durr, A., Charles, P., et al. (2013). Biological and clinical characteristics of individuals at risk for spinocerebellar ataxia types 1, 2, 3, and 6 in the longitudinal RISCA study: analysis of baseline data. Lancet. Neurol. *12*, 650–658.

Jahromi, S.S., and Atwood, H.L. (1974). Three-dimensional ultrastructure of the crayfish neuromuscular apparatus. J. Cell Biol. *63*, 599–613.

Jenkinson, M., Bannister, P., Brady, M., and Smith, S. (2002). Improved optimization for the robust and accurate linear registration and motion correction of brain images. Neuroimage *17*, 825–841.

Jiang, T. (2013). Brainnetome: a new -ome to understand the brain and its disorders. Neuroimage *80*, 263–272.

Jirsa, V.K., and Stefanescu, R.A. (2011). Neural population modes capture biologically realistic large scale network dynamics. Bull. Math. Biol. *73*, 325–343.

Jirsa, V.K., Sporns, O., Breakspear, M., Deco, G., and Mcintosh, A.R. (2010). Towards the virtual brain : network modeling of the intact and the damaged brain. 189–205.

Johnstone, T., Ores Walsh, K.S., Greischar, L.L., Alexander, A.L., Fox, A.S., Davidson, R.J., and Oakes, T.R. (2006). Motion correction and the use of motion covariates in multiple-subject fMRI analysis. Hum. Brain Mapp. *27*, 779–788.

Joiner, W.M., Brayanov, J.B., and Smith, M.A. (2013). The training schedule affects the stability, not the magnitude, of the interlimb transfer of learned dynamics. J. Neurophysiol. *110*, 984–998.

Jung, K.-H., and Lee, K.-H. (2015). Molecular imaging in the era of personalized medicine. J. Pathol. Transl. Med. *49*, 5–12.

Kamper, D.G., and Rymer, W.Z. (2001). Impairment of voluntary control of finger motion following stroke: role of inappropriate muscle coactivation. Muscle Nerve *24*, 673–681.

Karim, A.R., and Jacob, S. (2012). Immunological markers in neurological disorders. Ann. Clin. Biochem. *49*, 29–43.

Kerchner, G.A., and Nicoll, R.A. (2008). Silent synapses and the emergence of a postsynaptic mechanism for LTP. Nat. Rev. Neurosci. *9*, 813–825.

Kheradmand, A., and Zee, D.S. (2011). Cerebellum and ocular motor control. Front. Neurol. *2*, 53.

Kilbreath, S.L., and Gandevia, S.C. (1994). Limited independent flexion of the thumb and fingers in human subjects. J. Physiol. *479 (Pt 3)*, 487–497.

Kitago, T., Liang, J., Huang, V.S., Hayes, S., Simon, P., Tenteromano, L., Lazar, R.M., Marshall, R.S., Mazzoni, P., Lennihan, L., et al. (2013a). Improvement after constraint-induced movement therapy: recovery of normal motor control or task-specific compensation? Neurorehabil. Neural Repair *27*, 99–109.

Kitago, T., Liang, J., Huang, V.S., Hayes, S., Simon, P., Tenteromano, L., Lazar, R.M., Marshall, R.S., Mazzoni, P., Lennihan, L., et al. (2013b). Improvement after constraint-induced movement therapy: recovery of normal motor control or task-specific compensation? Neurorehabil. Neural Repair *27*, 99–109.

Klöppel, S., Chu, C., Tan, G.C., Draganski, B., Johnson, H., Paulsen, J.S., Kienzle, W., Tabrizi, S.J., Ashburner, J., and Frackowiak, R.S.J. (2009). Automatic detection of preclinical neurodegeneration: presymptomatic Huntington disease. Neurology *72*, 426–431.

Koeppen, A.H. (2005). The pathogenesis of spinocerebellar ataxia. Cerebellum *4*, 62–73.

Konen, C.S., Kleiser, R., Seitz, R.J., and Bremmer, F. (2005). An fMRI study of optokinetic nystagmus and smooth-pursuit eye movements in humans. Exp. Brain Res. *165*, 203–216.

Kordasiewicz, H.B., and Gomez, C.M. (2007). Molecular pathogenesis of spinocerebellar ataxia type 6. Neurotherapeutics *4*, 285–294.

Kötter, R. (2004). Online retrieval, processing, and visualization of primate connectivity data from the CoCoMac database. Neuroinformatics *2*, 127–144.

Koziol, L.F., Budding, D., Andreasen, N., D'Arrigo, S., Bulgheroni, S., Imamizu, H., Ito, M., Manto, M., Marvel, C., Parker, K., et al. (2014). Consensus paper: the cerebellum's role in movement and cognition. Cerebellum *13*, 151–177.

Lang, C.E., and Schieber, M.H. (2003). Differential impairment of individuated finger movements in humans after damage to the motor cortex or the corticospinal tract. J. Neurophysiol. *90*, 1160–1170.

Lang, C.E., and Schieber, M.H. (2004). Human finger independence: limitations due to passive mechanical coupling versus active neuromuscular control. J. Neurophysiol. *92*, 2802–2810.

Larsen, M.L., Hørder, M., and Mogensen, E.F. (1990). Effect of long-term monitoring of glycosylated hemoglobin levels in insulin-dependent diabetes mellitus. N. Engl. J. Med. *323*, 1021–1025.

Lawrence, DG, Kuypers, H. (2012). Lawrence and Kuypers (1968a , 1968b) revisited : Neurology.

Lee, R.G., and van Donkelaar, P. (1995). Mechanisms underlying functional recovery following stroke. Can. J. Neurol. Sci. *22*, 257–263.

Lee, L., Friston, K., and Horwitz, B. (2006). Large-scale neural models and dynamic causal modelling. Neuroimage *30*, 1243–1254.

Leemans, A., and Jones, D.K. (2009). The B-matrix must be rotated when correcting for subject motion in DTI data. Magn. Reson. Med. *61*, 1336–1349.

Leggo, J., Dalton, A., Morrison, P.J., Dodge, A., Connarty, M., Kotze, M.J., and Rubinsztein, D.C. (1997). Analysis of spinocerebellar ataxia types 1, 2, 3, and 6, dentatorubral-pallidoluysian atrophy, and Friedreich's ataxia genes in spinocerebellar ataxia patients in the UK. J. Med. Genet. *34*, 982–985.

LeMay, M. (1976). MORPHOLOGICAL CEREBRAL ASYMMETRIES OF MODERN MAN, FOSSIL MAN, AND NONHUMAN PRIMATE. Ann. N. Y. Acad. Sci. *280*, 349–366.

Lemon, R.N., Mantel, G.W., and Muir, R.B. (1986). Corticospinal facilitation of hand muscles during voluntary movement in the conscious monkey. J. Physiol. *381*, 497–527.

de Leon, M., Bobinski, M., Convit, A., Wolf, O., Insausti, R., Jack, C.R., Xu, Y., and Petersen, R.C. (2001). Usefulness of MRI measures of entorhinal cortex versus hippocampus in AD. Neurology *56*, 820–823.

Levin, M.F., Kleim, J. a, and Wolf, S.L. (2009). What do motor "recovery" and "compensation" mean in patients following stroke? Neurorehabil. Neural Repair *23*, 313–319.

Liem, E.I.M.L., Frens, M.A., Smits, M., and van der Geest, J.N. (2013). Cerebellar activation related to saccadic inaccuracies. Cerebellum *12*, 224–235.

Liepert, J. (2003). TMS in stroke. Suppl. Clin. Neurophysiol. *56*, 368–380.

Liepert, J., Graef, S., Uhde, I., Leidner, O., and Weiller, C. (2000). Training-induced changes of motor cortex representations in stroke patients. Acta Neurol. Scand. *101*,

321–326.

Logothetis, N.K., Pauls, J., Augath, M., Trinath, T., and Oeltermann, a (2001). Neurophysiological investigation of the basis of the fMRI signal. Nature *412*, 150–157.

Lohse, C., Bassett, D.S., Lim, K.O., and Carlson, J.M. (2014). Resolving anatomical and functional structure in human brain organization: identifying mesoscale organization in weighted network representations. PLoS Comput. Biol. *10*, e1003712.

Losi, G., Prybylowski, K., Fu, Z., Luo, J.H., and Vicini, S. (2002). Silent Synapses in Developing Cerebellar Granule Neurons. J Neurophysiol *87*, 1263–1270.

Lukas, C., Schöls, L., Bellenberg, B., Rüb, U., Przuntek, H., Schmid, G., Köster, O., and Suchan, B. (2006). Dissociation of grey and white matter reduction in spinocerebellar ataxia type 3 and 6: a voxel-based morphometry study. Neurosci. Lett. *408*, 230–235.

Lund, T.E., Madsen, K.H., Sidaros, K., Luo, W.-L., and Nichols, T.E. (2006). Non-white noise in fMRI: does modelling have an impact? Neuroimage *29*, 54–66.

Lynch, J.C., and Tian, J.-R. (2006). Cortico-cortical networks and cortico-subcortical loops for the higher control of eye movements. Prog. Brain Res. *151*, 461–501.

Maier, M.A., Kirkwood, P.A., Brochier, T., and Lemon, R.N. (2013). Responses of single corticospinal neurons to intracortical stimulation of primary motor and premotor cortex in the anesthetized macaque monkey. J. Neurophysiol. *109*, 2982–2998.

Malfait, N., and Ostry, D.J. (2004). Is interlimb transfer of force-field adaptation a cognitive response to the sudden introduction of load? J. Neurosci. *24*, 8084–8089.

Mannella, R. (2002). Integration of stochastic differential equations on a computer.

Mantuano, E., Veneziano, L., Jodice, C., and Frontali, M. (2003). Spinocerebellar ataxia type 6 and episodic ataxia type differences and similarities between two allelic disorders. Cytogenet Genome Res 100 *2 SRC - G*, 147–153.

Maschke, M., Oehlert, G., Xie, T.-D., Perlman, S., Subramony, S.H., Kumar, N., Ptacek, L.J., and Gomez, C.M. Clinical feature profile of spinocerebellar ataxia type 1-8 predicts genetically defined subtypes. Mov. Disord. *20*, 1405–1412.

Mashal, N., Solodkin, A., Dick, A.S., Chen, E.E., and Small, S.L. (2012). A network

model of observation and imitation of speech. Front. Psychol. *3*, 84.

Mathiowetz, V., Weber, K., Kashman, N., and Volland, G. (1985). Adult norms for the Nine Hole Peg Test of finger dexterity. Occup. Ther. J. Res. *5*, 24–38.

Matsumura, R., Futamura, N., Ando, N., and Ueno, S. Frequency of spinocerebellar ataxia mutations in the Kinki district of Japan. Acta Neurol. Scand. *107*, 38–41.

Matthews, P.M., Edison, P., Geraghty, O.C., and Johnson, M.R. (2014). The emerging agenda of stratified medicine in neurology. Nat. Rev. Neurol. *10*, 15–26.

McDowell, J.E., Dyckman, K.A., Austin, B.P., and Clementz, B.A. (2008). Neurophysiology and neuroanatomy of reflexive and volitional saccades: evidence from studies of humans. Brain Cogn. *68*, 255–270.

McHughen, S.A., Rodriguez, P.F., Kleim, J.A., Kleim, E.D., Marchal Crespo, L., Procaccio, V., and Cramer, S.C. (2010). BDNF val66met polymorphism influences motor system function in the human brain. Cereb. Cortex *20*, 1254–1262.

McIntosh, A.R. (2000). Towards a network theory of cognition. Neural Networks *13*, 861–870.

McIntosh, a. R., and Gonzalez-Lima, F. (1994). Structural equation modeling and its application to network analysis in functional brain imaging. Hum. Brain Mapp. *2*, 2–22.

van Meer, M.P.A., van der Marel, K., Otte, W.M., Berkelbach van der Sprenkel, J.W., and Dijkhuizen, R.M. (2010). Correspondence between altered functional and structural connectivity in the contralesional sensorimotor cortex after unilateral stroke in rats: a combined resting-state functional MRI and manganese-enhanced MRI study. J. Cereb. Blood Flow Metab. *30*, 1707–1711.

Miller, D.B., and O'Callaghan, J.P. (2014). Biomarkers of Parkinson's Disease (Pd): Present and Future. Metabolism *64*, S40–S46.

Milot, M.-H., and Cramer, S.C. (2008). Biomarkers of recovery after stroke. Curr. Opin. Neurol. *21*, 654–659.

Milton, J., Solodkin, A., Hlustík, P., and Small, S.L. (2007). The mind of expert motor performance is cool and focused. Neuroimage *35*, 804–813.

Mintun, M.A. (2005). Utilizing advanced imaging and surrogate markers across the spectrum of Alzheimer's disease. CNS Spectr. *10*, 13–16.

Mitra, P.P. (2014). The Circuit Architecture of Whole Brains at the Mesoscopic Scale. Neuron *83*, 1273–1283.

Molenberghs, P., Cunnington, R., and Mattingley, J.B. (2012). Brain regions with mirror properties: a meta-analysis of 125 human fMRI studies. Neurosci. Biobehav. Rev. *36*, 341–349.

Moon, S.K., Alaverdashvili, M., Cross, A.R., and Whishaw, I.Q. (2009). Both compensation and recovery of skilled reaching following small photothrombotic stroke to motor cortex in the rat. Exp. Neurol. *218*, 145–153.

Moran, R.J., Symmonds, M., Stephan, K.E., Friston, K.J., and Dolan, R.J. (2011). An in vivo assay of synaptic function mediating human cognition. Curr. Biol. *21*, 1320–1325.

Mori, S., and van Zijl, P.C.M. (2002). Fiber tracking: principles and strategies - a technical review. NMR Biomed. *15*, 468–480.

Mori, S., Crain, B.J., Chacko, V.P., and Van Zijl, P.C.M. (1999). Three-dimensional tracking of axonal projections in the brain by magnetic resonance imaging. Ann. Neurol. *45*, 265–269.

Mueller, S., Wang, D., Fox, M.D., Yeo, B.T.T., Sepulcre, J., Sabuncu, M.R., Shafee, R., Lu, J., and Liu, H. (2013a). Individual variability in functional connectivity architecture of the human brain. Neuron *77*, 586–595.

Mueller, S., Keeser, D., Samson, A.C., Kirsch, V., Blautzik, J., Grothe, M., Erat, O., Hegenloh, M., Coates, U., Reiser, M.F., et al. (2013b). Convergent Findings of Altered Functional and Structural Brain Connectivity in Individuals with High Functioning Autism: A Multimodal MRI Study. PLoS One *8*, e67329.

Muir, R.B., and Lemon, R.N. (1983). Corticospinal neurons with a special role in precision grip. Brain Res. *261*, 312–316.

Munshi, A., and Sharma, V. (2015). Genetic signatures in the treatment of stroke. Curr. Pharm. Des. *21*, 343–354.

Murata, Y., Kawakami, H., Yamaguchi, S., Nishimura, M., Kohriyama, T., Ishizaki, F., Matsuyama, Z., Mimori, Y., and Nakamura, S. Characteristic magnetic resonance imaging findings in spinocerebellar ataxia 6. Arch. Neurol. *55*, 1348–1352.

Nakayama, K., Kiyosue, K., and Taguchi, T. Diminished neuronal activity increases neuron-neuron connectivity underlying silent synapse formation and the rapid conversion of silent to functional synapses. J. Neurosci. *25*, 4040–4051.

Nalls, M.A., McLean, C.Y., Rick, J., Eberly, S., Hutten, S.J., Gwinn, K., Sutherland, M., Martinez, M., Heutink, P., Williams, N.M., et al. (2015). Diagnosis of Parkinson's disease on the basis of clinical and genetic classification: a population-based modelling study. Lancet. Neurol. *14*, 1002–1009.

Nelson, P.T., Alafuzoff, I., Bigio, E.H., Bouras, C., Braak, H., Cairns, N.J., Castellani, R.J., Crain, B.J., Davies, P., Del Tredici, K., et al. (2012). Correlation of Alzheimer disease neuropathologic changes with cognitive status: a review of the literature. J. Neuropathol. Exp. Neurol. *71*, 362–381.

Nichols-Larsen, D.S., Clark, P.C., Zeringue, A., Greenspan, A., and Blanton, S. (2005). Factors influencing stroke survivors' quality of life during subacute recovery. Stroke. *36*, 1480–1484.

Nilsson, M., van Westen, D., Ståhlberg, F., Sundgren, P.C., and Lätt, J. The role of tissue microstructure and water exchange in biophysical modelling of diffusion in white matter. MAGMA *26*, 345–370.

Nitschke, M.F., Binkofski, F., Buccino, G., Posse, S., Erdmann, C., Kömpf, D., Seitz, R.J., and Heide, W. Activation of cerebellar hemispheres in spatial memorization of saccadic eye movements: an fMRI study. Hum. Brain Mapp. *22*, 155–164.

Nudo, R.J. (2013). Recovery after brain injury: mechanisms and principles. Front. Hum. Neurosci. *7*, 887.

Oda, R., Takemoto, T., Kawai, M., and Yamashita, H. [Study of oculomotor disorders in spinocerebellar ataxia genotype]. Nihon Jibiinkoka Gakkai Kaiho *109*, 30–35.

Oldfield, R.C. (1971). The assessment and analysis of handedness: the Edinburgh inventory. Neuropsychologia *9*, 97–113.

Oxford Grice, K., Vogel, K.A., Le, V., Mitchell, A., Muniz, S., and Vollmer, M.A. (2003). Adult Norms for a Commercially Available Nine Hole Peg Test for Finger Dexterity. Am. J. Occup. Ther. *57*, 570–573.

Page, S.J., Levine, P., Sisto, S., Bond, Q., and Johnston, M. V (2002). Stroke patients' and therapists' opinions of constraint-induced movement therapy. Clin. Rehabil. *16*, 55–60.

Page, S.J., Gauthier, L. V, and White, S. (2013). Size doesn't matter: cortical stroke lesion volume is not associated with upper extremity motor impairment and function in mild, chronic hemiparesis. Arch. Phys. Med. Rehabil. *94*, 817–821.

Paolucci, S., Grasso, M.G., Antonucci, G., Bragoni, M., Troisi, E., Morelli, D., Coiro, P., De Angelis, D., and Rizzi, F. (2001). Mobility status after inpatient stroke rehabilitation: 1-Year follow-up and prognostic factors. Arch. Phys. Med. Rehabil. *82*, 2–8.

Pearson-Fuhrhop, K.M., Burke, E., and Cramer, S.C. (2012). The influence of genetic factors on brain plasticity and recovery after neural injury. Curr. Opin. Neurol. *25*, 682–688.

di Pellegrino, G., Fadiga, L., Fogassi, L., Gallese, V., and Rizzolatti, G. (1992). Understanding motor events: a neurophysiological study. Exp. Brain Res. *91*, 176–180.

Pennisi, G. (2002). Transcranial magnetic stimulation after pure motor stroke. Clin. Neurophysiol. *113*, 1536–1543.

Poldrack, R.A., and Gorgolewski, K.J. (2014). Making big data open: data sharing in neuroimaging. Nat. Neurosci. *17*, 1510–1517.

Porrill, J., and Dean, P. (2008). Silent synapses, LTP, and the indirect parallel-fibre pathway: computational consequences of optimal cerebellar noise-processing. PLoS Comput. Biol. *4*, e1000085.

Porro, C. a., Facchin, P., Fusi, S., Dri, G., and Fadiga, L. (2007). Enhancement of force after action observation. Behavioural and neurophysiological studies. Neuropsychologia *45*, 3114–3121.

Prevosto, V., and Sommer, M.A. (2013). Cognitive control of movement via the cerebellar-recipient thalamus. Front. Syst. Neurosci. *7*, 56.

Ramnani, N. (2006). The primate cortico-cerebellar system: anatomy and function. Nat. Rev. Neurosci. *7*, 511–522.

Ramnani, N. (2012). Frontal lobe and posterior parietal contributions to the cortico-cerebellar system. Cerebellum *11*, 366–383.

Rasband, M.N. (2011). Composition, assembly, and maintenance of excitable membrane domains in myelinated axons. Semin. Cell Dev. Biol. *22*, 178–184.

Reetz, K., Costa, A.S., Mirzazade, S., Lehmann, A., Juzek, A., Rakowicz, M., Boguslawska, R., Schöls, L., Linnemann, C., Mariotti, C., et al. (2013). Genotype-specific patterns of atrophy progression are more sensitive than clinical decline in SCA1, SCA3 and SCA6. Brain *136*, 905–917.

Rehme, A.K., and Grefkes, C. (2013). Cerebral network disorders after stroke: evidence from imaging-based connectivity analyses of active and resting brain states in humans. J. Physiol. *591*, 17–31.

Rehme, A.K., Eickhoff, S.B., Rottschy, C., Fink, G.R., and Grefkes, C. (2012). Activation likelihood estimation meta-analysis of motor-related neural activity after stroke. Neuroimage *59*, 2771–2782.

Reinkensmeyer, D.J., Guigon, E., and Maier, M. a (2012). A computational model of use-dependent motor recovery following a stroke: optimizing corticospinal activations via reinforcement learning can explain residual capacity and other strength recovery dynamics. Neural Netw. *29-30*, 60–69.

Reiss, A.P., Wolf, S.L., Hammel, E.A., McLeod, E.L., and Williams, E.A. (2012). Constraint-Induced Movement Therapy (CIMT): Current Perspectives and Future Directions. Stroke Res. Treat. *2012*, 159391.

De Renzi, E., and Faglioni, P. (1978). Normative data and screening power of a shortened version of the Token Test. Cortex. *14*, 41–49.

Riley, J.D., Le, V., Der-Yeghiaian, L., See, J., Newton, J.M., Ward, N.S., and Cramer, S.C. (2011). Anatomy of stroke injury predicts gains from therapy. Stroke. *42*, 421–426.

Ritter, P., Schirner, M., McIntosh, A.R., and Jirsa, V.K. (2013a). The virtual brain integrates computational modeling and multimodal neuroimaging. Brain Connect. *3*,

121–145.

Ritter, P., Schirner, M., McIntosh, A.R., and Jirsa, V. (2013b). The Virtual Brain Integrates Computational Modelling and Multimodal Neuroimaging. Brain Connect. *49*, 1–65.

Rizk-Jackson, A., Stoffers, D., Sheldon, S., Kuperman, J., Dale, A., Goldstein, J., Corey-Bloom, J., Poldrack, R.A., and Aron, A.R. (2011). Evaluating imaging biomarkers for neurodegeneration in pre-symptomatic Huntington's disease using machine learning techniques. Neuroimage *56*, 788–796.

Roebroeck, A., Formisano, E., and Goebel, R. (2011). The identification of interacting networks in the brain using fMRI: Model selection, causality and deconvolution. Neuroimage *58*, 296–302.

Rosati, G., Oscari, F., Reinkensmeyer, D.J., Secoli, R., Avanzini, F., Spagnol, S., and Masiero, S. (2011). Improving robotics for neurorehabilitation: enhancing engagement, performance, and learning with auditory feedback. IEEE Int. Conf. Rehabil. Robot. *2011*, 5975373.

Rosenzweig, S., and Carmichael, S.T. (2015). The axon-glia unit in white matter stroke: Mechanisms of damage and recovery. Brain Res. *1623*, 123–134.

Roy, D., Sigala, R., Breakspear, M., McIntosh, A.R., Jirsa, V.K., Deco, G., and Ritter, P. (2014). Using the virtual brain to reveal the role of oscillations and plasticity in shaping brain's dynamical landscape. Brain Connect. *4*, 791–811.

Rüb, U., Schöls, L., Paulson, H., Auburger, G., Kermer, P., Jen, J.C., Seidel, K., Korf, H.-W., and Deller, T. (2013). Clinical features, neurogenetics and neuropathology of the polyglutamine spinocerebellar ataxias type 1, 2, 3, 6 and 7. Prog. Neurobiol. *104*, 38–66.

Rubinov, M., and Sporns, O. (2010). Complex network measures of brain connectivity: uses and interpretations. Neuroimage *52*, 1059–1069.

Rubinov, M., Sporns, O., van Leeuwen, C., and Breakspear, M. (2009). Symbiotic relationship between brain structure and dynamics. BMC Neurosci. *10*, 55.

Saad, Z., and Reynolds, R. (2004). SUMA: an interface for surface-based intra-and

inter-subject analysis with AFNI. … Imaging Nano to … 1510–1513.

Sacco, R.L., Kasner, S.E., Broderick, J.P., Caplan, L.R., Connors, J.J.B., Culebras, A., Elkind, M.S. V, George, M.G., Hamdan, A.D., Higashida, R.T., et al. (2013). An updated definition of stroke for the 21st century: a statement for healthcare professionals from the American Heart Association/American Stroke Association. Stroke. *44*, 2064–2089.

Sakakibara, S., Aiba, I., Saito, Y., Inukai, A., Ishikawa, K., and Mizusawa, H. (2014). [Clinical features and MRI findings in spinocerebellar ataxia type 31 (SCA31) comparing with spinocerebellar ataxia type 6 (SCA6)]. Rinshō Shinkeigaku = Clin. Neurol. *54*, 473–479.

Santello, M., Baud-Bovy, G., and Jörntell, H. (2013). Neural bases of hand synergies. Front. Comput. Neurosci. *7*, 23.

Sanz Leon, P., Knock, S. a, Woodman, M.M., Domide, L., Mersmann, J., McIntosh, A.R., and Jirsa, V. (2013). The Virtual Brain: a simulator of primate brain network dynamics. Front. Neuroinform. *7*, 10.

Sanz-Leon, P., Knock, S.A., Spiegler, A., and Jirsa, V.K. (2015a). Mathematical framework for large-scale brain network modelling in The Virtual Brain. Neuroimage *111*, 385–430.

Sanz-Leon, P., Knock, S.A., Spiegler, A., and Jirsa, V.K. (2015b). Mathematical framework for large-scale brain network modeling in The Virtual Brain. Neuroimage *111*, 385–430.

Sasaki, H., Kojima, H., Yabe, I., Tashiro, K., Hamada, T., Sawa, H., Hiraga, H., and Nagashima, K. Neuropathological and molecular studies of spinocerebellar ataxia type 6 (SCA6). Acta Neuropathol. *95*, 199–204.

Sasaki, H., Yabe, I., and Tashiro, K. (2003). The hereditary spinocerebellar ataxias in Japan. Cytogenet. Genome Res. *100*, 198–205.

Satoh, T., Sasatomi, E., Yamasaki, F., Ishida, H., Wu, L., and Tokunaga, O. (1998). Multinucleated variant endothelial cells (MVECs) of human aorta: expression of tumor suppressor gene p53 and relationship to atherosclerosis and aging. Endothelium *6*, 123–132.

Savioz, A., Leuba, G., Vallet, P.G., and Walzer, C. Contribution of neural networks to Alzheimer disease's progression. Brain Res. Bull. *80*, 309–314.

Scheinost, D., Finn, E.S., Tokoglu, F., Shen, X., Papademetris, X., Hampson, M., and Constable, R.T. (2015). Sex differences in normal age trajectories of functional brain networks. Hum. Brain Mapp. *36*, 1524–1535.

Scheller, E., Abdulkadir, A., Peter, J., Tabrizi, S.J., Frackowiak, R.S.J., and Klöppel, S. (2013). Interregional compensatory mechanisms of motor functioning in progressing preclinical neurodegeneration. Neuroimage *75*, 146–154.

Schieber, M.H. (1990). How might the motor cortex individuate movements ? Trends Neurosci. 440–445.

Schieber, M.H. (1991). Individuated finger movements of rhesus monkeys: a means of quantifying the independence of the digits. J. Neurophysiol. *65*, 1381–1391.

Schieber, M.H. (2002). Motor cortex and the distributed anatomy of finger movements. Adv. Exp. Med. Biol. *508*, 411–416.

Schieber, M.H., Lang, C.E., Reilly, K., McNulty, P., and Sirigu, A. (2009). Selective Activation of Human Finger Muscles after Stroke or Amputation. Adv. Exp. Med. Biol. *629*, 559–575.

Schiene, K., Bruehl, C., Zilles, K., Qü, M., Hagemann, G., Kraemer, M., and Witte, O.W. (1996). Neuronal hyperexcitability and reduction of GABAA-receptor expression in the surround of cerebral photothrombosis. J. Cereb. Blood Flow Metab. *16*, 906–914.

Schmahmann, J.D., and Caplan, D. Cognition, emotion and the cerebellum. Brain *129*, 290–292.

Schols, L., Kruger, R., Amoiridis, G., Przuntek, H., Epplen, J.T., and Riess, O. (1998). Spinocerebellar ataxia type genotype and phenotype in German kindreds. Neurosurg Psychiatry 64 *6 SRC - G*, 67–73.

Scholz, S.W., Mhyre, T., Ressom, H., Shah, S., and Federoff, H.J. (2012). Genomics and bioinformatics of Parkinson's disease. Cold Spring Harb. Perspect. Med. *2*, a009449.

Schult, D., and Swart, P. (2008). Exploring network structure, dynamics, and function using NetworkX. Proc. 7th Python Sci. ….

Schulz, J.B., Borkert, J., Wolf, S., Schmitz-Hübsch, T., Rakowicz, M., Mariotti, C., Schöls, L., Schoels, L., Timmann, D., van de Warrenburg, B., et al. (2010). Visualization, quantification and correlation of brain atrophy with clinical symptoms in spinocerebellar ataxia types 1, 3 and 6. Neuroimage *49*, 158–168.

Seidel, K., Siswanto, S., Brunt, E.R.P., den Dunnen, W., Korf, H.-W., and Rüb, U. (2012). Brain pathology of spinocerebellar ataxias. Acta Neuropathol. *124*, 1–21.

Seidl, A.H., Sanchez, J.T., Schecterson, L., Tabor, K.M., Wang, Y., Kashima, D.T., Poynter, G., Huss, D., Fraser, S.E., Lansford, R., et al. Transgenic quail as a model for research in the avian nervous system: a comparative study of the auditory brainstem. J. Comp. Neurol. *521*, 5–23.

Selverston, A.I., and Ayers, J. (2006). Oscillations and oscillatory behavior in small neural circuits. Biol. Cybern. *95*, 537–554.

Shea, C.H., Wright, D.L., Wulf, G., and Whitacre, C. (2000). Physical and observational practice afford unique learning opportunities. J. Mot. Behav. *32*, 27–36.

Shen, K., Hutchison, R.M., Bezgin, G., Everling, S., and McIntosh, A.R. (2015a). Network Structure Shapes Spontaneous Functional Connectivity Dynamics. J. Neurosci. *35*, 5579–5588.

Shen, K., Mišić, B., Cipollini, B.N., Bezgin, G., Buschkuehl, M., Hutchison, R.M., Jaeggi, S.M., Kross, E., Peltier, S.J., Everling, S., et al. (2015b). Stable long-range interhemispheric coordination is supported by direct anatomical projections. Proc. Natl. Acad. Sci. U. S. A. *112*, 6473–6478.

Shepherd, G.M. (1972). The neuron doctrine: a revision of functional concepts. Yale J. Biol. Med. *45*, 584–599.

Shibata, D., Kappers, A.M.L., and Santello, M. (2014). Digit forces bias sensorimotor transformations underlying control of fingertip position. Front. Hum. Neurosci. *8*, 564.

Shimizu, T. (2002). Motor cortical disinhibition in the unaffected hemisphere after unilateral cortical stroke. Brain *125*, 1896–1907.

Shu, N., Liu, Y., Li, K., Duan, Y., Wang, J., Yu, C., Dong, H., Ye, J., and He, Y. (2011). Diffusion tensor tractography reveals disrupted topological efficiency in white matter structural networks in multiple sclerosis. Cereb. Cortex *21*, 2565–2577.

Small, S., Buccino, G., and Solodkin, A. (2013a). Brain repair after stroke-a novel neurological model. Nat. Rev. Neurol. *9*, 698–707.

Small, S.L., Hlustik, P., Noll, D.C., Genovese, C., and Solodkin, a (2002). Cerebellar hemispheric activation ipsilateral to the paretic hand correlates with functional recovery after stroke. Brain *125*, 1544–1557.

Small, S.L., Buccino, G., and Solodkin, A. (2012). The mirror neuron system and treatment of stroke. Dev. Psychobiol. *54*, 293–310.

Small, S.L., Buccino, G., and Solodkin, A. (2013b). Brain repair after stroke-a novel neurological model. Nat. Rev. Neurol. *9*, 698–707.

Smith, M.C. (1975). Histological findings after hemicerebellectomy in man: anterograde, retrograde and transneuronal degeneration. Brain Res. *95*, 423–442.

Smith, S.M. (2002). Fast robust automated brain extraction. Hum. Brain Mapp. *17*, 143–155.

Smith, S.M., Vidaurre, D., Beckmann, C.F., Glasser, M.F., Jenkinson, M., Miller, K.L., Nichols, T.E., Robinson, E.C., Salimi-Khorshidi, G., Woolrich, M.W., et al. (2013). Functional connectomics from resting-state fMRI. Trends Cogn. Sci. *17*, 666–682.

Solodkin, A., Hlustik, P., Chen, E., and Small, S. (2004). Fine modulation in network activation during motor execution and motor imagery. Cereb. Cortex.

Solodkin, A., Hasson, U., Siugzdaite, R., Schiel, M., Chen, E.E., Kotter, R., and Small, S.L. (2010). Virtual brain transplantation (VBT): a method for accurate image registration and parcellation in large cortical stroke. Arch. Ital. Biol. *148*, 219–241.

Solodkin, A., Peri, E., Chen, E.E., Ben-Jacob, E., and Gomez, C.M. (2011). Loss of intrinsic organization of cerebellar networks in spinocerebellar ataxia type 1: correlates with disease severity and duration. Cerebellum *10*, 218–232.

Solodkin, A., Chen, E.E., Van Hoesen, G.W., Heimer, L., Shereen, A., Kruggel, F., and

Mastrianni, J. (2013). In vivo parahippocampal white matter pathology as a biomarker of disease progression to Alzheimer's disease. J. Comp. Neurol. *521*, 4300–4317.

Song, S.-K., Sun, S.-W., Ramsbottom, M.J., Chang, C., Russell, J., and Cross, A.H. (2002). Dysmyelination Revealed through MRI as Increased Radial (but Unchanged Axial) Diffusion of Water. Neuroimage *17*, 1429–1436.

Sotelo, C. (2011). Camillo Golgi and Santiago Ramon y Cajal: the anatomical organization of the cortex of the cerebellum. Can the neuron doctrine still support our actual knowledge on the cerebellar structural arrangement? Brain Res. Rev. *66*, 16–34.

Sotero, R.C., and Trujillo-Barreto, N.J. (2008). Biophysical model for integrating neuronal activity, EEG, fMRI and metabolism. Neuroimage *39*, 290–309.

Sotiropoulos, S.N., Jbabdi, S., Xu, J., Andersson, J.L., Moeller, S., Auerbach, E.J., Glasser, M.F., Hernandez, M., Sapiro, G., Jenkinson, M., et al. (2013). Advances in diffusion MRI acquisition and processing in the Human Connectome Project. Neuroimage *80*, 125–143.

Sporns, O. (2014). Towards network substrates of brain disorders. Brain 2117–2118.

Sporns, O., Chialvo, D.R., Kaiser, M., and Hilgetag, C.C. (2004). Organization, development and function of complex brain networks. Trends Cogn. Sci. *8*, 418–425.

Sporns, O., Honey, C.J., Ko, R., Sciences, B., and Neurophysiology, S. (2007). Identification and Classification of Hubs in Brain Networks.

Stefanescu, R. a, and Jirsa, V.K. (2008). A low dimensional description of globally coupled heterogeneous neural networks of excitatory and inhibitory neurons. PLoS Comput. Biol. *4*, e1000219.

Stefanescu, M.R., Dohnalek, M., Maderwald, S., Thürling, M., Minnerop, M., Beck, A., Schlamann, M., Diedrichsen, J., Ladd, M.E., and Timmann, D. (2015). Structural and functional MRI abnormalities of cerebellar cortex and nuclei in SCA3, SCA6 and Friedreich's ataxia. Brain *138*, 1182–1197.

Stephan, K.E., Penny, W.D., Moran, R.J., den Ouden, H.E.M., Daunizeau, J., and Friston, K.J. (2010). Ten simple rules for dynamic causal modeling. Neuroimage *49*, 3099–3109.

Stephan, T., Mascolo, A., Yousry, T.A., Bense, S., Brandt, T., and Dieterich, M. (2002). Changes in cerebellar activation pattern during two successive sequences of saccades. Hum. Brain Mapp. *16*, 63–70.

Stinear, C.M., Barber, P.A., Smale, P.R., Coxon, J.P., Fleming, M.K., and Byblow, W.D. (2007). Functional potential in chronic stroke patients depends on corticospinal tract integrity. Brain *130*, 170–180.

Stoodley, C.J., and Schmahmann, J.D. (2010). Evidence for topographic organization in the cerebellum of motor control versus cognitive and affective processing. Cortex. *46*, 831–844.

Strick, P.L., Dum, R.P., and Fiez, J.A. (2009). Cerebellum and nonmotor function. Annu. Rev. Neurosci. *32*, 413–434.

Susanto, E.A., Tong, R.K., Ockenfeld, C., and Ho, N.S. (2015). Efficacy of robot-assisted fingers training in chronic stroke survivors: a pilot randomized-controlled trial. J. Neuroeng. Rehabil. *12*, 42.

Swindale, N. V Neural synchrony, axonal path lengths, and general anesthesia: a hypothesis. Neuroscientist *9*, 440–445.

Syed, Y.A., Baer, A.S., Lubec, G., Hoeger, H., Widhalm, G., and Kotter, M.R. (2008). Inhibition of oligodendrocyte precursor cell differentiation by myelin-associated proteins. Neurosurg. Focus *24*, E5.

Taheri, H., Rowe, J., and Gardner, D. (2012). Robot-assisted guitar hero for finger rehabilitation after stroke. … Med. ….

Taheri, H., Rowe, J.B., Gardner, D., Chan, V., Gray, K., Bower, C., Reinkensmeyer, D.J., and Wolbrecht, E.T. (2014). Design and preliminary evaluation of the FINGER rehabilitation robot: controlling challenge and quantifying finger individuation during musical computer game play. J. Neuroeng. Rehabil. *11*, 10.

Takeuchi, N., Chuma, T., Matsuo, Y., Watanabe, I., and Ikoma, K. (2005). Repetitive transcranial magnetic stimulation of contralesional primary motor cortex improves hand function after stroke. Stroke. *36*, 2681–2686.

Tang, Y.-H., Ma, Y.-Y., Zhang, Z.-J., Wang, Y.-T., and Yang, G.-Y. (2015).

Opportunities and Challenges: Stem Cell-Based Therapy for the Treatment of Ischemic Stroke. CNS Neurosci. Ther.

Teichner, G., Golden, C.J., Bradley, J.D., and Crum, T.A. (1999). Internal consistency and discriminant validity of the Luria Nebraska Neuropsychological Battery-III. Int. J. Neurosci. *98*, 141–152.

Thielbar, K.O., Lord, T.J., Fischer, H.C., Lazzaro, E.C., Barth, K.C., Stoykov, M.E., Triandafilou, K.M., and Kamper, D.G. (2014). Training finger individuation with a mechatronic-virtual reality system leads to improved fine motor control post-stroke. J. Neuroeng. Rehabil. *11*, 171.

Thomas, J.B., Brier, M.R., Bateman, R.J., Snyder, A.Z., Benzinger, T.L., Xiong, C., Raichle, M., Holtzman, D.M., Sperling, R.A., Mayeux, R., et al. (2014). Functional connectivity in autosomal dominant and late-onset Alzheimer disease. JAMA Neurol. *71*, 1111–1122.

Tsou, W.-L., Soong, B.-W., Paulson, H.L., and Rodríguez-Lebrón, E. (2011). Splice isoform-specific suppression of the Cav2.1 variant underlying spinocerebellar ataxia type 6. Neurobiol. Dis. *43*, 533–542.

Turner, R. (2003). Techniques for imaging neuroscience. Br. Med. Bull. *65*, 3–20.

Uchino, A., Takase, Y., Nomiyama, K., Egashira, R., and Kudo, S. Brainstem and cerebellar changes after cerebrovascular accidents: magnetic resonance imaging. Eur. Radiol. *16*, 592–597.

Uswatte, G., Taub, E., Morris, D., Vignolo, M., and McCulloch, K. (2005). Reliability and validity of the upper-extremity Motor Activity Log-14 for measuring real-world arm use. Stroke. *36*, 2493–2496.

Verstraete, E., and Foerster, B.R. (2015). Neuroimaging as a New Diagnostic Modality in Amyotrophic Lateral Sclerosis. Neurotherapeutics *12*, 403–416.

Voogd, J., Schraa-Tam, C.K.L., van der Geest, J.N., and De Zeeuw, C.I. Visuomotor cerebellum in human and nonhuman primates. Cerebellum *11*, 392–410.

Vos, S.B., Jones, D.K., Viergever, M.A., and Leemans, A. Partial volume effect as a hidden covariate in DTI analyses. Neuroimage *55*, 1566–1576.

Wakana, S., Jiang, H., Nagae-Poetscher, L.M., van Zijl, P.C.M., and Mori, S. Fiber tract-based atlas of human white matter anatomy. Radiology *230*, 77–87.

Walker, L.E., Mirza, N., Yip, V.L.M., Marson, A.G., and Pirmohamed, M. (2015). Personalized medicine approaches in epilepsy. J. Intern. Med. *277*, 218–234.

Walsh, R.R., Small, S.L., Chen, E.E., and Solodkin, A. (2008). Network activation during bimanual movements in humans. Neuroimage *43*, 540–553.

Wang, J.L., Yang, X., Xia, K., Hu, Z.M., Weng, L., Jin, X., Jiang, H., Zhang, P., Shen, L., Guo, J.F., et al. (2010a). TGM6 identified as a novel causative gene of spinocerebellar ataxias using exome sequencing. Brain *133*, 3510–3518.

Wang, L., Yu, C., Chen, H., Qin, W., He, Y., Fan, F., Zhang, Y., Wang, M., Li, K., Zang, Y., et al. (2010b). Dynamic functional reorganization of the motor execution network after stroke. Brain *133*, 1224–1238.

Warburton, E., Price, C.J., Swinburn, K., and Wise, R.J.S. (1999). Mechanisms of recovery from aphasia : evidence from positron emission tomography studies. J. Neurol. Neurosurg. Psychiatry *66*, 155–161.

Ward, N.S. (2003). Neural correlates of outcome after stroke: a cross-sectional fMRI study. Brain *126*, 1430–1448.

Ward, N.S., and Cohen, L.G. (2004). Mechanisms underlying recovery of motor function after stroke. Arch. Neurol. *61*, 1844–1848.

Wedeen, V.J., Wang, R.P., Schmahmann, J.D., Benner, T., Tseng, W.Y.I., Dai, G., Pandya, D.N., Hagmann, P., D'Arceuil, H., and de Crespigny, A.J. (2008). Diffusion spectrum magnetic resonance imaging (DSI) tractography of crossing fibers. Neuroimage *41*, 1267–1277.

Wojtowicz, J.M., Smith, B.R., and Atwood, H.L. (1991). Activity-dependent recruitment of silent synapses. Ann. N. Y. Acad. Sci. *627*, 169–179.

WOLF, S., LECRAW, D., BARTON, L., and JANN, B. (1989). Forced use of hemiplegic upper extremities to reverse the effect of learned nonuse among chronic stroke and head-injured patients. Exp. Neurol. *104*, 125–132.

Wolf, S.L., Catlin, P. a., Ellis, M., Archer, a. L., Morgan, B., and Piacentino, a. (2001). Assessing Wolf Motor Function Test as Outcome Measure for Research in Patients After Stroke. Stroke *32*, 1635–1639.

Wolf, S.L., Winstein, C.J., Miller, J.P., and Morris, D. (2006). Effect of Constraint-Induced Movement. *296*, 2095–2104.

Wolf, Steven L, Winstein,Carolee J., Miller, J. Phillip, Thompson, Paul A., Taub, Edward, Uswatte, Gitendra, Morris, David, Blanton, Sarah, Nichols-Larsen, D. (2008). NIH Public Access. Lancet Neurol. *7*, 33–40.

Wolkenhauer, O., Auffray, C., Brass, O., Clairambault, J., Deutsch, A., Drasdo, D., Gervasio, F., Preziosi, L., Maini, P., Marciniak-Czochra, A., et al. (2014). Enabling multiscale modeling in systems medicine. Genome Med. *6*, 21.

Wolz, R., Julkunen, V., Koikkalainen, J., Niskanen, E., Zhang, D.P., Rueckert, D., Soininen, H., and Lötjönen, J. (2011). Multi-method analysis of MRI images in early diagnostics of Alzheimer's disease. PLoS One *6*, e25446.

Yang, G.J., Murray, J.D., Repovs, G., Cole, M.W., Savic, A., Glasser, M.F., Pittenger, C., Krystal, J.H., Wang, X.-J., Pearlson, G.D., et al. (2014). Altered global brain signal in schizophrenia. Proc. Natl. Acad. Sci. U. S. A. *111*, 7438–7443.

Yang, Q., Hashizume, Y., Yoshida, M., Wang, Y., Goto, Y., Mitsuma, N., Ishikawa, K., and Mizusawa, H. (2000). Morphological Purkinje cell changes in spinocerebellar ataxia type 6. Acta Neuropathol. *100*, 371–376.

Yasui, K., Yabe, I., Yoshida, K., Kanai, K., Arai, K., Ito, M., Onodera, O., Koyano, S., Isozaki, E., Sawai, S., et al. (2014). A 3-year cohort study of the natural history of spinocerebellar ataxia type 6 in Japan. Orphanet J. Rare Dis. *9*, 118.

Zalesky, A., and Fornito, A. (2009). A DTI-derived measure of cortico-cortical connectivity. IEEE Trans. Med. Imaging *28*, 1023–1036.

Zamora-Berridi, G.J., Pendleton, C., Ruiz, G., Cohen-Gadol, A.A., and Quiñones-Hinojosa, A. (2011). Santiago Ramón y Cajal and Harvey Cushing: two forefathers of neuroscience and neurosurgery. World Neurosurg. *76*, 466–476.

Zemke, A.C., Heagerty, P.J., Lee, C., and Cramer, S.C. (2003). Motor cortex

organization after stroke is related to side of stroke and level of recovery. Stroke. *34*, e23–e28.

Zhang, R., Wei, Q., Kang, Z., Zalesky, A., Li, M., Xu, Y., Li, L., Wang, J., Zheng, L., Wang, B., et al. (2015). Disrupted brain anatomical connectivity in medication-naïve patients with first-episode schizophrenia. Brain Struct. Funct. *220*, 1145–1159.

Zhang, Y., Brady, M., and Smith, S. (2001). Segmentation of brain MR images through a hidden Markov random field model and the expectation-maximization algorithm. IEEE Trans. Med. Imaging *20*, 45–57.

Zhuchenko, O., Bailey, J., Bonnen, P., Ashizawa, T., Stockton, D.W., Amos, C., Dobyns, W.B., Subramony, S.H., Zoghbi, H.Y., and Lee, C.C. (1997). Autosomal dominant cerebellar ataxia (SCA6) associated with small polyglutamine expansions in the alpha 1A-voltage-dependent calcium channel. Nat. Genet. *15*, 62–69.